Experimental and numerical study of an electro-osmotic flow based heat spreader.

Eng, Connie Pey Fen

Swansea University
Prifysgol Abertawe

Experimental and Numerical Study of an Electro-osmotic Flow based Heat Spreader

Connie Pey Fen Eng

Thesis submitted to Swansea University
in candidature for the degree of Doctor of Philosophy

30 June 2009

School of Engineering
Swansea University
Singleton Park, Swansea SA2 8PP
Wales, United Kingdom

Declaration

This work has not previously been accepted in substance for any degree and is not being concurrently submitted in candidature for any degree.

Signed ..... (Candidate)

Date 28.10.2009.

Statement 1

This thesis is the result of my own investigation except where otherwise stated. Other sources have been acknowledged by footnotes giving explicit references. A bibliography is appended.

Signed ..... (Candidate)

Date 28.10.2009.

Statement 2

I hereby give consent for my thesis, if accepted, to be available for photocopying and for interlibrary loan, and for the title and summary to be made available to outside organizations.

Signed ..... (Candidate)

Date 28.10.2009.

Acknowledgement

I would like to express my gratitude to my supervisor Prof P. Nithiarasu who has given me opportunity to carry out this project. His support and guidance throughout my research is also appreciated.

I would also like to thank my colleagues Owen, Sony, Alex, Chun Bin and Pure Wafer Ltd for their technical support. The financial support of Welsh Development Agency (WDA) via Knowledge Exploitation Fund (KEF) and Swansea University via staff benefit is also acknowledged.

Finally, I would like to express special thanks to my parents, Teck Mein and Fong Heong; my siblings, Pey Fong, Pey Key and Ing Siew; my relatives, Fong Eng, Kian Guap and last but not least, my partner, Arturs for their support and encouragement during my PhD studies.

Summary

In this thesis, experimental and numerical analysis of an electro-osmosis (EO) based cooling system are presented. Heat spreader with EO pump is proposed to remove heat from a microprocessor. The EO micro-pump is formed by 152 straight micro-channels and used to force the electrolyte to circulate through the elliptical micro-channels. This arrangement is expected to reduce hot spots and temperature of the microprocessor.

The fabrication of the EO heat spreader is discussed in detail in this thesis. Different channel depths are etched and tested on a silicon wafer. Besides, an isolation layer is deposited between the EO heat spreader and the microprocessor to avoid the electrical interference. The experiments of the EO heat spreader with and without isolation layer are carried out and silicon dioxide has been found to have good electrical insulation properties. The flow rate through the EO heat spreader is obtained by monitoring the distance travelled by a particle in an EO flow channel which is subjected to an external electric potential. At higher electric potential difference, electrolysis occurs and results in the bubble generation near the electrodes. To reduce the bubble generation, a pulse like voltage cycle is introduced for the first time. Finally, the experiments are carried out to study the influence of the EO heat spreader on the cooling system. The proposed EO heat spreader can reduce both the size of the heat sink and the temperature of the microprocessor.

In the latter part of the thesis, the numerical modelling of the EO heat spreader is presented. The electric potentials in the EO flow are solved explicitly and global time stepping is used. The converged electric potential solutions are added into the momentum equation. The Navier Stokes equations (NSE) which are used to govern the EO flow are non-dimensionalised. A new non-dimensional scale is selected to avoid introducing Reynolds number into the non-dimensional form. Local time stepping is used to solve the NSE. The governing equations are temporally discretised by using Artificial Compressibility - Characteristic Split (AC-CBS) algorithm is used to reduce the oscillation which is caused by the pressure and convection terms. Standard Galerkin finite element method is used for spatial discretisation. The numerical EO flow solution obtained is compared with experimental data and good agreement is obtained between the results.

Contents

List of Figures

List of Tables

Nomenclature

A	Area (m^2)
Bi	Biot number
c	Speed of sound (m/s)
c_p	Specific heat capacity (J/kgK)
C_d	Double layer capacitance (F)
D	Depth of channel in y direction (m)
$\|D\|$	Mean deviation (mm/min)
$\|D_u\|$	Velocity deviation (%)
E_1, E_2	External electric field and EDL electric field (V/m)
E_x	Non-dimensional electric potential
E_r	Experimental error (%)
e	Electron charge $(1.6 \times 10^{-19}C)$
F_i	Convective flux vector
FR	Volumetric Flow rate $(\mu l/min$ or $mm^3/min)$
G_i	Diffusion fluxes
h	convective heat transfer coefficient(W/m^2K)
h_{ie}	Element height
I_t	Total current (A)
I_E	Electrolyte current (A)
I_{Si}	Silicon current (A)
I_{SiO_2}	Silicon dioxide current (A)
J	Parameter J in source term
k_B	Boltzmann constant (m^2kg/s^2K)
k and k_∞	Thermal conductivity (W/mK)
L_m	Distance travelled by a particle between two images
m	Number of node
N	Shape function
n	Total number of particles
n_0	Bulk ionic concentration (m^{-3})
n^+, n^-	Number of positive and negative ions (m^{-3})
$\overline{n}$	normal direction
P	Pressure $(Pa$ or $N/m^2)$
Pr	Prandlt number
q	heat flux $(W/m^2s^(2))$
Q	Source terms
RF	Velocimetry system correlation parameter
R	Ratio of electrolyte current to substrate current
R_{Si}	Silicon resistance (Ω)
Re	Reynolds number
SF	Safety factor
T, T_∞	Temperature and reference (K)
T_1, $T_{Heat\ Source}$	Temperature of heat source (^oC)
T_2, $T_{Heat\ Spreader}$	Temperature of heat spreader (^oC)

T_g	Glass transition temperature, (^oC)
T_a	Temperature at position a to e (^oC)
t	Time period (s)
t_{ON}	On time period (s)
t_{OFF}	Off time period (s)
t	Time (s)
u_i	Velocity vector of electrolyte, i = 1,2,3 in x, y, z direction (m^2/s)
$u_{Mesh\ i}$	Velocity of Mesh, i = 1 to 6
$\overline{u}$	Average velocity of an electrolyte (m/s)
$\overline{u}_{num}$	Numerical non-dimensional velocity
$\overline{u}_{max}$	Maximum non-dimensional velocity
$\overline{u}_{HS}$	Helmholtz Smoluchowski velocity (m/s)
$u^\dagger$	intermediate momentum
$U^\dagger$	Velocity in CBS - Step 1
$U^{\dagger\dagger}$	Velocity in CBS - Step 3
u_{conv}	Convective velocity (mm^2/min)
u_{diff}	Diffusion velocity (mm^2/min)
V	Independent variable vector
V_d	Double layer voltage (V)
V_t	Total voltage (V)
W, L_∞	Channel width as characteristic length (m)
x_i, x_k	Channel direction in x, y and z direction, i = 1,2,3 (m)
x'	x in characteristic problem
x_{mi}	distance in x direction, i = 1,2 (particle 1 and 2)
X_{SiO_2}	Silicon dioxide reactance (Ω)
y_{mi}	distance in y direction, i = 1,2 (particle 1 and 2)
Y	distance from the channel wall (m)
z_+, z_-, z	Valence of ion
Z_E	Electrolyte resistance (Ω)
Z_t	Total impedance (Ω)

α and α_∞	Thermal diffusivity (m^2/s)
β	Artificial compressibility parameter
Γ	Surface
Δx	Displacement (m)
Δt	Time step
Δt_{conv}	Convective time step
Δt_{diff}	Diffusion time step
$\Delta Q/\Delta t$	Heat flow rate (W)
ΔT	Temperature Difference between two point (K)
ϵ and ϵ_∞	Dielectric constant
ϵ_0	Permittivity in vacuum
κ	Debye Huckel parameter
κa	Ratio of EDL thickness to width of channel

λ	Debye length (nm)
μ	Dynamic viscosity (Ns/m^2)
ν	Kinematic viscosity ($NsKgm^5$)
ϕ	External electric potential (V)
ϕ_1 and ϕ_2	External electric potential at inlet and outlet(V)
ρ and ρ_∞	Electrolyte density (kgm^3)
ρ_E	Net electric charge density (Cm^3)
Ω	Volume domain
ψ	Electrostatic or internal electric potential (V)
σ, σ_∞	Electrical conductivity ($\mu S/m$)
τ_{ij}	Deviatoric stress component (Pa or N/m^2)
θ_i	time stepping scheme, i = 1,2
ζ	Surface potential or zeta potential (V)

AC	Artificial compressibility
AC	Alternating Current
CBS	Characteristic based split
CVD	Chemical vapor deposition
DC	Direct Current
DI	De-ionized
EDL	Electric double layer
EO	Electro-osmotic/electro-osmosis
EOF	Electro-osmotic flow
FDM	Finite difference method
FEM	Finite element method
FVM	Finite volume method
HS	Helmholtz Smuluchowski
IA	Interrogation area
IC	Integrated circuit
IV	Current-Voltage
KCl	Potassium Chloride
MEMS	Micro-electro-mechanical systems
NSE	Navier Stokes equations
PIV	Particle image velocimetry
PVD	Physical vapor deposition
RCA	Radio Corporation of America
RIE	Reactive Ion Etching
SC1, SC2	Standard RCA cleaning procedure 1 and 2
SEM	Scanning electron microscope
SMU	Source measurement unit
VLSI	Very large scale integrated
μ-TAS	Micro-total analysis systems

Chapter 1

Introduction

1.1 Background

All electronic equipment produce heat during normal operating conditions, especially microprocessors used in computing and power electronic devices. According to the ITRS roadmap [5], microprocessors will generate more than 200 W/cm^2 within the next decade. Multi-chip integration, chip size reduction and transistor multiplication pose an ever challenging thermal problem in the design of the microprocessors. In order to keep the microprocessors within their safe operating temperatures, efficient thermal management of such systems is essential. Besides, the hot spots often generated by the microprocessors may shorten the life time of microprocessors. There are a few methods available to cool the hot spots of a microprocessor. They include heat sinks, thermoelectric cooling, liquid cooling, heat pipe and integrated chip cooling. Sahraoui et al [6], Upadhya et al [7] and Mudawar [8] compared various cooling techniques in their review papers. All the techniques can potentially achieve a thermal resistance well below 0.1 $^oC/W$.

In desktop computing, heat sinks are commonly used for heat dissipation from microprocessors. The large surface area of the heat sinks are normally used to allow more heat dissipation. Fan is often used to speed up the heat exchange. Air cooling systems with fan and heat sink have been used widely. However, air cooled systems in general are bulky and they can be difficult to employ in miniature equipment. In addition, the use of fan

can also increase the noise level of a computer and the poor thermal transport properties of air greatly reduce cooling potential. Air cooling method is often optimized by employing adhesive like thermal conductive pad or gel spread between microprocessor and heat sink [9].

Thermoelectric coolers are also used to cool computer components to keep temperatures within design limits without the noise of a fan. As current is allowed through two different types of materials in a thermoelectric device, it creates a temperature difference between the materials. Then, heat is transported from the hotter side of the device to the cooler side against temperature gradient.

Liquid cooling is also an alternative method of microprocessor cooling which is being implemented due to its high heat capacity. It has low noise level output compared to the fan cooling. The advantages of liquid cooling brings the heat pipe into discussion.

Heat pipe is a hollow tube containing liquid. As liquid evaporates, it carries heat to the cool end where the vapor is condensed. It returns to the hot end under capillary action. It is normally attached between the microprocessor and heat sink. Heat pipe is widely used in laptop computers [9, 10]. It is able to dissipate 25 to 30 W from a microprocessor to the heat sink. Recent work from Zuo et al [11] was able to demonstrate that the heat pipe has potential to achieve high heat flux capability of over 250 W/cm^2 and a low thermal resistance of the order of 1 $^oC/W$. The heat pipe was thermally driven by pulsating two phase flow. Heat pipes are attractive due to their high effective thermal conductivity at relatively low weight. However, very careful wick design and assembly are required to ensure that capillary force in the wick structure is able to pump the liquid back to the evaporator. In addition, the heat pipes may not be very suitable for target cooling of hot spots.

The methods of cooling discussed above use some kind of attachment to the microprocessor. Attachment technique will always exhibit some thermal resistance between the microprocessor and the attachment. Therefore, integrated chip cooling method are more attractive to remove heat from hot spots quickly. This form of local cooling is essential for high power dissipation. Potential integrated cooling systems include jet impingement cooling and micro-channel cooling.

Jet impingement directs the coolant through a small orifice and forms a jet. The jet

is directed towards the microprocessor to remove heat. It has shown cooling power densities of up to 370 W/cm^2 with single phase water cooler [12, 13]. Multi-jet impingement reported by Wang et al [14] was able to remove heat of 90 W/cm^2. The diameter of multi-jet was 76 μm at a flow rate of 8 ml/min with a temperature rise of 100 ^oC. Kiper predicted more than 500 W/cm^2 heat flux removal with micro-scale direct liquid impingement to chips from an orifice plate [15].

In micro-channel heat sinks, micro-channels are fabricated into the silicon chip and coolant is pumped through them. Micro-channels are designed to increase surface area to give better total heat transfer. Micro-channel heat sink that was demonstrated by Tuckerman and Pease was able to remove heat fluxes of 790 W/cm^2 [16]. It has effectively reduced hot spots in a most cost effective manner. Zhang et al [17] developed a single phase liquid cooled aluminium micro-channel heat sink that has low thermal resistance ranging from 0.32 to 0.44 $^oC/W$ for 12 mm^2 chip size and 0.59 to 0.44 $^oC/W$ for 10 mm^2 chip size. A pump was used to provide pressure flow to micro-channels. The flow rate from the pressure pump was in the range of 1.67×10^{-6} to $1.67 \times 10^{-5} m^3/s$. Lian Zhang et al [18, 19] showed that a flow rate of 100 $\mu l/min$ was sufficient for cooling some hot spots. Recently, various micro-channel heat sinks have been investigated due to its attractive heat transfer coefficients which can be increased by a factor of 100 to 1000 with forced two phase convection [20, 21, 22].

1.2 Review of Electro-osmotic Cooling System

The air or liquid flow through a micro-channel heat sink can increase the heat transfer rate from the microprocessor to the ambient. Recently, Jiang et al [1] developed a closed loop two phase micro-channel cooling system using electro-osmotic pumping with ultra fine porous glass. The micro-channel cooling system consists of an external electro-osmotic micro-pump, a silicon micro-channel heat exchanger and a radiator. An external electro-osmotic micro-pump pumps the coolant directly on the core of microprocessor. The coolant transports the heat to the radiator away from the microprocessor. The silicon micro-channel heat exchanger with hydraulic diameter of 100 μm was attached on the test

chip. The pump gives flow rate of 7 ml/min and back pressure of 160 kPa. This cooling system was able to remove a heat of 38 W with pumping power of 2 W. The junction ambient thermal resistance was as low as 2.5 $^oC/W$. However, the drawback of such system was the complexity in construction.

Electro-osmotic pump reported by Yao at el [23] produced up to 1.3 atm of pressure and flow rates greater than 33 ml/min, using a porous sintered-glass cylinder with a 40 mm diameter and 1 mm thickness to support cooling heat load of 100 W. The volume of this external pump was about 6000 mm^3.

An electro-osmotic pump with the size of 120 mm^3 reported by Laser at el [24, 25, 26] produced up to 10 kPa of pressure and flow rates greater than 0.17 ml/min at 400 V. These reported works show that the electro-osmotic flow has the potential to be employed in the microprocessor cooling and such systems are free of mechanical moving parts and noise.

An integration of a electro-osmotic heat spreader in the microprocessor is proposed in the present work. The heat spreader proposed is located in the proximity of the microprocessor to remove the hot spots more effectively. Besides, the electro-osmotic pump has no moving parts and it can potentially give high flow rates.

In addition, the design proposed reduces the complexity of the cooling system due to no piping or external connections. The development of VLSI technology is beneficial to the integration process of the proposed heat spreader. An elliptical micro-channel structure has been designed to allow liquid circulation on the microprocessor surface. This makes the heat flux on the microprocessor surface more uniform. An electro-osmotic pump section is fabricated within the heat spreader to induce flow. Small external electric fields are supplied via two gold electrodes which are deposited across the pumping section. The electro-osmotic heat spreader is integrated between a heat sink and the microprocessor. The micro-scale electro-osmotic heat spreader is able to reduce the temperature of the microprocessor.

1.3 Review of the Numerical Model of EOF

Numerical model of EOF in capillaries has attracted attention from various research groups including Burgeen and Nakache [27], Rice and Whitehead [28] and Hu et al [29]. In these studies, the finite difference method (FDM) was used to obtain a solution of the electric potential distribution. This method is straight forward and easy to use.

Finite volume method (FVM) is also employed to solve the governing equations. This method has been used by Min et al [30] for a non uniform structure grid. Besides, Tang et al [31, 32, 33] use the FVM in their study on thermal effects in electro-osmotic flow. This method was also used by Patankar and Hu [34].

There are some works available on the finite element method (FEM). Bianchi et al [35] used FEM to explore two dimensional electro-osmotic flow at a micro-scale T-junction. The electric field was firstly solved and then a source term was added to the Navier Stokes equations (NSE) and solved. Erickson and Li [36] and Borges et al [37] also used FEM to solve NSE. The FEM offers flexibility to solve EOF in complex geometries and obtain accurate result in a specific area with a fine mesh.

The characteristic based split (CBS) algorithm is employed to temporally discretise the governing equations of electro-osmotic flow. This method was developed by Zienkiewicz and Codina [38] and has been widely used in other incompressible flow applications as noted by Nithiarasu et al [39, 40]. In CBS algorithm, the momentum equation is split up into two parts, in order to remove the instability caused by the pressure term by introducing an intermediate momentum. This results in the algorithm consisting of three steps. The first is to solve for the intermediate momentum. The pressure is solved for the second step and finally the momentum is corrected by replacing the intermediate term. The CBS has proven to be stable, versatile and can be used in both incompressible and compressible flow problems [38, 41, 42, 43].

The stability of CBS scheme make it possible to model electro-osmotic flow (EOF) channel. Galerkin finite element procedure is used to spatial discretisation to obtain an accurate velocity profile of EOF channel. This model can be used to simulate EOF in a conjugate heat transfer model.

1.4 Outline of Thesis

The aim of the project is experimental investigations and numerical simulations of an electro-osmotic heat spreader. Experimental investigations provide the information about the physical process and give the actual measurement. An experimental investigation involves full scale test. There are some difficulties associated with measurements and that the measuring instrument are not free from error. Numerical simulations are normally developed from a mathematical model. The mathematic model consists of a set of governing differential equations which would predict the phenomena approximately. In the present work, fluid flow model and heat conduction and convection models are developed to simulate the electro-osmotic heat spreader.

The second chapter in this thesis presents the electro-osmotic principles and background, including the assumptions made. It also introduces the equations which govern the electro osmotic effect close to the surface of the channel.

A prototype of the proposed electro-osmotic heat spreader is fabricated for experimental measurements. Fabrication processes involving mask design, lithography, etching, thermal oxidation, metal deposition and bonding techniques are described in detail in Chapter 3. Shallow and deep micro-channels have been etched with the aid of positive and negative photo-resist. Various micro-channel depths are shown using scanning electron microscope (SEM) photos. Straight micro-channel structure and elliptical heat spreader structures have been fabricated for electro-osmotic flow studies.

Integration of heat spreader at the back of the microprocessor will result in current interference between the microprocessor and electro-osmotic heat spreader. This will affect the performance of the microprocessor. Silicon dioxide layer is deposited between them to force the current to flow through the electrolyte. Experiments are carried out and shown in Chapter 4 to demonstrate that the effectiveness of silicon dioxide to avoid current straying to the microprocessor.

Velocimetry experiments are carried out to measure the velocity of particles which are inserted into the electrolyte samples. This method is explained in detail in Chapter 5. The velocities generated in the experiments are used to calculate the flow rate of the

electro-osmotic flow. In this chapter, the influences of a few parameter, including external electric field, zeta potential and cross sectional area are explored in the flow measurement.

As driving voltage of electro-osmotic flow exceeds 1.2 V, electrolysis occurs at the electrodes. Redox reaction generates bubbles which will block the micro-channels. Experiments with the pulsed voltage are carried out to reduce the bubble generation which is explained in Chapter 6. The influence of electrolyte electrical conductivity, frequency, duty cycle and voltage are investigated in this chapter. Flow rate is measured with the pulsed power source.

Temperature measurements to study the effect of electro-osmotic flow heat spreader on the microprocessor are presented in Chapter 7. A heat source is used to replace the microprocessor. The temperature of the heat source, and the temperature at other locations are measured with and without the aid of cooling system.

The non dimensional form of the governing equations is outlined in Chapter 8. This produce important non dimensional parameters which are used in the following chapter. The chapter concludes by describing the boundary conditions imposed on the channel specific to electro-osmosis.

The method by which the equation governing the electro-osmotic force is discretised is described in Chapter 9. These equations are decoupled and pseudo time term is included in order to perform a temporal discretisation. The effect of these equations is incorporated into a source term which is added to the momentum equation. The weak form of the governing equations are presented, followed by an outline of the boundary conditions important to micro-channel flow. The validation of model against experimental and numerical results is carried out in this chapter.

The Chapter 10 is concerned with electro-osmosis in a straight micro-channel systems and the heat spreader. The flow rate is calculated from the velocity which is obtained from the numerical simulation. The velocities of numerical model are compared with the experimental results. Following this, conjugate heat transfer model is discussed in latter part of this chapter. The conjugate system contains electro-osmotic micro-channels and a heat sink. The difference between the systems with and without electro-osmotically driven heat spreader on a uniform and non uniform heat source is investigated.

Chapter 11 concludes the thesis, discussing what has been investigated and the outcomes of experimental and numerical results. Following the conclusions, potential future work is outlined.

Chapter 2

Electro-osmosis Principle

2.1 Introduction

The electrokinetic phenomena can be classificated into four main types. These are listed in the Table 2.1. In both electro-osmosis and electro-phoresis, an electric field is applied to induce motion. The remaining two phenomena have opposite features in that they use motion to produce an electric field.

Table 2.1: Classification of main electrokinetic phenomena.

Name	Type of Movement
Electro-osmosis	Liquid moves relative to a stationary charged surface with an applied electric field
Electrophoresis	The charged surface moves relative to a stationary liquid with an applied electric field
Streaming potential	Liquid moves relative to a stationary charged surface to create an electric field
Sedimentation potential	The charged surface moves relative to a stationary liquid to create an electric field

Electro-osmotic flow was discovered by F. F. Reuss, a scientist from Moscow in 1809 [44]. Reuss found that applying an electric field across a porous medium filled with a dielectric liquid caused the liquid to flow. Any combination of an electrolyte and insulator would generate electro-osmotic flow. In the past, electro-osmotic flow has been used in de-watering soil and sludge [45].

Recently, electro-osmotic phenomena has spurred development of potential applications of separation, mixing and transportation in the lab-on-chip devices. These lab-on-chip devices employ electro-osmosis to handle small volume of liquid in the range of nano and pico-liters which can be dangerous chemicals. These devices can ease the chemical, biological and medical diagnosis and analysis [46, 47, 48]. The electro-osmotic effect can be used to induce the DNA-DNA hybridization in a DNA micro-array [49, 50] or extract chromosomes from the DNA [51]. The implementation of capillary electrophoresis in a miniature device have induced higher efficiency and faster response times and reduced reagent consumption in drug delivery [52].

Fluids involvement in MEMS technology, sparked the development of electro-osmotic micro sensors [53] and micro pumps [54]. Zeng et al [55] fabricated EOF pump by packing 3.5 μm diameter non porous silica into 500 to 700 μm diameter fused silica capillaries. The pump can generate a maximum pressure in excess of 20 atm and flow rate of 3.6 $\mu l/min$ at 2 kV applied potential. Chen et al [56] fabricated an EOF pump on soda lime glass substrate using standard micro-lithography and chemical wet etching techniques. The pump provided a maximum pressure and flow rate performance of 0.33 atm and 1.5 $\mu l/min$ at 1 kV applied potential. The usage of electroosmosis as pumping mechanism is beneficial in pumping the liquid to remove heat from thermal device [1].

2.2 Electro-osmotic phenomena

Electro-osmotic phenomena occurs in an electric double layer (EDL) structure. The EDL appears on a surface when it is in contact with an electrolyte.

The simplest EDL was first introduced by Helmholtz in 1879 [57, 58]. In the Helmholtz model, only a single layer of ions is adsorbed to the surface. The defect of this model is that no interaction occurs further away from the first layer of adsorbed ions. This model has been improved by Gouy Chapman model (1910-1913) with a diffused layer introduced in the electric double layer. In the diffuse layer, the potential at the surface decrease exponentially between the surface to the bulk fluid.

The electric double layer has been further improved with the Stern model in 1924.

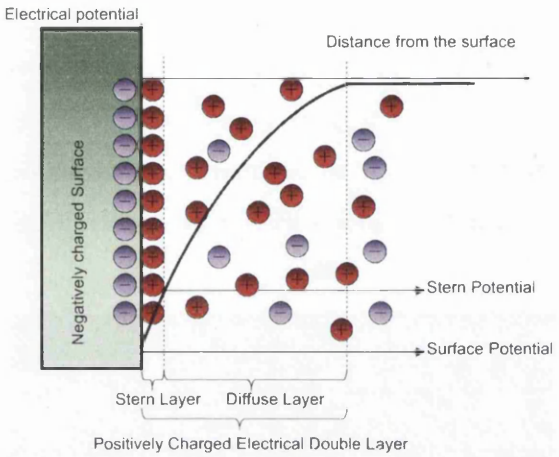

Figure 2.1: Electric Double Layer.

Stern model is the combination of both Helmholtz and Gouy Chapman models which is shown in Figure 2.1. For example, when a silicon surface is in contact with an electrolyte, the silanol ($Si-OH$) groups at the surface lose charges and turn into $Si-O^-$, resulting in a net negative surface potential. These negative surface charges influence the migration of positive charges within the electrolyte. The positive charges are attracted towards the surface and form a diffuse layer. There are some positive charges which are fixed to the negative surface charges forming a very thin layer called Stern layer. Both diffuse and Stern layer together are called electric double layer (EDL). Here, the EDL is positively charged when in contact with a negatively charged surface. The EDL thickness is determined by the strength of the electrolyte. It is also known as Debye length, λ.

This Stern model has made some assumptions as below:

1. Boltzmann distribution describes the ion concentration in the electrolyte.
2. The potential is defined as a function of distance from a surface where the ions are point charges.
3. The diffuse layer begins at some distance from the surface.
4. Viscosity of fluids is constant above slipping plane.
5. Dielectric permittivity is constant throughout the double layer.

When an external electric potential is employed across a channel as shown in Figure 2.2, the positive charges in the diffuse layer can be moved towards the negative electrode. In the mean time, the positive charges drag along the bulk fluid and results in fluid flow in the channel. The motion of liquid induced by an external electric potential is called electro-osmotic flow. Figure 2.2 also shows the internal potential and velocity distribution in a channel.

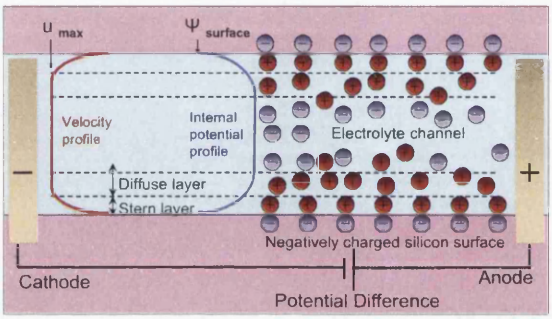

Figure 2.2: EOF in negative charged surface.

The electro-osmotic phenomena has been analytically studied by scientists since 1965 [27, 28]. Burgeen and Nakache [27] studied the effect of the surface energy and electrokinetic radius on liquid transportation through very fine capillary channels of rectangular cross section under an imposed electrical field. They solved electro-osmotic flow problem analytically for channels with arbitrary cross sections applicable to capillaries having any magnitude of ionic energy, providing the electrokinetic radius is sufficiently large. Rice and Whitehead [28] studied the same problem but in a narrow cylindrical capillaries. The electro-kinetic radius has been calculated on the basis of Debye Huckel approximation for the net charge density in the double layer. Levine et al [59] considered flow in a tube under the Debye Huckel approximation. They produced results for both thin and overlapping double layers. Symmetry of the flow with respect to the direction normal to the channel walls is assumed. The current flow is also calculated. Maynes and Webb [60] analyzed the electro-osmotic flow between parallel plates and circular micro-tube under imposed constant wall heat flux and constant temperature boundary conditions. Conlisk et al [61] solved the problem for strong electrolyte solutions and considered the case where there is a potential

difference in the direction normal to the channel walls corresponding in some cases to oppositely charged wall. They indicate that under certain conditions reversed flow may occur in the channel and this situation can significantly reduce the flow rate. Patankar and Hu [34] studied the electro-osmotic injection characteristics of a cross channels geometry for capillary electro-phoresis.

2.3 Electro-osmotic Flow Profile

The electro-osmotic pump is preferred over the conventional pressure driven pump. The main reason is it gives plug like velocity profile. In the plug like velocity profile, the velocity of electrolyte is almost the same over the cross sectional of a channel, unlike the parabolic flow profile which is produced by conventional pressure driven pump. In the parabolic flow profile, the velocity of electrolyte is higher in the center and lower near the wall. The parabolic velocity flow profile always appears in laminar flow which Reynold number is in between 1 and 2300. Reynold number is defined as:

$$Re = \frac{\rho \overline{u} L}{\mu} \tag{2.1}$$

where ρ, $\overline{u}$, L and μ are electrolyte density, velocity, viscosity and characteristic length of a channel. On the other hand, the plug like velocity profile can be observed in turbulent flows where Reynold number is more than 2300. Flow with Reynold number less than 1 is defined as Stokes flow. Stokes flow is influenced by the viscosity of the electrolyte.

The flow profiles impact the heat transfer in the channel of flow. Thus, the heat convection in the parabolic flow is more significant in the center but gradually reduced nearer the wall. However, in the plug like flow profile, heat can be transported without dispersion caused by flow shear.

The thickness of electric double layer (EDL) has great influence on the electro-osmotic flow profile. At thin EDL, the ions are more distributed near the wall and the internal potential becomes large. Therefore, when an external potential difference is employed, a lot of ions are moved towards to the electrode ultimately leading to higher velocity. Here, a plug flow velocity profile is created. At thick EDL, the ions are dispersed from the

wall giving weaker internal potential. Subsequently, much fewer ions are moved as an external potential difference is employed. The velocity profile becomes parabolic compared with the thin EDL. As the thickness of EDL at both ends of the walls is large enough to overlap, the produced velocity is the smallest compared with the previous cases. This is due to high viscous friction in the flow. EDL overlapping phenomena can be seen in the flow profile of nano-channel [62].

2.4 Governing Equations

The electric field induced by the electric double layer and the external electric field could generate the electro-osmotic flow. The electro-osmotic flow is governed by the Navier Stokes equations [63].

2.4.1 Electric Field Equations

The electric field induced by external potential, E_1 in a charge free region of space is written as:

$$\frac{\partial(\sigma E_1)}{\partial x_i} = 0 \tag{2.2}$$

where σ represents the liquid electrical conductivity and it is assumed constant. The external electric field, E_1 and external electric potential, ϕ are related via

$$E_1 = -\frac{\partial \phi}{\partial x_i} \tag{2.3}$$

Thus the external electric field is governed by the Laplace equation of the type

$$\frac{\partial^2(\sigma \phi)}{\partial x_i^2} = 0 \tag{2.4}$$

The electric field in electric double layer, E_2 relates to charge density via the following relationship.

$$\frac{\partial(\epsilon E_2)}{\partial x_i} = \frac{\rho_E}{\epsilon_0} \tag{2.5}$$

where E_2 is the electric field, ρ_E is the net charge density, ϵ_0 is the permittivity of vacuum and ϵ is the dielectric constant of the electrolyte. Electric field is related to electrostatic potential or internal potential, ψ via

$$E_2 = -\frac{\partial \psi}{\partial x_i} \tag{2.6}$$

Combining Equations 2.5 and 2.6 we get the Poisson equation.

$$\frac{\partial^2 \psi}{\partial x_i^2} = -\frac{\rho_E}{\epsilon \epsilon_0} \tag{2.7}$$

Note that ϵ is assumed to be constant. Assuming that the Boltzmann distribution applies, the Boltzmann distribution equation can be used to describe the ion distribution per unit volume, n_0 in the electric double layer. It depends on temperature of the electrolyte in Kelvin, T and $ze\zeta$ which is the energy required to bring the ions from an infinite distance, where ζ is zero, to region where ζ varies exponentially as

$$n^+ = n_0 \exp\left(-\frac{z_+ e\psi}{k_B T}\right); n^- = n_0 \exp\left(\frac{z_- e\psi}{k_B T}\right) \tag{2.8}$$

where electron charges, e is $1.6 \times 10^{-19} C$. k_B is the Boltzmann's constant with the value of $1.38065 \times 10^{-23} m^2 kg s^{-2} K^{-1}$. The charge density ρ_E can be expressed in terms of Boltzmann distribution and for a symmetric electrolyte where valence of electron, $z = |z_+| = |z_-|$, it is given by

$$\rho_E = (n^+ - n^-) ze \tag{2.9}$$

$$\rho_E = -2 n_0 ze \sinh\left(\frac{ze\psi}{k_B T}\right) \tag{2.10}$$

where

$$\sinh(x) = \frac{\exp(x) - \exp(-x)}{2} \tag{2.11}$$

The exponential variation in the Boltzmann distribution remains in the form of hyperbolic sine function in the charge density equation after applying the trigonometry relation. The combination of Boltzmann distribution and the Poisson equation gives a Poisson-Boltzmann equation. Non linear Poisson-Boltzmann equation relates the electrostatic potential and the number of ions per unit volume of a dielecric medium, i.e.,

$$\frac{\partial^2 \psi}{\partial x_i^2} = \frac{2n_0 ze}{\epsilon\epsilon_0} \sinh\left(\frac{ze\psi}{k_B T}\right) \tag{2.12}$$

The electrostatic potential, ψ is the potential that exists at the boundary between Stern layer and diffuse layer. At small zeta potential ζ, the electrostatic energy $ze\zeta$ of charges is much smaller than their thermal energy $k_B T$. Then, $\left(\frac{ze\zeta}{k_B T}\right) \ll 1$, $\sinh \frac{ze\zeta}{k_B T} \approx \left(\frac{ze\zeta}{k_B T}\right)$, whereby Debye Huckel approximation is assumed and linear Poisson-Boltzmann equation is obtained [61].

$$\frac{\partial^2 \psi}{\partial x_i^2} = \frac{2n_0 ze}{\epsilon\epsilon_0} \left(\frac{ze\psi}{k_B T}\right) \tag{2.13}$$

For a large zeta potential, the Debye Huckel approximation does not remain valid and hyperbolic sine term appears. In the present study, non-linear Poisson-Boltzmann equation has been solved numerically [64].

2.4.2 Modified Navier-Stokes Equations

For resolving EOF, a modified form of the NSE is required. They are

Continuity Equation:

$$\frac{\partial \rho}{\partial t} = -\rho \frac{\partial u_i}{\partial x_i} \tag{2.14}$$

By applying gas law, the speed of sound, c is defined as

$$c^2 = \frac{\partial P}{\partial \rho} \tag{2.15}$$

$$\frac{\partial \rho}{\partial t} = \frac{\partial \rho}{\partial P}\frac{\partial P}{\partial t} \tag{2.16}$$

$$= \frac{1}{c^2}\frac{\partial P}{\partial t} \tag{2.17}$$

The continuity equation can be rewritten as:

$$\frac{1}{c^2}\frac{\partial P}{\partial t} = -\rho\frac{\partial u_i}{\partial x_i} \tag{2.18}$$

where x_i and u_i are the spatial coordinates and velocity vector of a domain with i = [1, 2, 3]. u_1, u_2 and u_3 are the components of velocity vector in x, y and z directions respectively.

The driving force of electro-osmotic flow is created by the interaction between net charge density, ρ_E in the electric double layer regime and the applied electric field E. Therefore, the electric field created by an external potential and electric double layer are added as a source term of the momentum equation for incompressible steady flow of an electrolyte.

Modified momentum equation:

$$\rho\left(\frac{\partial u_i}{\partial t} + u_j\frac{\partial u_i}{\partial x_i}\right) = -\frac{\partial P}{\partial x_i} + \frac{\partial \tau_{ij}}{\partial x_i} + \rho_E E_1 \tag{2.19}$$

where

$$\tau_{ij} = \mu\left(\frac{\partial u_i}{\partial x_j} + \frac{\partial u_j}{\partial x_i}\right) \tag{2.20}$$

The pressure gradient, the first term on the right hand side of momentum equation is very small. This is because the only force to drive electro-osmotic flow is from an external electrical field. Thus, the motion of the flow may be reduced to a balance between the viscous or shear stress in the fluid and the external electric field force.

The convective term on the left hand side of the momentum equation is a physical process that occurs in a flow of electrolyte in which some property is transported by the ordered motion of the flow. The stress tensor τ and the viscosity of electrolyte are in the diffusion term. The charge density and external electric field are coupled and the momentum equation can be rewritten as (using Poisson Boltzmann distribution):

$$\rho\frac{\partial u_i}{\partial t}+\rho u_j\frac{\partial u_i}{\partial x_i}=-\frac{\partial P}{\partial x_i}+\mu\frac{\partial}{\partial x_i}\left(\frac{\partial u_i}{\partial x_j}+\frac{\partial u_j}{\partial x_i}\right)+2n_0ze\sinh\left(\frac{ze\psi}{k_BT}\right)\frac{\partial\phi}{\partial x_i} \tag{2.21}$$

When temperature is involved in the electro-osmotic system, the energy equation can be derived as

Energy equation:

$$c_p\rho\left(\frac{\partial T}{\partial t}+u_j\frac{\partial T}{\partial x_j}\right) = k\frac{\partial}{\partial x_j}\left(\frac{\partial T}{\partial x_j}\right)+\sigma|E|^2 \tag{2.22}$$

$$\left(\frac{\partial T}{\partial t}+u_j\frac{\partial T}{\partial x_j}\right) = \alpha\left(\frac{\partial^2 T}{\partial x_j^2}\right)+\frac{\sigma}{c_p\rho}\left|-\frac{\partial\phi}{\partial x}\right|^2 \tag{2.23}$$

where T is the temperature in Kelvin c_p and k are specific heat capacity and the temperature dependent thermal conductivity of the electrolyte respectively. The last term on the right hand side represents Joule heating produced by the external electric potential [34, 33, 65, 66]. The thermal diffusivity, α is defined as:

$$\alpha=\frac{k}{c_p\rho} \tag{2.24}$$

Joule heating is ignored in this study because the applied electric field on solid is very small.

The convective term is dropped off when only heat conduction occurs in the solid material. The heat conduction equation can be expressed as:

$$\left(\frac{\partial T}{\partial t}\right)=\alpha\left(\frac{\partial^2 T}{\partial x_j^2}\right) \tag{2.25}$$

The coupled mass, momentum and energy equations form Navier Stokes Equations in three dimensions which can be written as:

$$\frac{\partial\mathbf{V}}{\partial t}+\frac{\partial\mathbf{F_i}}{\partial x_i}+\frac{\partial\mathbf{G_i}}{\partial x_i}+\mathbf{Q}=0 \tag{2.26}$$

with independent variable vector:

$$\mathbf{V^T}=(\rho,\rho u_1,\rho u_2,\rho u_3,\rho T) \tag{2.27}$$

with convective flux vector:

$$\mathbf{F_i^T} = (\rho u_j, \rho u_j u_1, \rho u_j u_2, \rho u_j u_3, \rho u_j T) \tag{2.28}$$

with diffusion fluxes:

$$\mathbf{G_i^T} = \left(0, \tau_{1j}, \tau_{2j}, \tau_{3j}, \frac{k}{c_p}\frac{\partial T}{\partial x_j}\right) \tag{2.29}$$

with the sources terms:

$$\mathbf{Q^T} = (0, g_1, g_2, g_3, 0) \tag{2.30}$$

where

$$g_i = 2n_0 ze \sinh\left(\frac{ze\psi}{k_B T}\right)\frac{\partial \phi}{\partial x_i} \tag{2.31}$$

2.5 Electrode-Electrolyte Interface

As described in the previous section, electric double layer is formed between a surface when in contact with electrolyte. In this section, a double layer formed near the electrode-electrolyte interface is discussed. The capacitance induced by the double layer in the electrolyte near the electrode surface would influence the impedance of electrolyte used. This will be discussed in detail in Chapter 4.

The quantities of charges in the double layer will affect the charge transfer reaction in the electrolysis process. An increase of charge transfer reaction in an electrolyte, generates gas near the electrodes and pose a problem in the proposed EO heat spreader. This will be discussed further in Chapter 6.

The equivalent circuit of the electrode-electrolyte interface is illustrated in Figure 2.3.

C_d is double layer capacitance [67]:

$$C_d = \sqrt{\left(\frac{2n_0 z^2 e^2 \epsilon\epsilon_0}{k_B T}\right)} cosh\frac{ze\zeta}{2k_B T} \tag{2.32}$$

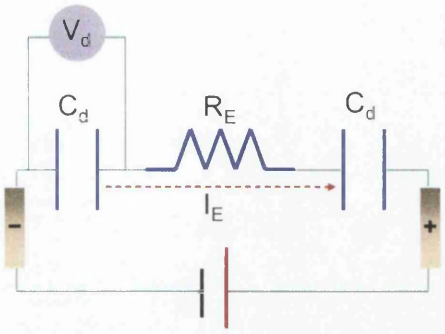

Figure 2.3: Electrolyte $R_E C_d$ equivalent circuit.

Total impedance of the electrolyte, Z_E relates to the double layer capacitance C_d and the electrolyte resistance R_E. It is written as:

$$Z_E = \sqrt{R_E^2 + X_c^2} \tag{2.33}$$

where double layer capacitance reactance is:

$$X_c = \frac{1}{2\pi f C_d} \tag{2.34}$$

At high electrolyte concentration n_0, the double layer capacitance is large. More current is needed to charge the double layer capacitor. As a result the resultant current of $R_E C_d$ equivalent circuit, I_E is large.

$$I_E = C_d \frac{\partial V_d}{\partial t} \tag{2.35}$$

where V_d is the voltage of the capacitance.

2.6 Summary

The background theory and governing equations of electric double layer (EDL) and electro-osmosis (EO) are discussed in this chapter. Laplace and Poisson Boltzmann equations were used to govern the external electric field and the electric field generated near the electric double layer. The Navier Stokes equations which are formed by continuity,

momentum and energy equations were used to describe the electro-osmotic flow. The momentum equation contains convective, pressure, viscosity and source term. The EO electric fields were added to momentum equations via source terms. EO phenomena will be used in designing a new generation of micro-cooling system and this will be discussed further in the latter chapters.

Chapter 3

Device Fabrication Process

3.1 Introduction

The transistors in the microprocessor create hot spots and reduce the performance of the microprocessor. Some works suggest that the size of the heat sink has to be increased to reduce hot spots [5, 68, 69]. However, increasing the heat sink volume may not always be possible. Therefore, an elliptical integrated heat spreader has been proposed in Section 3.2 between the heat sink and the microprocessor to avoid excessive increase in heat sink size. The purpose of elliptical heat spreader is to force electrolyte to circulate on the back surface of the microprocessor and spread the heat uniformly to eliminate hot spots. Liquid is used as a medium to transport heat because liquid has higher heat capacity compared to air.

In this chapter, a description is given about the processes that were used to fabricate straight micro-channels and elliptical heat spreader. During this research masks for lithography process were designed together with cleaning procedures that are essential before lithography process. Also, the recipes for fabricating straight-channel structure and elliptical heat spreader have been developed. Shallow etching and deep etching have been employed using both positive and negative photo-resist. The silicon dioxide is grown via thermal oxidation and the gold thin film electrodes are deposited via sputtering process. Finally the heat spreader is sealed employing the silicon direct bonding and anodic bonding.

3.2 Proposed Design

The schematic diagram of a proposed micro heat spreader is shown in Figure 3.1. The design consists of two silicon wafers which have thickness of about 1 mm. The bottom silicon wafer is assumed to be the microprocessor chip. Straight and elliptical micro-channels are etched at the back surface of the microprocessor chips. Here, the silicon that we used has a size of 3.5 cm and 2.5 cm in width and length. The electrodes are deposited across all the straight micro-channels. The top silicon wafer acts as both a water tight cover and the heat sink.

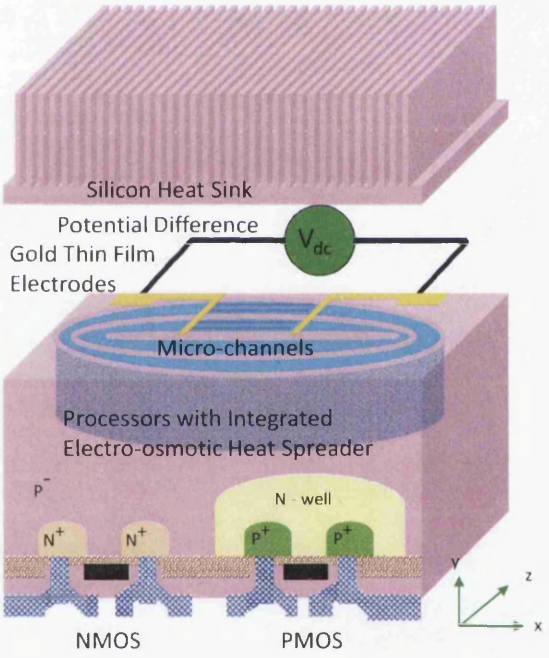

Figure 3.1: Proposed model.

Straight micro-channels are used as an electro-osmotic micro-pump which can force the liquid flowing into the elliptical micro-channels by subjecting it to a small external potential via the electrodes. The micro-pump area has a size of 20 to 25 mm^2. The elliptical micro-channels will circulate the liquid around on the back surface of the microprocessor and spread the heat from hot spot uniformly. The plate fin heat sink is expected to be attached to the top surface of the top silicon wafer to dissipate heat from the micro heat spreader to

the ambient. It also has some provision to input the liquid into the heat spreader.

The EO heat spreader has no moving pump and no complex piping connection making it reliable and suitable for multi stack modules. It can be integrated at the back surface of the silicon wafer for every layer of a chip. Thus, the hot spot can be spread instantly before transferring into the next layer. In the following section, a brief overview on common substrate materials and micro-fabrication steps are given.

3.3 Material

Polydimethylsiloxane (PDMS) and glass are common materials which are used to fabricate the micro-fluidic devices. Kim et al and Glawdel et al [4, 70] used PDMS to fabricate electro-osmotic pump for the lab-on-chip devices. Yao et al [23] used borosilicate glass to make their electro-osmotic pump. The pump was connected to a micro-channel heat sink in a cooling system. Brask et al [71], using borosilicate and silica glass frit, assembled in an electro-osmotic pump to generate flow for micro-fluidic devices. Takamura et el [72] developed a low voltage electro-osmotic pump with quartz for micro-total analysis systems (μ-TAS) and lab-on-chip devices. PDMS and glass are good materials to produce electro-osmotic pump for laboratory analysis. However, both materials have poor thermal conductivities as illustrated in Table 3.1. Thus, the micro-fluidic devices made by PDMS and glass have difficulty in dissipating the heat which is generated internally when a high electric field is applied across electrodes [31, 36].

Thus, in this thesis silicon has been chosen to fabricate the electro-osmotic heat spreader. Silicon is a standard substrate material for micro-electro-mechanical system (MEMS) [73] and integrated circuit (IC). The silicon wafer is available with diameters from 100 to 300 mm. Therefore, the devices can be manufactured from the silicon wafer economically in large volumes. It also has favourable electrical and thermal properties (Table 3.1) which enable the co-integration of micro-device and chip [74].

Table 3.1: Properties of silicon, PDMS and Borosilicate glass.

Thermal Properties	Silicon	PDMS	Borosilicate Glass
Thermal Conductivity W/mK	149	0.15	1.1
Dielectric Constant	11-12	2.3-2.8	4.8

3.4 Lithography and Etching

The micro-fabrication processes of proposed heat spreader with silicon substrate as in Figure 3.1 are described in detail in this section [75, 76, 77]. The micro-fabrication techniques for heat spreader are identical to those used in micro-electro-mechanical system (MEMS) which include photo-lithography, etching, thermal oxidation, thin film deposition and bonding. These techniques are combined to fabricate the heat spreader.

IC are extremely sensitive to contaminants prior to micro-fabrication process. Therefore, the Radio Corporation of America (RCA) cleaning needs to be performed to the silicon wafer before starting the high temperature and fabrication process in the semiconductor manufacturing. RCA cleaning is a standard set of wafer cleaning steps which involves removal of organic contaminants, oxide layer and ionic contamination. The silicon wafer must be cleaned following the standard RCA cleaning procedure 1 (SC1) with the solution of ammonium peroxide (NH_4OH): Hydrogen peroxide (H_2O_2): DI water at 70 ^oC in ratio of 1:1:5. The SC1 treatment is used to remove the contamination on the silicon substrate. However, this treatment results in the formation of a thin silicon dioxide layer on the silicon surface, along with a certain degree of metallic contamination that is removed in the standard cleaning procedure 2 (SC2). It is performed with 1:1:5 solution of Hydrogen chloride (HCl): Hydrogen peroxide (H_2O_2): DI water at 70 ^oC. This treatment is used to dissolve the alkali ions and hydroxide.

After wafer cleaning, a layer of photo-resist is spun uniformly on the silicon substrate. The photo-resist is a light-sensitive chemical which can be categorized into positive and negative photo resists. The positive photo-resist is a type of photo-resist that becomes soluble to the photo-resist developer after having been exposed to the light. The portion of the photo-resist left unexposed remains insoluble to the photo-resist developer. The positive photo-resist is commonly used in IC fabrication due to its simplicity in developing.

However, it is not suitable to fabricate high aspect ratio channel. This is because positive photo-resist has less silicon-to-photo-resist selectivity in the silicon etching process. Therefore, negative photo-resist is used in generating deep channels. It has the reverse effect when exposed to the light, as compared to the positive photo-resist. The spinning speed and duration of photo-resist is important in determining photo-resist thickness [77].

After the photo-resist is applied to the substrate, it must be soft baked to evaporate the solvent. Duration and temperature of baking should be optimized since solvent evaporation rate is influenced by the rate of heat transfer.

Photolithography is used to selectively remove parts of the photo-resist. It uses ultraviolet (UV) light to transfer the desired pattern from a photo-mask to a photo-resist on the substrate. Photolithography consists of the following two steps.

(i) Positioning process: The substrate which is coated with photo-resist will be aligned in position with the photo-mask using MJB3 Mask Aligner. The substrate is held on a vacuum chuck.

(ii) Exposure process: The substrate is brought into physical contact with the photo-mask which is called contact printing during optical exposure. Then, the mask pattern is transferred to the wafer using the optical exposure. The exposure intensity (in W/cm^2) at the substrate times the exposure time (in seconds) give exposure energy or dose (in mJ/cm^2). The intensity is a measure of time averaged energy flux.

After lithography process, the silicon with pattern proceeds to Reactive Ion Etching (RIE) process. RIE is a plasma etching which is used in conjunction with photolithography techniques to etch micro-channels of the heat spreader. This process creates directional electric field near the substrate to achieve more anisotropic etch profile. Under low pressure and electromagnetic field, gas reagents are transformed into plasma ions. The ions meet the substrate surface almost perpendicularly. Therefore, this plasma etching method can produce relatively high aspect ratio micro-channels [75, 76]. The use of reagents which include sulfur hexafluoride, SF_6 and oxygen, O_2 have been optimized to give the faster etch rate. The chamber base pressure and individual gas flow rate are the control factors the etch rate. The etch rate is determined from the etching experiment. Etching process practically also reduces the photo-resist layer thickness.

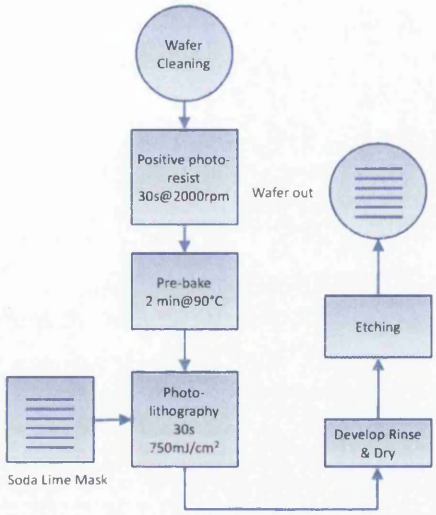

Figure 3.2: Flow chart of using positive photo-resist in straight micro-channels structure.

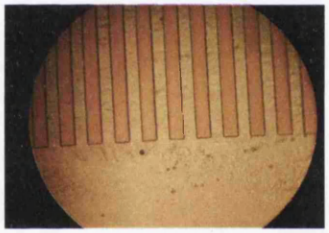

Figure 3.3: Positive Photo-resist.

After plasma etching, the micro-channels are observed with scanning electron microscope (SEM). The channel width and depth of the structure are measured.

3.4.1 Straight Micro-channel Structure

Straight micro-channel structure with a width of 30 μm is fabricated to study the electro-osmotic characteristics. The fabrication process of the straight micro-channel structure is summarized in Figure 3.2. S1828, a positive photo-resist material is spun at a speed of 2000 rpm for 30 s to uniformly spread the photo resist on the substrate. The substrate is then heated up to a temperature of 90 ^oC for 2 minutes to evaporate the solvent from the photo-resist. Then, the silicon with photo-resist is exposed to 436 nm UV light

in MJB3 mask aligner. After that it is exposed to UV light with intensity of 25 mW/cm^2 for 30 s. The exposure dose of S1828 can be calculated and is equal to 750 mJ/cm^2. The substrate with patterned photo resist is developed using Microposit MF-319 developer. The result is shown in Figure 3.3. The silicon with patterned photo resist is finally immersed in a developer to remove the exposed area.

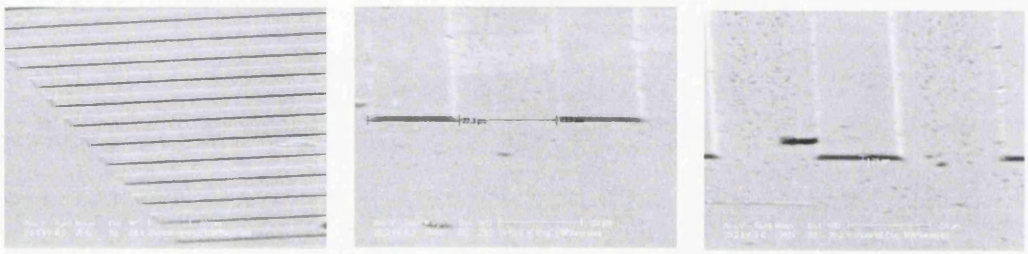

(a) (b) (c)

Figure 3.4: Shallow micro-channel structures with a depth of 1.25 μm.

Table 3.2: RIE Etching recipes.

Parameter	Recipe 1	Recipe 2
Silane SF_6, (sccm)	100	30
Oxygen O_2, (sccm)	10	10
Pressure, (mTorr)	200	200
Power, W	100	200

After lithography process, the silicon substrate with patterned photo-resist is sent for dry etching. The recipes of dry etching are shown in Table 3.2. In Recipe 1, the flow rate of SF_6 and O_2 is 100 $sccm$ and 10 $sccm$ respectively. The chamber pressure is 200 $mTorr$ with the power of 100 W. The oxygen plasma etching can strip most solidified photo-resist. It has also been shown previously that stripping rates can be enhanced when fluorinated gases are added to the oxygen plasma. A small percentage of fluorinated gas can bring about a large increase in removal rate for many resists because fluorine atomic reaction produces reactive sites on polymer backbone and small amounts of fluorine increase the concentration of atomic oxygen in the plasma. In Recipe 2, the flow rate of SF_6 is reduced to 30 $sccm$ and the power is increased to 200 W. The high flow rate of SF_6 gives higher etch rate compared to Recipe 2. However, the Recipe 2 gives smoother surface.

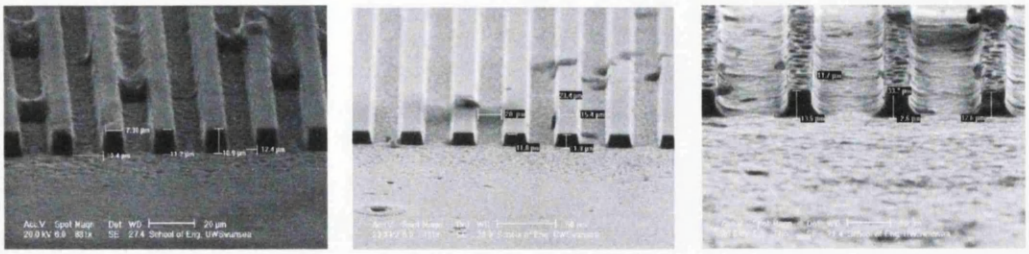

(a) (b) (c)

Figure 3.5: Straight micro-channel structures with width of 10 μm, 20 μm, 30 μm and a depth of 10 μm.

When the sample is etched first with Recipe 1 for 4 minutes and then with Recipe 2 for 4 minutes, micro-channels with depth of 1.25 μm are formed as shown in Figure 3.4. When the duration of flow is increased with SF_6 to 10 minutes, the micro-channel depth increases to 10 μm. However, the surface of 10 μm deep channels is not as smooth as 1.25 μm. Oxygen plasma treatment gives smoother surface. By using the positive photo-resist, we can get aspect ratio less than 0.33 at a width of 30 μm. The Figure 3.5 shows the different width of micro-channels with depth of 10 μm. The width of the micro-channels are 10 ,20 and 30 μm.

3.4.2 Elliptical Heat Spreader

The desired patterns are shown in Figures 3.6(a) and 3.6(b) which are designed with L-Edit Layout Editor. The patterns are transferred to a glass soda lime for masking purposes. The straight pattern is designed for electro-osmotic pumping area with 25 mm^2. There are 152 straight channels and each channel has a width of 40 μm and a length of 2.5 mm. The electrolyte is circulated in 8 large elliptical patterns which has a width of 1.12 mm each. The mask for the model in Figure 3.6(a) has no area for electrodes while the model in Figure 3.6(b) has two mask areas for golden electrodes of 750 μm wide. There are two circular structures on the left and right of the elliptical heat spreader which are about 2 mm in diameter working as an inlet and outlet of the elliptical heat spreader. The electrolyte is injected into inlet and fills up the elliptical micro-channels.

To fabricate elliptical heat spreader as in the Figure 3.6, a thick chemically and

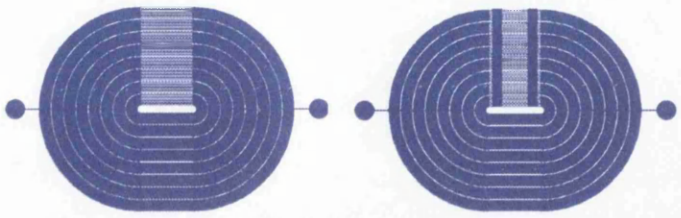

(a) (b)

Figure 3.6: Elliptical heat spreader mask.

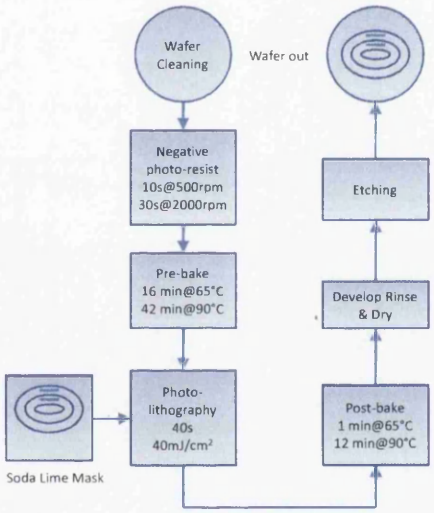

Figure 3.7: Flow chart of using negative photo-resist in elliptical heat spreader.

thermally stable photo-resist is essential to give deep etching to the silicon wafer. Negative epoxy based photo-resist, SU8 has been chosen due to its ability to give high aspect ratio etching to MEMS device structure [78]. It has high selectivity to silicon in the etching process. Therefore, SU8 is ideally suited for the fabrication of deep micro-channels for micro-fluidics and MEMS device [79].

The deep etching process of elliptical heat spreader is summarized in Figure 3.7. After the RCA cleaning, SU8 polymer is spun at a speed of 500 rpm for 10 s to spread the SU8 photo resist. This is necessary since the viscosity of the polymer is high. It is followed by 2000 rpm for 30 s to spread uniformly on the substrate. The thickness of the SU8 is about 125 μm. Lower initial bake temperatures allow solvent to evaporate out of the resist

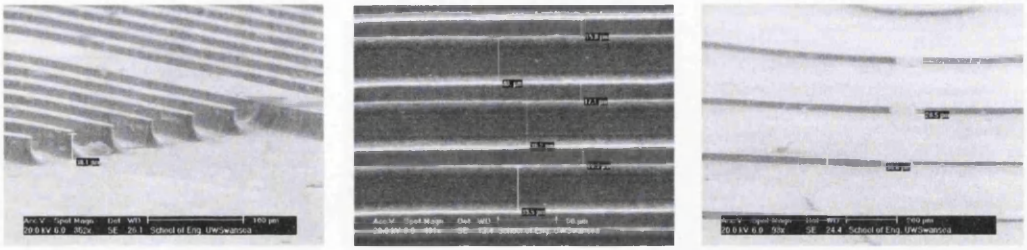

(a) (b) (c)

Figure 3.8: Depth of 30 μm.

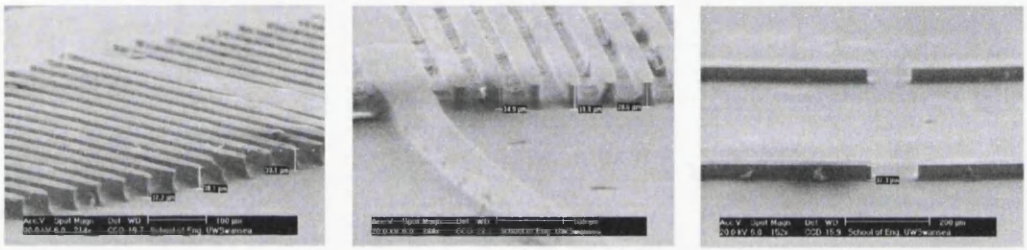

(a) (b) (c)

Figure 3.9: Depth of 38 μm.

layer at a more controlled rate, which results in better coating. This also reduces edge bead and results in better resist to substrate adhesion. The good mobility of SU8 results in self uniform spread during the soft baking process. Therefore, it is essential to adjust the horizontal position of hot plates prior to the baking process. Two step hot plate process is recommended here. The substrate gets heated to a temperature of 65 ^oC for 16 minutes and then at 90 ^oC for 40 minutes.

Then, silicon with negative photo resist is exposed to 355 nm UV light at intensity of 10 mW/cm^2 for 40 s. The exposure dose necessary for using SU8 is calculated as 400 mJ/cm^2. The substrate is post-baked again to 65 ^oC for 1 minute and then at 90 ^oC for 12 minutes. The exposed and subsequently cross linked portion of the film is rendered insoluble to developer.

After lithography process, the silicon substrate with patterned photo-resist is etched using the Reactive Ion Etching (RIE) system. The SF_6 and O_2 are used as reagents

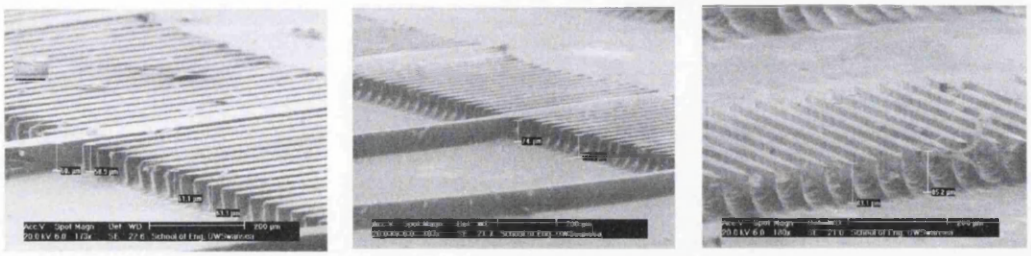

(a) (b) (c)

Figure 3.10: Depth of 60 μm, 75 μm and 83 μm depth.

Table 3.3: Etching recipes for difference depth

Channel depth (μm)	Recipe 1 (min)	Recipe 2 (min)	Aspect ratio
30	13	2	0.75
38	15	3	1
60	40	5	1.5
75	40	8.5	1.8
83	30	15	2

for plasma etching. The reagent flow rates used are shown in Table 3.2.

By increasing the duration of SF_6 flow rate from 13 minutes to 40 minutes, the channel depth is increased from 30 μm to 75 μm. By increasing the duration of O_2 flow rate from 5 minutes to 8.5 minutes, the channel depth is increased from 60 μm to 75 μm. Figure 3.8 shows channels with the depth of 30 μm. The width of the channel is 40 μm. Figure 3.9 shows channels with the depth of 38 μm. Figure 3.9(c) is the trench which is used to direct the electrolyte to the elliptical channels in the heat spreader from the inlet of electrolyte. Figure 3.10 shows channels with the depth of 60 μm, 75 μm and 83 μm. The SEM photos demonstrate that the SU8 negative photo-resist is capable to produce high aspect ratio channel. The aspect ratio of channel is calculated and shown in Table 3.3. The highest aspect ratio here is about 2 at a width of 40 μm. The Table 3.3 also shows the etching recipes for different depth of elliptical heat spreader.

The etch rates of the both etching Recipes 1 and 2 are studied here. The Recipe 2 has known etch rate of about 0.5 $\mu m/min$. In the channel depth of 30 to 83 μm, the etch rate of Recipe 1 is between 1.4 to 2.5 μm. The average etch rate is calculated and is shown

in Figure 3.11.

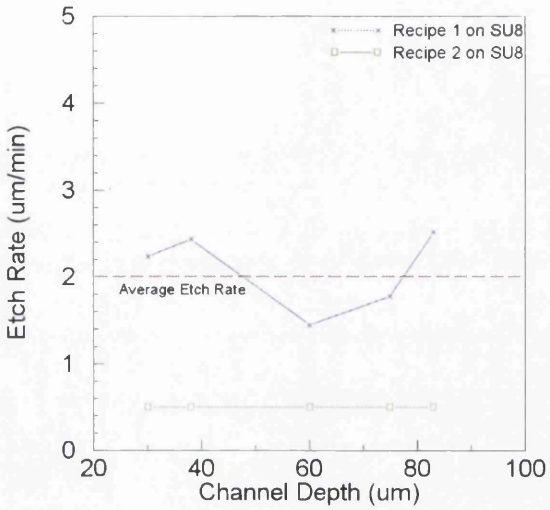

Figure 3.11: Etching rate of recipes on silicon with SU8 photo-resist.

The width of the elliptical micro-channels is 1.07 mm which is shown in Figure 3.12(a). Circular structure which works as the inlet of electrolyte has a diameter of 1.9 mm and is shown in Figure 3.12(b). The electrolyte is injected from this inlet into the heat spreader. The injected electrolyte is then directed to the elliptical micro-channels via the cross channel links as shown in Figure 3.12(c).

The Figure 3.13 shows the channels which are prepared for thin gold film electrodes. The width of thin film area is about 725 to 795 μm.

The Figure 3.14 and 3.15 show the photos of elliptical heat spreader and straight micro-channel structure respectively.

3.5 Electrical Isolation

The proposed electro-osmotic (EO) heat spreader is expected to be in close proximity to the microprocessor. Therefore a good electrical insulator is essential in designing a fully embedded EO heat spreader. The insulator is used for preventing the current penetration into the silicon substrate. In this thesis, silicon dioxide is chosen as the electrical insulator. The influence of silicon dioxide layer to the proposed designed will be discussed

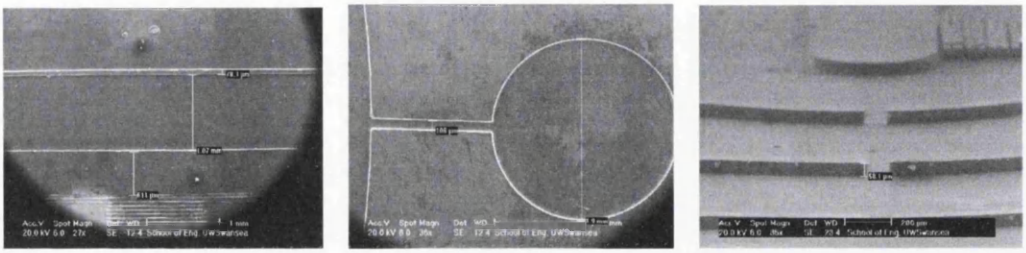

(a) (b) (c)

Figure 3.12: Other part of elliptical heat spreader.

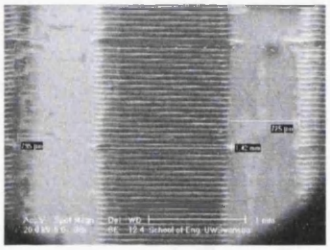

Figure 3.13: Electrodes area.

in detail in Chapter 4. In this section, the silicon dioxide fabrication process are discussed.

3.5.1 Thermal Oxidation

A chemical vapor deposition (CVD) process is often used to deposit silicon dioxide on wafer surfaces. However, the interface between the deposited oxide and the underlying silicon will not be as uniform as that formed by thermal oxidation. In addition, the latter provides a smoother topography and better quality surface which is suitable for wafer bonding process which is necessary to fabricate multi layered device chip architecture. Thus, it is the thermal oxidation that is usually employed in most device applications. Thermal oxidation of silicon is usually performed at temperatures between 800 ^oC to 1200 ^oC. Either wet oxidation or dry oxidation can be used. In case of wet oxidation, water vapor is used as oxidant and produces both silicon dioxide layer and hydrogen gas.

$$Si + 2H_2O \longrightarrow SiO_2 + 2H_2 \tag{3.1}$$

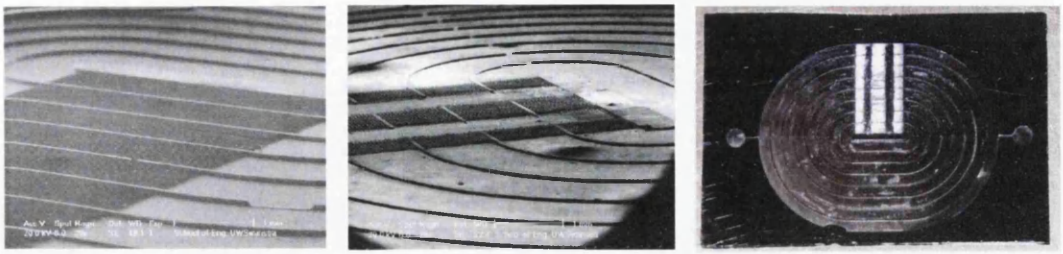

(a) (b) (c)

Figure 3.14: Elliptical heat spreader from (a) Mask shown in Figure 3.6(a). (b)Mask shown in Figure 3.6(b). (c)Full view.

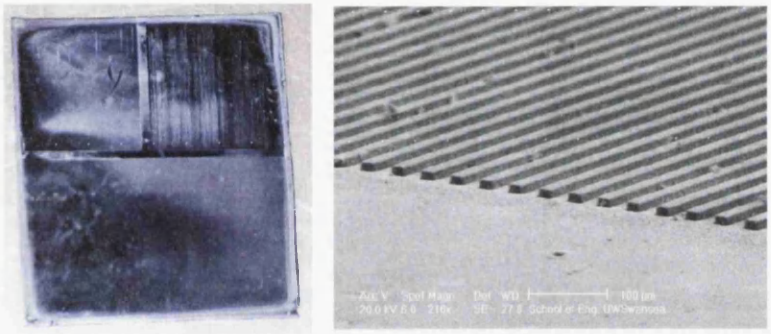

(a) (b)

Figure 3.15: Full view of straight channel structures.

In the present study, the dry oxidation process has been used. Here, molecular oxygen is used as the oxidant. As the result of the thermal oxidation process, a thin layer of the silicon dioxide is produced at the wafer surface [75].

$$Si + O_2 \longrightarrow SiO_2 \tag{3.2}$$

3.5.2 Electrical Isolator Result

Thermal furnace is heated to the desired temperature which is 1100 ^oC and kept at it until the temperature has stabilized. Meanwhile nitrogen gas is allowed to flow through the furnace to clean it. When the temperature of furnace has stabilized, oxygen is allowed to flow over the silicon surface in the furnace. Before loading sample onto the quartz rack

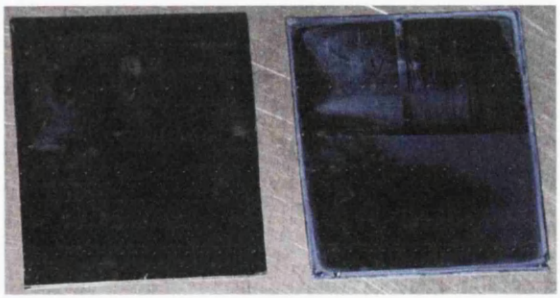

Figure 3.16: Straight channel with (left) and without (right) SiO_2.

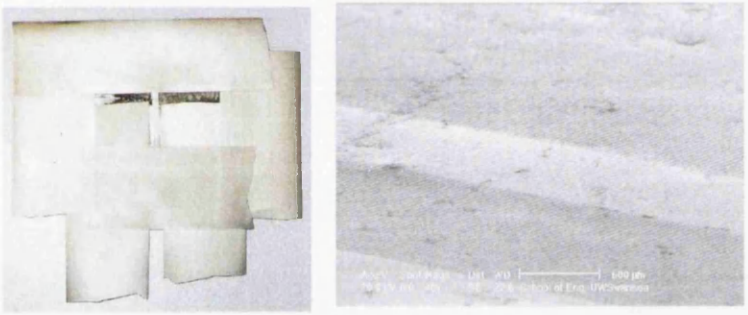

(a) (b)

Figure 3.17: (a)Masking for gold thin film deposition. (b)Gold thin film for electrodes in straight micro-channel structures.

horizontally in the furnace, the samples have to be cleaned with RCA cleaning procedures as described in Section 3.4. Silicon atoms on the surface of the sample chemically combine with oxygen atoms producing the silicon dioxide layer. The temperature of the furnace can be monitored with a thermocouple.

When the temperature of the furnace is stabilized, 1 l/min oxygen is allowed to flow over the silicon surface. After 4 hours, a silicon dioxide layer of thickness 250 nm is obtained. The right hand part of Figure 3.16 shows silicon dioxide deposition on silicon surface under thermal oxidation process.

It must be noted that, the cleanliness of samples is important to avoid the dust contamination which can affect the dielectric properties of the silicon dioxide. The dielectric performance of silicon dioxide between silicon substrate and electrolyte is tested in Chapter 4. The silicon dioxide layer is expected to prevent that the current flows through the silicon

substrate but not to the electrolyte.

3.6 Electrode Fabrication

A pair of electrodes sealed between the porous glass frit was used by Yao et al [23]. They connected the electrodes to an external potential difference to generate an electric field between the porous glass frit. Laser et al [25, 26] inserted platinum wire into the manifolds through channels of their micro-pump. These kinds of assembly are not compatible for embedded systems. Furthermore, the use of platinum also increases the cost of the micro-pump. Therefore gold is used here as electrode material for the proposed electro-osmotic heat spreader.

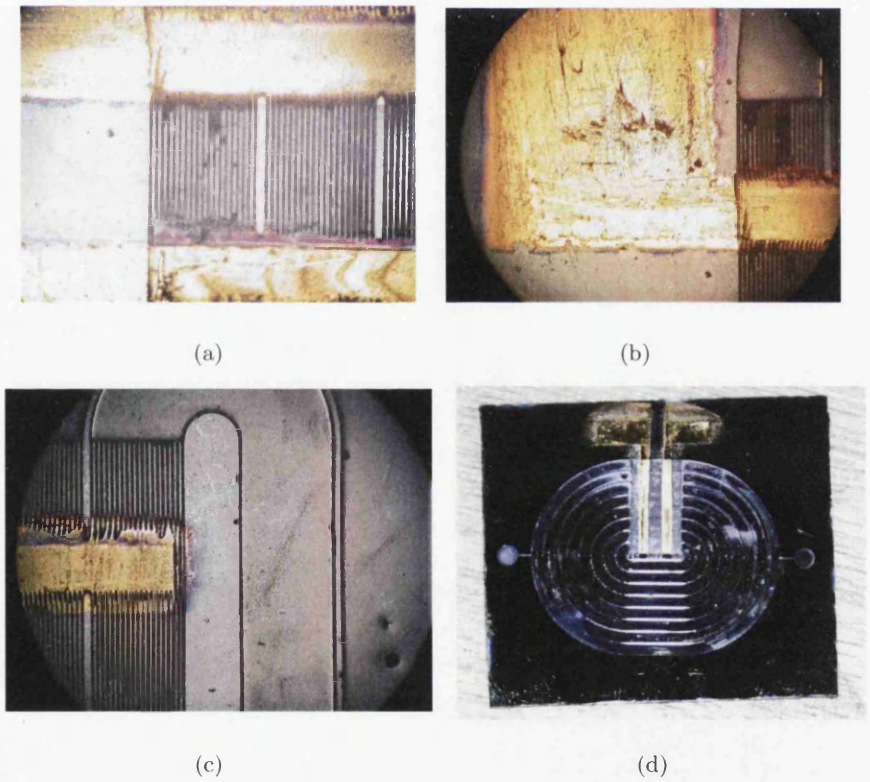

Figure 3.18: Thin gold film for electrodes in elliptical channels.

Gold is a very good electrical conductor and cheaper in cost compared to platinum.

Thin gold film is deposited via sputtering technique.

3.6.1 Sputtering Deposition

Sputtering technique is a physical vapor deposition (PVD) process which is used to deposit the gold thin film. Sputtering technique uses flux of atoms, which are released from a target material by bombarding it with chemically inert gases, such as argon. In strong electromagnetic field argon gas is ionized and plasma is produced. The positively charged argon atoms are accelerated and bombardment knocks out target atoms, which are then condensed on the predefined locations forming a thin film. Sputtered film has better adhesion on the substrate than evaporated film.

3.6.2 Electrode Fabrication Results

The substrate is masked before deposition process as in Figure 3.17(a). The vacuum of sputtering chamber is adjusted to $3 \times 10^{-1} Torr$. The argon gas is allowed to flow at about 1 l/min into the system. The voltage of 1 kV and current of 30 mA is applied to produce a plasma layer between the target and silicon substrate. The duration for depositing a pair of electrodes is 15 minutes. The thickness of the thin film is about 1 μm. Figures 3.17(b) and 3.18 show the samples which are deposited with thin gold film in straight channel structure and elliptical heat spreader respectively.

3.7 Bonding

After fabrication of micro-channels, electrical isolator and electrodes, the electro-osmotic heat spreader is bonded to seal the electrolyte and prevent it from leaking. The development of MEMS technology eases the bonding techniques. Silicon bonding and anodic bonding have been investigated in this thesis. The silicon bonding is beneficial for co-integration of electro-osmotic heat spreader into microprocessors and multi-chip modules. However, anodic bonding is needed for monitoring the particle movement in flow measurement.

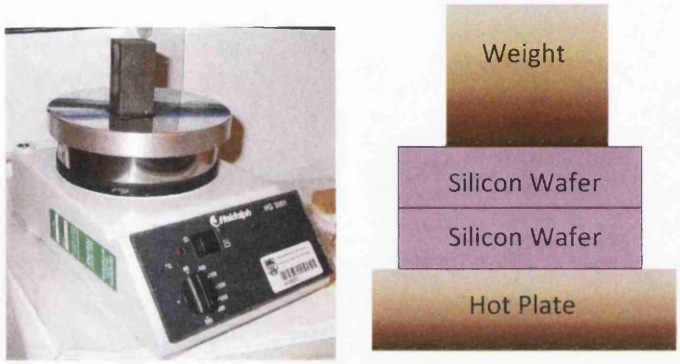

(a) (b)

Figure 3.19: Silicon-Silicon bonding.

3.7.1 Silicon Direct Bonding

Silicon direct bonding is used here to seal two silicon wafers together. It utilizes the reaction between hydroxyl groups at the surface of oxide layer of two silicon wafers. Before bonding, the substrate is cleaned to remove the thin oxide layer and some fraction of ionic contaminations. After the wafers are cleaned, they are brought to contact at room temperature. To make the bonding stronger, the wafer is heated as in Figure 3.19 under pressure from a weight to make a permanent bond. Large and smooth surface is essential to give a perfect bond [80].

3.7.2 Anodic Bonding

In anodic bonding, the glass and silicon are bonded by heating to a specific temperature at which glass becomes electrically conductive. However, the bonding temperature is maintained below the glass transition temperature, T_g so that there is no macroscopic deformation during the bonding process. When the bonding temperature is reached, a bonding voltage is applied. This activates the mobile cations in the glass to move away from silicon-glass interface towards the cathode. This creates a depletion layer in the glass near the interface with the anode material. The two materials are pressed into contact by electrostatic pressure resulting in the movement of cations. Ultimately, permanent bond

gets formed by anodic oxidation of the anode material at the interface [81]. The experiment of anodic bonding is shown in Figure 3.20.

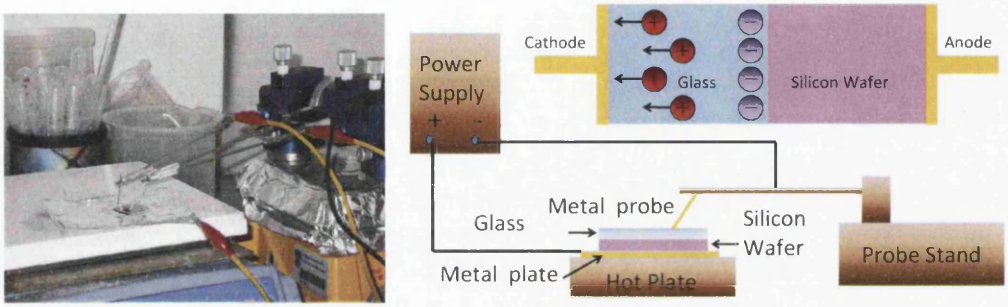

(a) (b)

Figure 3.20: Anodic bonding.

3.7.3 Bonding Results

Figure 3.21(a) shows the result of silicon-silicon direct bonding. Before bonding, the silicon substrate is immersed in 1:50 solution of hydrogen fluoride (HF): DI water (H_2O) at room temperature, in order to remove the thin oxide layer and some fraction of ionic contaminations. After the wafers are cleaned, they are brought into contact at room temperature. To make the bonding stronger, the wafers are heated to a temperature of 200 ^oC for 24 hours before cooling them back to room temperature. Smooth surfaces and large areas are easier to bond.

Figure 3.21(b) shows the result of silicon glass or anodic bonding. The substrates were heated to a temperature of 400 ^oC. When the bonding temperature is reached, a bonding voltage of 600 V is applied. Then, the silicon and glass substrates were pressed into contact by electrostatic pressure resulting in movement of cations. Ultimately, permanent bond is formed by anodic oxidation of the anode material at the interface. However the glass sometimes cracks after anodic bonding. This can be solved by cooling down the temperature slowly. However, both techniques are not reliable to keep the electrolyte from leaking. Therefore, both bonding techniques need to be further investigated to ensure the system is safely sealed.

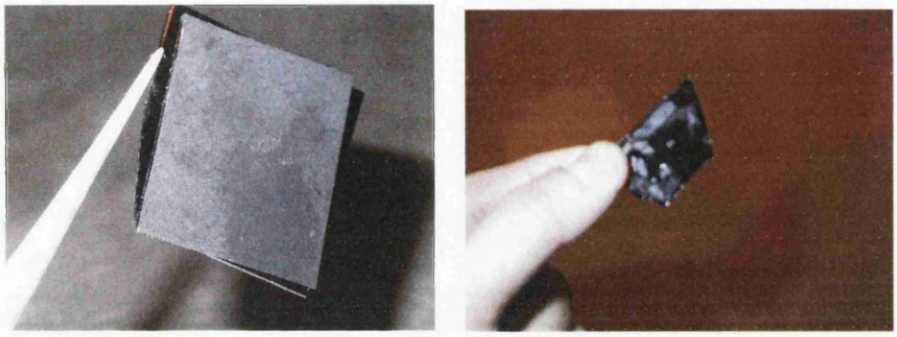

(a) (b)

Figure 3.21: (a)Silicon-silicon bonding. (b)Anodic bonding.

3.8 Summary

In this chapter, an integrated EO based heat spreader has been proposed. The liquid was driven by EO force and forced to circulate in the elliptical structure etched on to the heat spreader surface.

The fabrication processes of the EO heat spreader were discussed in this chapter. The lithography and etching processes were able to produce both shallow and deep micro-channels. Recipes of these processes are summarised in Appendix A.1. The shallow straight micro-channels have the depth of 1.25 and 10 μm and the width of 10, 20 and 40 μm. With the recipes, deep micro-channels from 30 to 83 μm were fabricated. The elliptical micro-channels and straight micro-channels in the heat spreader in Section 3.4.2 have a width of 1.07 mm and 40 μm respectively. The samples produced here were used in flow measurements in Chapter 5. The straight micro-channel part in the elliptical heat spreader were used as an electro-osmotic micro-pump to force the electrolyte to circulate in the elliptical micro-channels.

A layer of silicon dioxide with a thickness of 250 μm was deposited to isolate microprocessor and electro-osmotic pump. The effect of using silicon dioxide as electrical isolation layer will be explained further in Chapter 4.

A pair of thin gold film with a thickness of about 1 μm was deposited across the micro-channels works as electrodes in electro-osmotic pump. External voltage source is

applied to the electro-osmotic pump via these thin gold films.

Two bonding techniques have been demonstrated. These are silicon-glass and silicon-silicon bonding. The silicon-glass bonding was employed in flow measurements in Chapter 5 for particle movement monitoring while silicon-silicon bonding is employed in temperature measurements in Chapter 7. However, both techniques need to be perfected to avoid the leakage of electrolyte which will pose a problem of integration in the microprocessor.

Chapter 4

Electrical Isolator

4.1 Introduction

The external potential difference in the electro-osmotic (EO) micro-pump produces current that drives the electrolyte. In the past, EO pump has been designed to operate externally [1] as shown in the Figure 4.1 from the microprocessor to avoid current interference between the devices in the microprocessor and the micro-pump. Such a design is complex in wiring and piping.

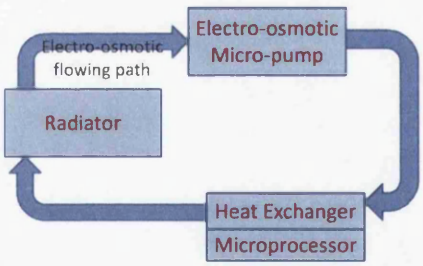

Figure 4.1: Architecture of electro-osmotic cooling system from Jiang et al [1].

The EO heat spreader proposed in this thesis is fabricated at the back of microprocessor. (refer to Figure 3.1). The integration of EO heat spreader in the microprocessor can remove the heat and reduce the complexity of wiring and piping. However, due to both EO heat spreader and microprocessor sharing the same silicon substrate, the current

of the EO heat spreader can interfere with the devices in the microprocessor. Therefore, it is very important to choose a good insulator to prevent the current of the integrated EO heat spreader from penetrating through the silicon and affecting the performance of the microprocessor. This chapter describes how an insulator layer can be used to prevent the current from penetrating silicon substrate and force that current to flow through the electrolyte instead.

4.2 Silicon and Isolation Materials

Table 4.1: Properties of Si, SiO_2 and Si_3N_4.

Properties	Si	SiO_2	Si_3N_4
Thermal Conductivity (W/mK)	149	1.4	30
Dielectric Constant	11	3.9	7.5
Zeta Potential at pH 7 (Refer to Figure 5.3) (mV)	-5	-35.5	-28
Electrical conductivity (Sm^{-1})	1.2×10^{-3}	10^{-7} to 10^{-14}	10^{-10}

Silicon nitride (Si_3N_4) has been used in the past by Laser et al [25, 26] as an isolator between the microprocessor and a micro-pump. The reason to use silicon nitride is because it has moderate thermal conductivity, high dielectric constant and low electrical conductivity as shown in Table 4.1. However, there are some works showing Si_3N_4 has zeta potential of -28 mV at pH 7 which is considered unstable [2, 82]. At small zeta potential, there are fewer positive charges in the diffuse layer. As a result, as a potential difference is applied across the diffuse layer, the charge does not have enough strength to drag along the electrolyte molecules and give small fluid flow in the channel.

Therefore, silicon dioxide is considered in the present study. It has zeta potential of -35.5 mV in the electrolyte with pH 7 [3]. This zeta potential value is good enough to attract more charges to the diffuse layer. Large amount of charges in the diffuse layer can drag more electrolyte molecules and give larger flow rate. Silicon dioxide in the form of glass or quartz is also widely used in micro-fluidic systems [56, 83] due to its good properties in generating stable flow rate.

In addition, it is also easy to produce a silicon dioxide thin film on a silicon substrate through micro-fabrication process. Therefore, it has been used as an oxide material

in some electronic devices like metal-oxide-semiconductor field-effect transistor (MOSFET) [84]. The band gap energy of 8.1 eV in silicon dioxide also makes it a superior electric insulator as shown in Table 4.1 [85, 86, 87]. In fact, silicon dioxide is a good choice of isolation material.

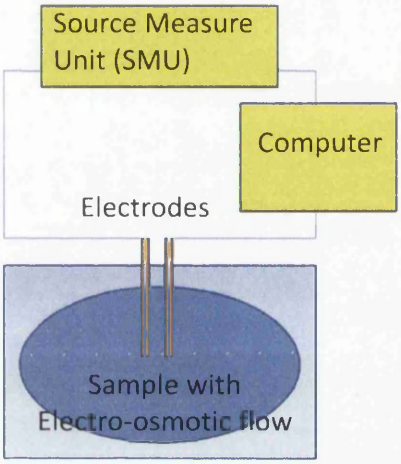

Figure 4.2: IV Measurement Setup.

4.3 Experiment Setup

In this section, current-voltage (IV) experiments are conducted to study the effect in the presence of a silicon dioxide layer on a silicon substrate with micro-channel structure. A silicon micro-channel sample is connected to a source measurement unit (SMU) as shown in Figure 4.2 with thin gold film electrodes. The SMU produces potential difference to the sample. Experiments are conducted to measure the current flow in different environments: KCl solution, DI water or having no electrolyte in silicon heat spreader at all. The experiments are repeated in the silicon micro-channel structure with silicon dioxide layer. The total current, I_t and total voltage V_t are recorded and plotted to an IV graph. The measured total current is used to calculate the total impedance (Z_t) of entire system in different environments. The relationship between I_t, V_t and Z_t is:

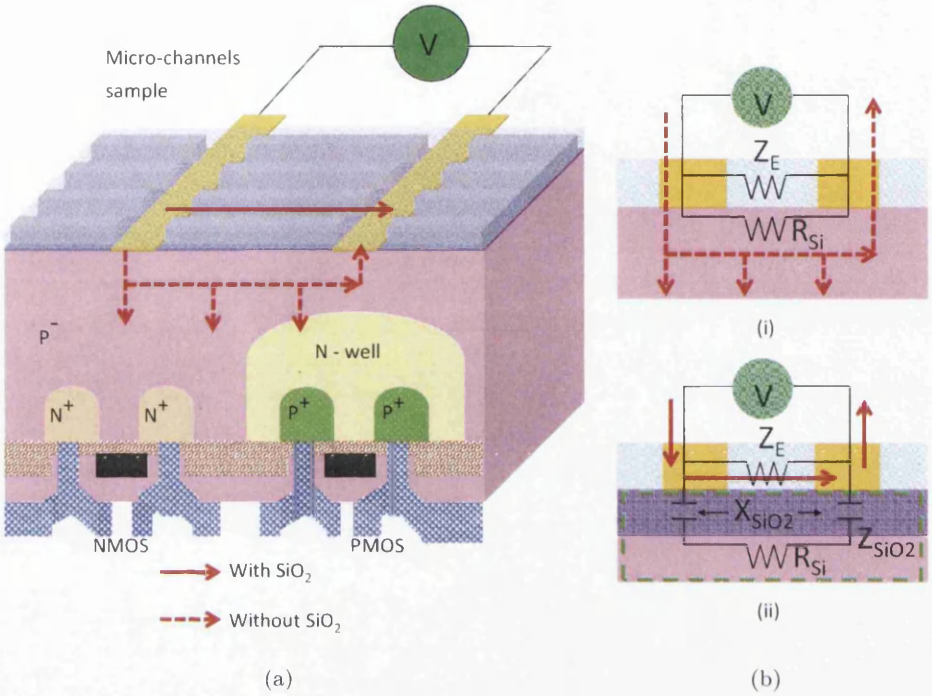

Figure 4.3: (a)Current path in silicon electro-osmotic pump and microprocessor. (b)Heat spreader with (bottom) and without (top) SiO_2 equivalent circuit.

$$Z_t = \frac{V_t}{I_t} \tag{4.1}$$

The total impedance obtained is then used to calculate the resistances and currents in different mediums: electrolyte, silicon substrate and silicon substrate with SiO_2 layer. The heat spreader equivalent circuits without and with silicon dioxide layer are shown in Figure 4.3(i) and (ii). Their total impedance in terms of electrolyte impedance (Z_E), silicon substrate resistance (R_{Si}) and silicon substrate with SiO_2 layer impedance, Z_{SiO_2} are:

$$Z_t = \frac{R_{Si} Z_E}{R_{Si} + Z_E} \tag{4.2}$$

and

$$Z_t = \frac{Z_{SiO_2} Z_E}{Z_{SiO_2} + Z_E} \tag{4.3}$$

where

$$Z_{SiO_2} = \sqrt{(2X_{SiO_2})^2 + R_{Si}^2} \tag{4.4}$$

and X_{SiO_2} is the reactance of silicon dioxide. The impedance of electrolyte, Z_E can be obtained at Equation 2.33. The current flowing through the mediums of electrolyte, silicon and silicon dioxide can be obtained by using Equation 4.1. Finally, the ratio of electrolyte current (I_E) to substrate current (I_{Si} or I_{SiO_2}), R is determined by using Equation 4.5 to differentiate the effectiveness of using SiO_2 as an isolation layer.

$$R = \frac{I_E}{I_{Si}} \tag{4.5}$$

4.4 Measurements without SiO_2 Layer

In this section, a silicon heat spreader with no silicon dioxide layer was used in the experiments. Here, native oxide is neglected because its thickness is thin (about 10 Armstrong). Thus, if no SiO_2 is used or the SiO_2 layer thickness is too small, the barrier strength of SiO_2 will not be sufficient to prevent electron penetration from the electrodes of EO pump to the silicon substrate [88].

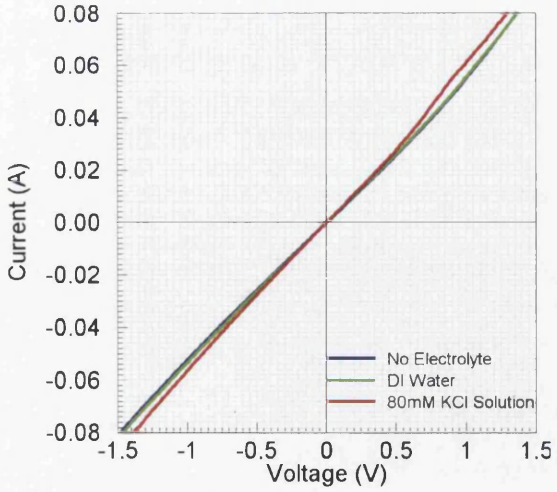

Figure 4.4: IV characteristics of the elliptical heat spreader without SiO_2.

Table 4.2: Elliptical heat spreader without SiO_2. Current and resistance distributions.

Case	V (V)	I (mA)	Z_t (Ω)	R_{Si} (Ω)	Z_E (Ω)	I_{Si} (mA)	I_E (mA)	R
Dry	1	54.8	18.24	18.24	infinity	54.8	0	0.00
DI	1	55.4	18.05	18.24	1732.80	54.8	0.6	0.01
KCl	1	61.2	16.34	18.24	156.86	54.8	6.4	0.11

Experiments are carried out on silicon heat spreader samples with different electrolytes, including DI water and 80 mM KCl solution. Experiments are also carried without the presence of any electrolyte. The current flowing through the micro-channels is measured and plotted against the potential difference as shown in Figure 4.4. The currents measured are 54.8 mA, 55.4 mA, and 61.2 mA at 1 V for cases without electrolyte (Case Dry), with DI water (Case DI) and with KCl solution (Case KCl) respectively. The parameters of Z_t, R_{Si}, Z_E, I_{Si}, I_E and R are determined by using Equations 4.1 to 4.5 and recorded in Table 4.2.

To calculate R_{Si}, Z_E is maintained at infinite resistance (no electrolyte). Thus, the total impedance of the system is equivalent to the silicon resistance. After determining the silicon resistance, the impedance of DI water and KCl solution are also calculated by using Equations 4.1 and 4.2. As seen in Figure 4.4, the current of silicon with no electrolyte (Case Dry) is increased proportional to the applied voltage. This is obvious that there are no capacitance which is induced by the insulation on the silicon surface. The linearity of IV curve which is shown in Figure 4.4 shows the system with silicon surface is almost resistive.

The Table 4.2 shows that the impedance of silicon, DI water and KCl solutions are 18.24, 1732.80 and 156.86 Ω respectively. Both impedance values of electrolyte are much higher than silicon. Thus, more current of flows through the silicon substrate.

As seen in Table 4.2, the current flowing through the silicon substrate is about 54.8 mA while the currents flowing through the DI water and KCl solution are 0.6 and 6.4 mA respectively. The ratios of electrolyte current to substrate current of both DI and KCl are considered small. In other words, the total current is almost identical to the substrate current and almost no current flows through the electrolyte. It is also apparent from Figure 4.4 that the current is almost identical with and without the presence of the electrolytes.

This clearly demonstrates that without electrical insulation, the chances of damage to the microprocessor beneath the heat spreader are very high.

4.5 Measurements with SiO_2 Layer

In this section, a SiO_2 layer which has thickness of 250 nm is deposited via thermal oxidation process on a silicon heat spreader. This thickness is expected to prevent the current tunneling to the silicon wafer. The measured current and voltage are plotted in Figure 4.5.

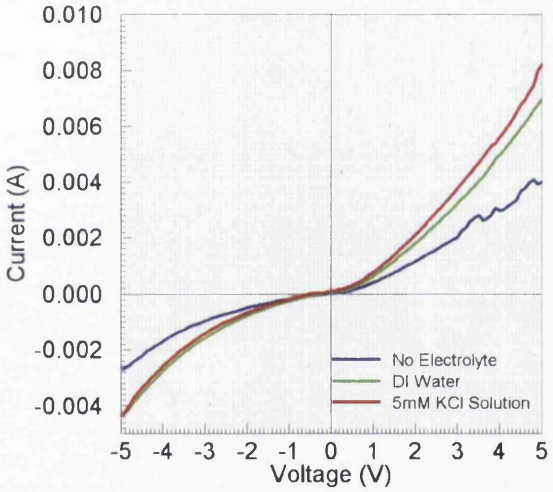

Figure 4.5: IV characteristics of the elliptical heat spreader with SiO_2.

From Figure 4.5 and Table 4.3, it is clear that the tunneling current is significantly reduced to a value of 0.38 mA with no electrolyte on an insulated silicon wafer, at a potential difference of 1 V. The currents in the presence of the electrolyte are also significantly reduced to 0.61 mA for DI water and 0.74 mA for KCl solution.

Table 4.3: Elliptical heat spreader with SiO_2. Current and resistance distributions.

Case	V (V)	I (mA)	Z_t ($k\Omega$)	Z_{SiO_2} ($k\Omega$)	Z_E ($k\Omega$)	I_{SiO_2} (mA)	I_E (mA)	R
Dry	1	0.38	2.63	2.63	Infinity	0.38	0	0.00
DI	1	0.61	1.64	2.63	4.35	0.38	0.23	0.61
KCl	1	0.74	1.35	2.63	2.77	0.38	0.36	0.94

As seen in Table 4.3, the ratios of electrolyte current to substrate current of both Case DI and KCl are higher than the system without insulation which is demonstrated in the previous section. The ratio prove that silicon dioxide is capable to reduce the current that flows through the silicon substrate. The ratio becomes apparent when voltage is increased (see Figure 4.5). The ratio of electrolyte current to substrate current can be improved by ensuring the cleanliness of silicon substrate before loading it into a furnace for the thermal oxidation. The dust contamination under the silicon dioxide layer affects the dielectric properties of silicon dioxide.

Due to the dust contamination in the system without electrolyte (Case A), as the voltage is increased from zero in Figure 4.5, the current can hardly flow through the device in the beginning. It is because voltage is needed to overcome the barrier of the silicon substrate with SiO_2 layer. However, as soon as the barrier is overcame, the current increases proportionally to the voltage. The silicon dioxide layer is no longer enough to block the current from flowing into the silicon. This also happens with negative voltage.

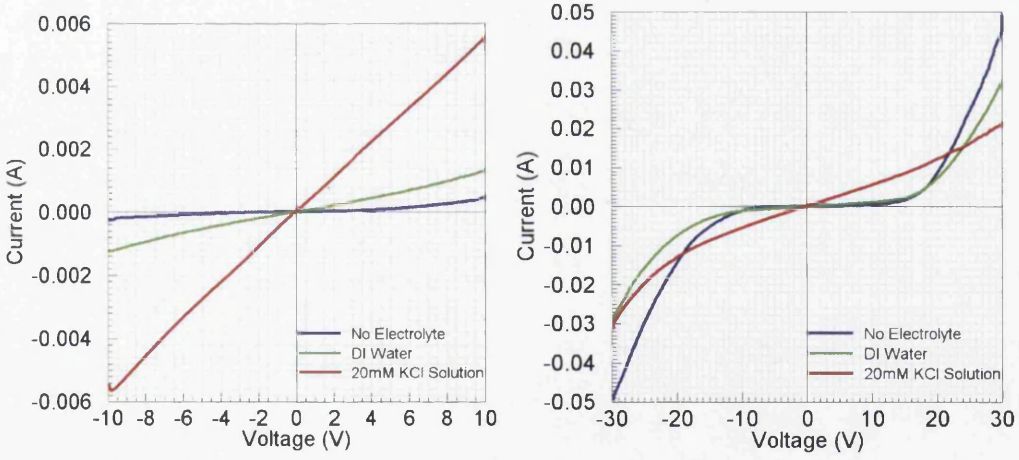

(a) (b)

Figure 4.6: IV characteristics of the straight micro-channels with SiO_2 in voltage range of (a) $\pm 10\ V$. (b) $\pm 30\ V$.

Next, another sample with silicon dioxide is used in IV measurement. As seen in Table 4.4, the tunneling current is about 6 μA at a potential difference of 1 V. With the DI water and 20 mM KCl the current is about 106 μA and 546 μA respectively. Again,

Table 4.4: Straight micro-channels structure with SiO_2. Current and resistance distributions.

Case	V (V)	I (μA)	Z_t ($k\Omega$)	Z_{SiO_2} ($k\Omega$)	Z_E ($k\Omega$)	I_{SiO_2} (μA)	I_E (μA)	R
Dry	1	6	160.00	160.00	Infinity	6.00	0	0.00
DI	1	106	9.40	160.00	9.90	6.00	100.00	16.67
KCl	1	546	1.83	160.00	1.85	6.00	540.00	90.00

the current is further reduced compared to the previous experiments. The parameters of Z_t, Z_{SiO_2}, R_{Si}, Z_E, I_{Si}, I_E and R are determined and recorded in Table 4.4.

The high impedance of SiO_2 layer, 160 $k\Omega$ obtained only allow 6 μA to flow through. It is clear indication that SiO_2 is a suitable insulator. The impedance of DI water and KCl solution obtained are only 9.9 $k\Omega$ and 1.85 $k\Omega$ respectively. The high impedance offered by SiO_2 deflects more current to flow through the electrolytes. As seen in Table 4.4, the ratio of the electrolyte current to substrate current is the largest compared to the previous experiments.

The IV characteristic of sample with SiO_2 at voltage range from -30 V to 30 V is also measured and shown in Figure 4.6(b). The current of samples without electrolyte (Case A) can hardly flow through the silicon substrate at small voltage. Higher voltage is needed to overcome the barrier of the silicon substrate with silicon dioxide compared with the sample which has defect of dust contamination. Consequently, the current only rapidly increased at voltage about 18 V. The Figure 4.6(b) also shows that, at the voltage of 18 V, the current over the device is about 4.5 mA.

The Table 4.4 shows that the current flow in the KCl solution is higher than the DI water. This is because at higher concentrations of electrolyte, the capacitance of double layer near the electrodes is large and more current are needed to charge the double layer. As a result, high current flows through highly concentrated electrolyte. As seen in Figure 4.6, the current of the sample with KCl solution is increased proportional to the voltage. However, the current obtained from the sample with DI water is small in the beginning because of the charging process occur in the double layer near the electrodes. At higher voltage, the current is increased proportional to the voltage until oxide breakdown occurs in the silicon dioxide at 18 V.

4.6 Summary

A thin silicon dioxide layer of 250 nm was experimentally tested for its electrical isolation properties in the context of electro-osmotic heat spreaders. It is clear that, about 54.8 mA of current strays into the silicon substrate, if no insulation between the microprocessor and the electro-osmotic pump is used. However by using a silicon dioxide layer as an insulator, this current can be reduced to just 6 μA. This indicates that using silicon dioxide as an insulator forces the current to flow through the electrolyte rather than through the silicon substrate. In addition, since the zeta potential of SiO_2 is higher than other competing insulators, it will be extremely useful in electro-kinetic devices that need faster flow rate.

Chapter 5

Flow Measurements

5.1 Introduction

In this chapter, the flow rate of electrolyte which is driven by electro-osmotic force is determined using a velocimetry system. This system is used to monitor the movement of particles in the electrolyte. Velocities of particles are calculated from the images which are taken by a CCD camera. Following that, volumetric flow rates and zeta potential are calculated. The influence of parameters, including external potential, zeta potential and cross sectional area are discussed in this chapter.

5.2 Flow Rate Calculation

Volumetric flow rate, FR is the product of average velocity of an electrolyte, $\overline{u}$ and cross sectional area of channel, A. It describes the volume of electrolyte which passes through a section per unit time. The volumetric flow rate can be written as:

$$FR = A.\overline{u} \tag{5.1}$$

where average velocity is the displacement Δx that travelled by an electrolyte over a time interval Δt:

$$\overline{u} = \frac{\Delta x}{\Delta t} \tag{5.2}$$

Various mechanical velocimetric flow meters have been used over the years to measure the flow rate of piping systems. However the moving part in the mechanical flow meter is not reliable. Therefore optical flow meters have been invented recently because they have no moving parts. One of the optical velocimetry methods is called Particle Image Velocimetry (PIV) which involves measuring the velocity field in two dimensions of particles seeded in a flow.

Santiago et al [89] demonstrated the first application of micro-PIV in EOF with fluorescent seed particles by measuring the velocity field. In the micro-PIV system, a pair of laser pulses with time interval of nano seconds are fired to a light-sheet in a flow system. The images of particles lying in the light-sheet are recorded on a digital camera. Those images are divided into subsections called interrogation areas (IA). The IA from each image frame then are cross-correlated with each other pixel by pixel. The correlation produces a signal peak, identifying common particle displacement. The displacements of those particles are converted to velocity using the time interval between the pair of laser pulses. This technique is also used by Kim at el [4].

Due to short time interval between the laser pulses, high speed digital camera is required to capture the two images and store in the computer for cross correlation analysis before the next pair of images is being taken. However, the speed of the digital camera is a limitation in the recent technology. Therefore, an alternative way of velocimetry measurement is designed in this chapter to measure the velocity of particles in the electro-osmotic flow. Here, the speed of digital camera has no impact in capturing two images. The details of velocimetry system are explained in Section 5.3

5.3 Velocimetry System Setup

A velocimetry system is set up as shown in Figure 5.1 to measure the velocity of electrolyte which is seeded with particles. The micro-channel samples get filled with electrolyte and particles and covered by a transparent glass slide for visual examination

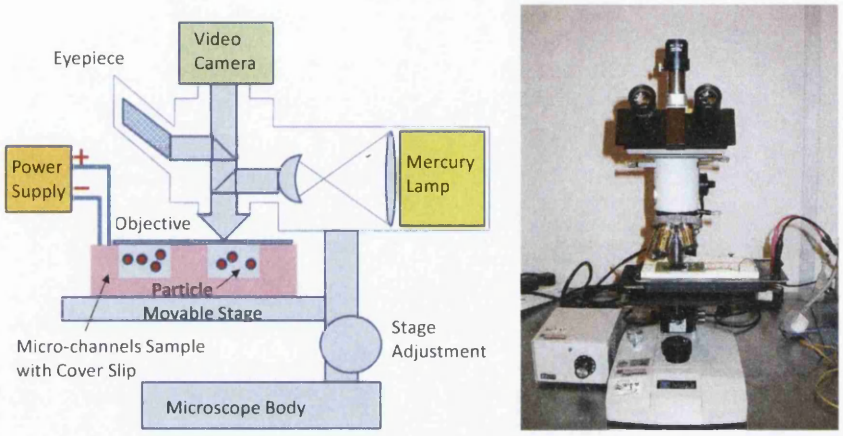

(a) (b)

Figure 5.1: Velocimetry System Setup.

of the particle movement. Then the samples are placed under a microscope as shown in Figure 5.1. When a potential difference is applied to the straight micro-channels, the particles in the electrolyte are moving towards the negative electrode in the micro-channels. The movements of particles are recorded in the video with a CCD digital camera which is attached onto the microscope. The frame rate of the video is 25 frame per second.

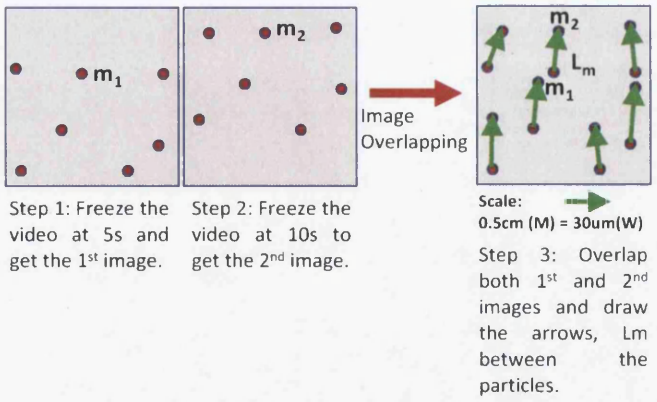

Figure 5.2: Procedure to get the L_m.

The videos taken are then analyzed in a computer. When the video is played, the images with clear vision of particle are frozen with a specific time interval (Δt) (see Figure

5.2). The locations of the particles in both images are marked as m_1 and m_2. The images with marked particle locations are overlapped for comparison. A line, L_m is then drawn between m_1 and m_2 and its length is calculated with the equation below:

$$L_m = \sqrt{(x_{m_1} - x_{m_2})^2 + (y_{m_1} - y_{m_2})^2} \tag{5.3}$$

The L_m is the distance that was travelled by a particle in a given time duration. However, this distance cannot be taken as the actual travelling distance of the particle. The L_m has to be correlated to obtain an actual distance. Thus, to get an actual travelling distance of the particle, the L_m has to be multiplied with a correlation parameter, RF. The correlation parameter can be obtained from a scale of an image. For example, scale of the image in Figure 5.2 is: every 0.5 cm of the image scale (M) is equivalent to 30 μm in actual dimension (W). Both parameters M and W are used to calculate correlation parameter. The correlation parameter is:

$$RF = \frac{W}{M} \tag{5.4}$$

The actual particle displacement, Δx, can be obtained by the product of representative fraction and L_m.

$$\Delta x = RF \times L_m \tag{5.5}$$

Finally, the velocity of the particle is calculated by dividing the particle displacement with time interval (refer to Equation 5.2). The average velocity, $\overline{u}$ of a group of particles is determined as:

$$\overline{u} = \frac{1}{n}\sum_{i=1}^{n} u \tag{5.6}$$

where n is the total number of particles. The average velocity is then used to calculate the volumetric flow rate of different micro-channel samples.

The mean deviation and experiment error are determined to make sure the accuracy of the measurements is maintained. The mean deviation, $|D|$ describes the absolute value of the difference between each particle velocity and average velocity. It is written as:

$$|D| = \frac{1}{n}\sum_{i=1}^{n}|u - \overline{u}| \tag{5.7}$$

The experiment error, E_r is the fraction of mean deviation to the average velocity in percentage. It is written as:

$$E_r = \frac{|D|}{\overline{u}} \times 100 \tag{5.8}$$

The calculation of L_m, RF, Δx, $\overline{u}$, $|D|$ and E_r are shown in details in Appendix C.1.

In the present velocimetry system, no laser pulses are used. Therefore, high speed digital camera is not needed. Particles distances are determined from a video with 25 frames per second.

5.4 Electrolytes

The choice of electrolyte pH used in the heat spreader is essential to drive the flow. At a large pH value, the electrolyte contains more OH^- ions. The ions in the electrolyte will flow to the electrode when external potential difference is employed. The flowing ions drag along with the electrolyte molecules and generate flow in the channel. However, high ionic concentration of electrolyte such as Potassium Chloride (KCl) solution will result in the electrolysis phenomena. Due to electrolysis, bubbles are generated and it gives an adverse pressure. The bubbles will also block the narrow channels. Therefore, in the present work, de-ionized (DI) water with pH 7 is chosen as working fluid in the system. It will generate smaller amount of bubbles compared to KCl solution. Besides, DI water is easier and cheaper to acquire.

5.4.1 Zeta potential Estimation

The zeta potential is important to determine the electro-osmotic (EO) velocity. The zeta potential of a surface is influenced by the pH of electrolyte. As the pH value increases, the negative charges on a surface also increase. The negative surface charges

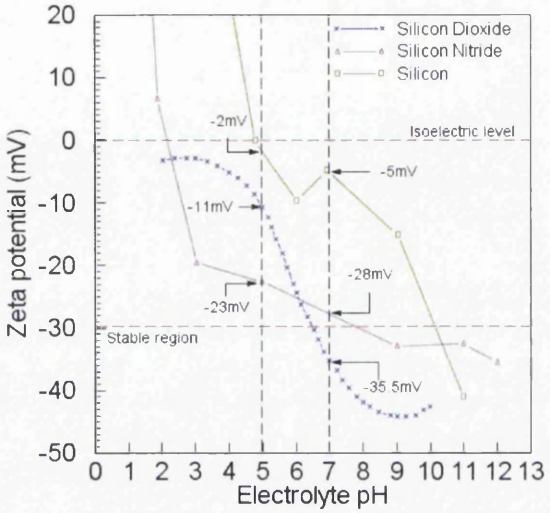

Figure 5.3: Zeta Potential of Si, SiO_2 and Si_3N_4 in different pH of electrolyte from Wu et al and Matec Applied Science [2, 3].

attract more positive charges in the electrolyte to the diffuse layer and give large zeta potential. Large zeta potential over the diffuse layer tend to give large EO velocity when electric force is employed.

As seen in Figure 5.3, the silicon and silicon dioxide surfaces have zeta potential of -5 mV and -35.5 mV respectively at pH 7. It is expected that the silicon dioxide surface can generate higher electro-osmotic velocity than silicon surface when both surfaces are in contact with DI water. Figure 5.3 also shows that silicon has isoelectric point (pI) at pH 2. At this point, the silicon surface has zero surface charge. Thus, no EO flow can be generated at this point.

In the next section, silicon and silicon dioxide surfaces are prepared for flow experiments. The zeta potentials of both surfaces can be estimated by using Helmholtz Smoluchowski equation:

$$\overline{u}_{HS} = \frac{\zeta \epsilon E_1}{\mu} \tag{5.9}$$

where μ and ϵ are the viscosity and dielectric properties of electrolyte respectively. The Helmholtz Smoluchowski (HS) velcoity, $\overline{u}_{HS}$ can be obtained experimentally under the electric field of E_1. The electro-osmotically driven flow is assumed to be steady and fully

developed with zero pressure gradient. Equation 5.9 is limited to small EDL thickness over a large channel width. The estimated zeta potential will be used in the numerical simulation [13] in Chapter 10.

5.5 Sample Preparation

Table 5.1: Experimental samples.

Samples	Surface	Width (μm)	Depth (μm)	Pumping distance (mm)	Applied Voltage (V_{dc})
Straight A	Si	30	0.5	10	400
Straight B	SiO_2	30	10	10	10
Straight C	SiO_2	30	10	10	20
Straight D	SiO_2	30	10	10	40
Straight E	SiO_2	30	10	5	5
Elliptical A	Si	40	0.5	5	50
Elliptical B	Si	40	0.5	5	400
Elliptical C	SiO_2	40	30	2	5
Elliptical D	SiO_2	40	30	2	AC Voltage

A few samples of straight micro-channel structures (Straight A to Straight E) and elliptical heat spreaders (Elliptical A to Elliptical D) with dimensions as shown in Table 5.1 were used to illustrate the principle of electro-osmotically driven flow. The surfaces of silicon, Si, and silicon dioxide, SiO_2, are used in the experiments.

The straight micro-channel structure samples have the cross sectional areas of $15\mu m^2$ and $300\mu m^2$. Two electrodes are deposited 10 mm apart across the micro-channels. The distance between both electrodes is defined as pumping distance. The elliptical heat spreader samples have the cross sectional areas of 20 μm^2 and 1200 μm^2 with electro-osmotic pumping distances of 5 mm and 2 mm respectively.

Those samples have two reservoirs to supply the electrolyte from and for, providing particles for the experiments. Before starting an experiment, the samples are rinsed with de-ionized water to remove any contaminants. The clean samples are then connected to the direct current external potential difference with a pair of wires sealed with silver paste onto the gold thin film of the samples. Figures 5.4 and 5.5 show the setup for both straight and elliptical samples respectively.

Direct current potential differences of 5, 10, 20, 40 and 400 V_{dc} are used in the experiments. Elliptical heat spreader (Elliptical D) with 1200 μm^2 cross sectional area and 2 mm pumping distance use alternating current (AC) voltage as a voltage source of the electro-osmotic flow. AC input voltage is beneficial in reducing bubble generation as the result of electrolysis. This will be explained in detail in Chapter 6.

The electro-osmotic force is employed to the samples and flow rates are determined to study the characteristics of electro-osmotic flow. The effects of electric field, zeta potential and cross sectional area on the velocity and flow rate are analysed.

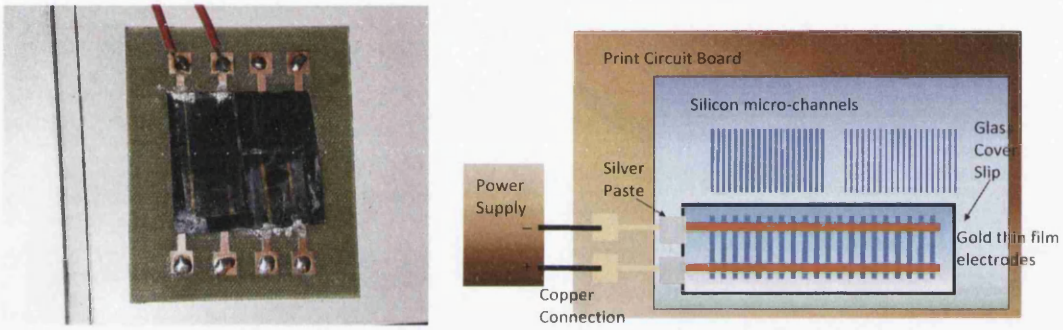

(a) (b)

Figure 5.4: Straight micro-channel structure. Experiment setup.

5.6 Straight Micro-channel - Flow Measurement Results

Silicon particles are chosen in the flow measurement. There have small zeta potential of -5 mV at pH 7. Therefore, it is assumed not much influence to the flow measurement.

Videos of the silicon particle movement in samples Straight A to Straight E have been recorded by a CCD digital camera in the velocimetry system as discussed in Section 5.3. The overlapped images of samples are shown in Figure 5.6. The displacements of the silicon particles are calculated using the Equations 5.3 to 5.5. The calculated velocity and flow rate in every sample are listed in Table 5.2.

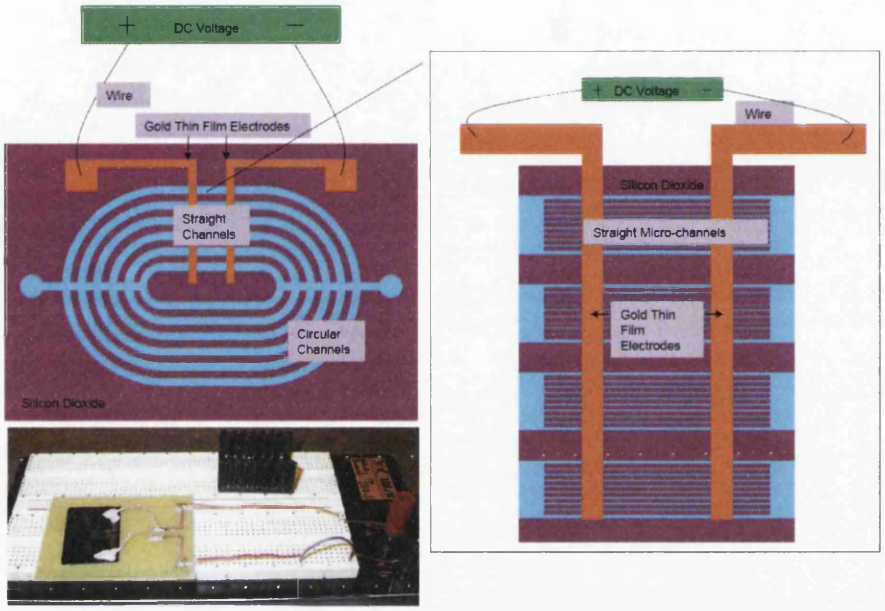

Figure 5.5: Elliptical heat spreader. Experiment setup.

5.6.1 Experimental Analysis

The mean deviation ($|D|$) and experiment error (E_r) are calculated and shown in Table 5.2. The mean deviation of experiment is less than 0.0084 mm/min and experiment error is less than 9.06 percent.

According to Equation 2.19 and Equation 5.9, the velocity of electrolyte will vary with respect to external potential difference, zeta potential and properties of electrolyte. Since DI water was used in all the experiments, the properties of electrolyte were assumed constant.

With a pumping distance of 10 mm, the electric fields applied on sample Straight B is 1 kV/m. The velocity obtained from sample Straight B is 0.898 mm/min. Increasing the electric field from 1 to 2 kV/m (Straight C) gives the velocity increase from 0.898 mm/min to 1.268 mm/min. A further increase in the external potential to 4 kV/m (Straight D) gives a velocity of 5.542 mm/min.

Zeta potentials of samples were calculated by using Equation 5.9 and are shown in Table 5.2. With silicon dioxide surface, the zeta potential is varying between 13.48 mV

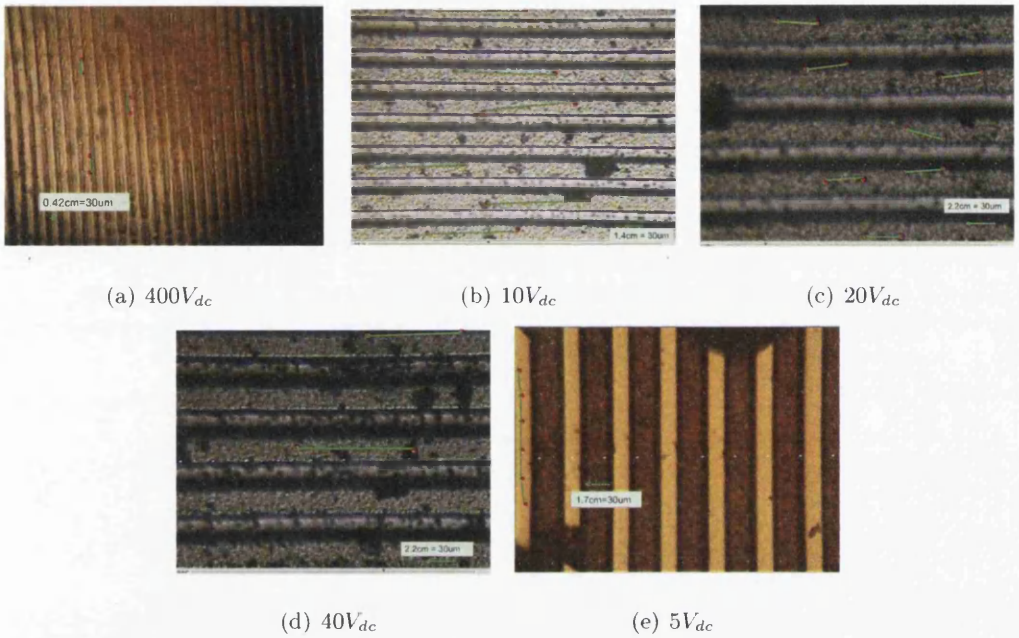

(a) $400V_{dc}$ (b) $10V_{dc}$ (c) $20V_{dc}$

(d) $40V_{dc}$ (e) $5V_{dc}$

Figure 5.6: Overlapped images of Straight A to Straight E samples.

to 43.66 mV (Straight B, C, D and E). However, the silicon surface (Straight A) gives a zeta potential less than 1 mV. The zeta potential of the surface affects the velocity of the electrolyte flow. In experiments, the sample Straight B has zeta potential of 13.48 mV. It gives velocity of 0.898 mm/min by subjecting the electrolyte to an electric field of 1 kV/m. However, Straight E gives a higher velocity of 2.065 mm/min at 1 kV/m. This is because Straight E develops a higher zeta potential than Straight B.

The flow rate is calculated by using Equation 5.1. The flow rate of a sample varies against change in electro-osmotic velocity and cross sectional area of a micro-channel. The sample Straight A has a cross sectional area of 15 μm^2. It gives a total flow rate of 0.0051 $\mu l/min$ for 152 micro-channels at a velocity of 2.221 mm/min and an electric field of 40 kV/m. High velocity is obtained in a narrow channel but it gives smaller flow rate. The narrow channel has higher surface to cross sectional area ratio. Thus the EO activity is pronounced for smaller channels [90].

Samples Straight B to E which have cross sectional area of 300 μm^2 give flow rates of 0.0410, 0.0578, 0.2527 and 0.0941 $\mu l/min$ respectively. These flow rates are obtained

Table 5.2: Straight channels experimental results.

Samples Surface	External Voltage (kV/m)	Velocity (mm/min)	Flow rate in 152 channels ($\mu l/min$)	Mean Deviation (mm/min)	Experiment Error (%)	Zeta Potential (mV)
Straight A - Si	40	2.221	0.0051	0.0033	8.79	1.19
Straight B - SiO_2	1	0.898	0.0410	0.0011	7.13	19.26
Straight C - SiO_2	2	1.268	0.0578	0.0010	4.61	13.48
Straight D - SiO_2	4	5.542	0.2527	0.0084	9.06	29.54
Straight E - SiO_2	1	2.065	0.0941	0.0024	6.97	43.66

from 152 straight micro-channels. In these cases, lower velocities are obtained in wider channels but the flow rates are higher than in the narrow channels.

The directions of particles which are shown in Figure 5.6 are not consistent. The variation of the particles' direction is mainly due to the bubble generation in the micro-channel.

5.7 Elliptical Heat Spreader - Flow Measurement Results

Electro-osmotic force is employed in elliptical heat spreader samples Elliptical A to C with applied direct current potential difference of 5, 50 and 400 V. The DI water with seeded particles is injected into the samples and the movement of particles is monitored by velocimetry system as discussed in Section 5.3. The overlapped images of the samples are shown in Figures 5.7 and 5.8. The velocities and flow rates of electrolyte in samples Elliptical A to C are shown in Table 5.3. The properties of the electrolyte are assumed constant.

Table 5.3: Elliptical channels experimental results

Samples Surface	External Voltage (kV/m)	Velocity (mm/min)	Flow rate in 152 channels ($\mu l/min$)	Mean Deviation (mm/min)	Experiment Error (%)	Zeta Potential (mV)
Elliptical A - Si	10	0.331	0.0008	0.0005	8.70	0.77
Elliptical B - Si	80	0.567	0.0013	0.0007	7.78	0.14
Elliptical C - SiO_2	2	1.112	0.2028	0.0018	9.64	12.20

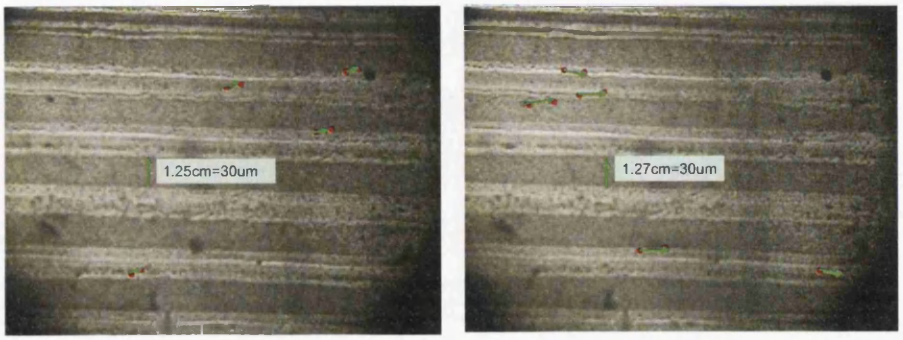

(a) (b)

Figure 5.7: Elliptical silicon channels subjected to (a)50V. (b)400V.

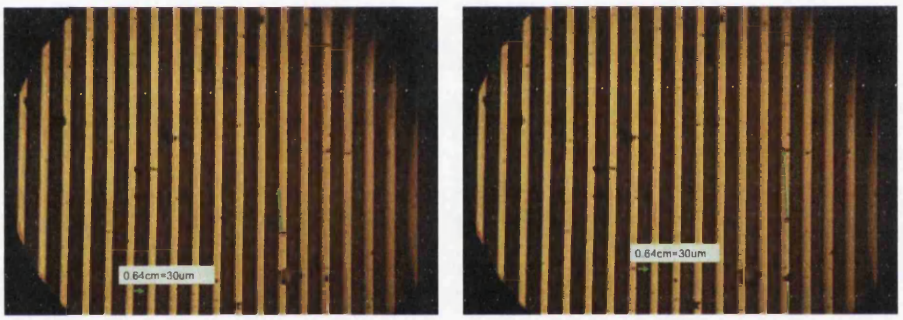

(a) (b)

Figure 5.8: Elliptical silicon dioxide channels subjected to 5V.

5.7.1 Experimental Analysis

As given in Table 5.3, the mean deviation of experiments is less than 0.0018 mm/min and experiment error is less than 9.64 percent.

The elliptical silicon heat spreader of Elliptical A and B have the same cross sectional area and surface material. A 10 kV/m electric field was employed across the heat spreader A and a velocity of 0.331 mm/min was obtained. With an increase in electric field to 80 kV/m, the velocity increased to 0.567 mm/min. Both silicon heat spreaders give small flow rates of 0.0008 and 0.0013 $\mu l/min$ for 152 channels with cross sectional area of 20 μm^2 per channel. The silicon heat spreader gives small zeta potential which is less than 1 mV.

The silicon dioxide heat spreader (Elliptical C) is capable to produce higher EO velocity and flow rate than both silicon heat spreaders (Elliptical A and B). This is because, silicon dioxide surface has higher zeta potential of 12.20 mV than the silicon. The EO pump in the heat spreader C has width, length and depth of 10 mm (152 straight micro-channels), 2 mm(pumping distance) and 30 μm respectively. The EO pump has size of 0.6 mm^3.

5.8 Summary

In this chapter, velocimetry system has been set up to measure the velocity of electrolyte in the EO heat spreader. Videos were taken via microscope on a seeded EO flow in the micro-channel samples. Then, the videos were frozen to obtain images. The particle displacements were then calculated from the images. The EO velocity can be obtained by dividing the particle displacements with the time interval between those images. Finally, the flow rate was calculated by multiplying EO velocity with cross sectional area of the micro-channel. The measurement error, deviation and the zeta potential were also calculated in the experiments.

The results show that the silicon micro-channels give small zeta potential when using DI water with a pH value of 7. Small zeta potential results in the silicon micro-channels giving smaller EO velocity and hence the flow rates. However, the micro-channels with silicon dioxide surface can generate good EO velocity. Besides, high electric field also contributed to higher electro-osmotic velocity. However, electric field has to be limited because it will generate bubbles and Joule heating. Therefore, AC voltage will be used as voltage source in the next chapter to reduce the bubbles generation. The shallow micro-channels could generate high velocity due to more surface to cross sectional area ratio. However, it generates lower flow rate compared to large cross sectional area.

Chapter 6

Bubble Formation

6.1 Introduction

As electric current flows through the electrolyte from electrodes, non-Faradaic and Faradaic processes occur at the electrode-electrolyte interface.

In the non-Faradaic process, no charge transfer reactions occur at the electrode-electrolyte interface. Charging double layer to its capacitance near the electrode is a non-faradaic process and does not cause any charge transfer. In DI water, non-Faradaic process occurs at small potential difference which is below 1.2 V [57, 58].

When the double layer is fully charged to its capacitance, Faradaic process starts transferring charges between the electrode and electrolyte. This reaction either supplies electrons (reduction) or sinks electrons (oxidation) which is known as Redox reaction. The Redox reaction in DI water may be defined as:

$$2H_2O(l) \rightarrow 2H_2(g) + O_2(g) \tag{6.1}$$

At cathode, electrons combine with hydrogen ions to produce hydrogen gas.

$$4H^+ + 4e^- \rightarrow 2H_2(g) \tag{6.2}$$

At anode, electrons are removed from oxygen to produce oxygen gas.

$$2O^{-2} - 4e^{-} \rightarrow O_2(g) \tag{6.3}$$

Redox reaction leads to formation of gases which yield some negative effects such as bubbles blocking micro-channels and the fluid drying out in a few seconds [91]. Thus, platinum can be used as electrode material due to its inert properties and its capability to catalyze the proton reaction [25, 56]. However, this method will increase the cost of manufacturing. Besides, thin platinum film needs to be deposited with high temperature evaporator and this results in complex manufacturing process. Therefore, in the heat spreader design, gold is used which is cheaper and it can be deposited with sputtering evaporator.

A drawback of using gold for material of electrodes in the heat spreader is that it will generate bubbles near the gold thin film. The bubble formation will also damage the thin film of gold electrodes. In some works, open reservoirs are used in the work to allow evacuation of the gases. However, this method is not applicable in micro applications. Therefore varying voltage source was selected as an alternative for micro-systems.

6.1.1 DC and AC drive

Faradaic process occurs when voltage exceeds 1.2 V. High continuous direct current (DC) will result in bubble formation. Thus pulsed alternating current (AC) voltage is employed here to stop the transfer of charges.

At positive cycle of AC pulsed voltage, the double layer is charging up. In a short charging period, the double layer does not have enough time to charge up to its capacitance. Thus, no transfer of charges can happen near the electrode-electrolyte interfaces. The charging period can be varied by changing the duty cycle value of the AC pulsed voltage. The duty cycle of pulsed voltage is illustrated in Figure 6.1 which is defined as a ratio of the duration of positive cycle of the AC pulsed voltage (t_{on}) to the total duration (t).

$$Duty\ Cycle = \frac{t_{on}}{t} \tag{6.4}$$

The total duration is the sum of both duration of positive (t_{on}) and negative (t_{off}) cycle.

$$t = t_{on} + t_{off} \tag{6.5}$$

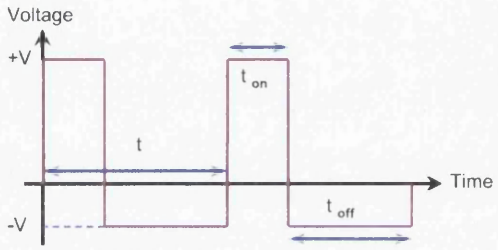

Figure 6.1: Duty cycle.

With long charging period, the double layer is charged to its capacitance resulting in the start of charge transfer reaction. Bubble generation starts with it. Therefore, small duty cycle is preferable and used in present study.

In positive cycle of AC pulsed voltage, the electro-osmotic flow occurs as the positive charges in the diffuse layer are attracted towards the negative electrode. As the AC pulse source flips the voltage to the negative cycle the electro-osmotic flow changes direction. To keep the same direction of the flow, only very small negative voltage is used. Thus, the reversed flow is very small and the resulting average flow is still in one direction only. Besides, with small negative voltage, only non-Faradaic reaction occurs. Therefore, no gas bubbles form in the negative cycle.

Pulsed AC voltage was also used by Selveganapathy et al and Multu et al. They applied a periodic, zero charge current to an electro-osmotic pump to reduce the bubbles [92, 93]. The electro-kinetic pump produced by Wu et. al. [85] used low AC voltage between 5 and 10 V_{rms} a frequency of 100 kHz for the application of bio-sensors.

6.2 Experimental Setup

The experimental setup with AC rectangular voltage pulse is illustrated in Figure 6.2. A function generator is used to generate voltage pulses to the electrodes E1 and E2 in the electro-osmotic sample as shown in Figure 6.3. Experiments were carried out to study

the influence of electrical conductivity of electrolyte, applied voltage, frequency and duty cycle on bubble formation. The observations on both electrodes E1 and E2 are recorded.

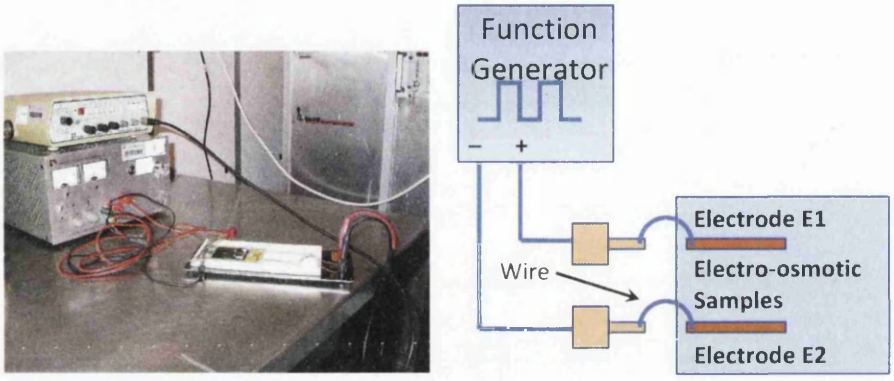

(a) (b)

Figure 6.2: Illustration of pulsed voltage experiment setup.

Figure 6.3: Stream of voltage pulses.

6.2.1 Electrical Conductivity of Electrolyte

In this section, two electrolyte with electrical conductivity of 289 and 88 $\mu S/cm$ are prepared. The electrode E1 (cathode) and E2 (anode) are connected to the positive and negative voltage source of electro-osmotic heat spreader respectively. A pulsed voltages of 10.4 V and -1.4 V and duty cycle of 72 percent is applied to a solution via electrode E1 and

Table 6.1: Electrical conductivity effect.

Elec conductivity ($\mu S/cm$)	Freq (Hz)	Duty Cycle (%)	$+V$	$-V$	Observation
88	92	72	10.4	-1.4	No Bubble
289	92	72	10.4	-1.4	Bubbles appear at electrode E1

E2. The bubble formation in the electro-osmotic heat spreader are observed and recorded in Table 6.1.

During the experiment, bubbles are observed near both the electrodes at electrolyte with electrical conductivity of 289 $\mu S/cm$. However, as the electrical conductivity reduced to 88 $\mu S/cm$, no bubble is noticed. These observations show that high electrical conductivity of electrolyte will result in bubble formation. The bubbles that appear near the electrode E1 (cathode) due to hydrogen gas generated are more than the oxygen which is generated near the anode.

6.2.2 Duty Cycle

Duty cycles between 30 to 95.15 percent are used in the present study. As seen in Table 6.2, at a duty cycle of 30 percent, there are no bubbles generated by the electrolysis process with pulsed voltage of 10.4 V and -1.4 V. However, when the duty cycle is increased to a value between 43.25 and 51 percent, bubbles can be seen near the electrode E1 (cathode). The duty cycle variation indicates that the maximum duty cycle that can avoid the bubble generation is below 30 percent. It should also be noted that by increasing the pulsed voltage to 13.4 V and -0.4 V, bubble generation also can be stopped with duty cycle of 30 percent.

The electrolysis reaction is reversed when the voltage turns to the negative. The bubbles are generated near the electrode E2 where the hydrogen ions accept the electrons from the electrolyte and forms hydrogen gas.

In fact, when the negative voltage is -10.4 V, the positive voltage in the pulse should reduce to 1.4 V with a duty cycle of 83 percent. This is because the t_{on} period has to be reduced to stop the electronation (accept ions) of hydrogen gas. In another case (Table 6.2), if the duty cycle is maintained below 20 percent, the bubbles still can be observed in

Table 6.2: Duty Cycle effect.

Elec conductivity ($\mu S/cm$)	Freq (Hz)	Duty Cycle (%)	$+V$	$-V$	Observation
289	10	30	10.4	-1.4	No Bubble
289	10	43.25	10.4	-1.4	Bubbles appear slowly at electrode E1
289	10	51	10.4	-1.4	Bubbles appear at electrode E1
289	10	30	13.4	-0.4	No Bubble
289	10	95.15	13.4	-0.4	Bubbles appear slowly at electrode E1
289	0.53	83	1.4	-10.4	No Bubble
289	0.65	20	0.6	-10.4	Bubbles appear at electrode E2

the electrode E2.

6.2.3 Frequency

In this section, frequencies of pulsed voltage from 4 Hz to 1000 Hz are used to supply an AC voltage stream of 10.4 and -1.4 V to the electro-osmotic heat spreader. Table 6.3 shows that there are no bubble is observed in these range of frequency.

Table 6.3: Frequency effect.

Elec conductivity ($\mu S/cm$)	Freq (Hz)	Duty Cycle (%)	$+V$	$-V$	Observation
289	4	30	10.4	-1.4	No Bubble
289	40	30	10.4	-1.4	No Bubble
289	135	30	10.4	-1.4	No Bubble
289	1000	30	10.4	-1.4	No Bubble

6.2.4 Voltage

Applied voltage has a very strong influence on bubble generation. Note that, bubbles were generated near the gold electrodes, when a DC voltage of 1.2 V or above was applied. Therefore, pulsed voltage is used.

Referring to Table 6.4, as the voltages of t_{on} and t_{off} are adjusted to positive values of 13.4 and 1.4 V, the bubbles appear at the electrode E1 (cathode). This shows that a continuous positive pulsed voltage will not reduce the bubble generation. Thus, the

Table 6.4: Voltage effect.

Elec conductivity ($\mu S/cm$)	Freq (Hz)	Duty Cycle (%)	$+V$	$-V$	Observation
289	10	30	13.4	1.4	Bubbles appear slowly at electrode E1
289	0.65	20	13.4	-0.4	No Bubbles
289	10	30	10.4	-1.4	No Bubbles
289	10	30	10.4	-5.6	Bubbles appear slowly at electrode E1
289	10	30	13.4	-5.6	Bubbles appear slowly at electrode E1
289	0.53	83	1.4	-10.4	No Bubbles
289	10	30	1.8	-10.4	Bubbles appear at electrode E2
289	10	30	6.8	-10.4	Bubbles appear slowly at electrode E2

voltage of t_{off} is reduced to -0.4, the bubble formation is ceased. This phenomena is also applicable to the experiment with pulsed 10.4 V and -1.4 V. However, as decreasing of the negative voltage to -5.6 V, the bubbles start appear at electrode E1.

In the case of high negative voltage of -10.4 V, the bubbles appear at electrode E2 when t_{on} is above 1.4 V. All experiments show that asymmetrical voltage pulse cycle can stop electrolysis.

6.3 Pulsed Signal Flow Measurement

During the above experiments, note that bubbles start forming near the electrodes when positive pulsed voltage is higher than 10.4 V and negative pulsed voltage is lower than -1.4 V. To reduce bubble formation, low reversed voltage needs to be applied. A pulse like voltage input of 10.4 V and -1.4 V as shown in Figure 6.3 is used in the flow experiment here. This resulted in successful elimination of bubbles. Also, a duty cycle of less than 30 percent helped in reducing the bubble formation near the electrodes. Frequency with the range of 4 to 1000 Hz has no effect on the bubbles generation. However, in the present study, low frequency of 10 Hz is used here to generate the flow in the heat spreader.

The AC pulsed voltage is applied across the micro-channels of elliptical structure of Elliptical D to measure the electro-osmotic flow rate. The particles introduced into the

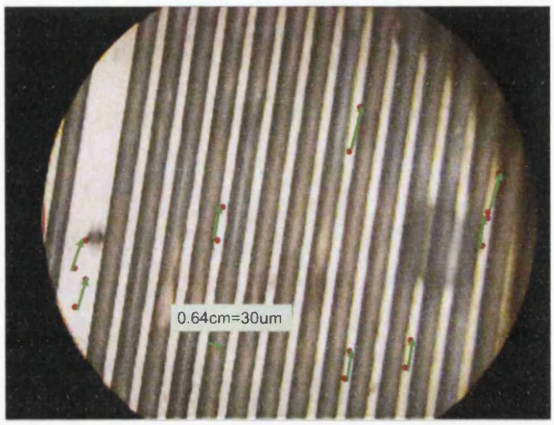

Figure 6.4: Heat Spreader structure with silicon dioxide surface with pulsed signal.

fluid are tracked using the velocimetry system as shown in Section 5.3. Overlapped image of Elliptical D is shown in Figure 6.4. The velocity produced by pulsed voltage is about 1.3 mm/min and the flow rate in the elliptical heat spreader is 0.237 $\mu l/min$ (Table 6.5). The experimental error and mean deviation are 9.15 percent and 0.002 mm/min respectively.

Table 6.5: Elliptical channels with AC voltage experimental results.

Samples Surface	External Voltage (kV/m)	Velocity (mm/min)	Flow rate in 152 channels ($\mu l/min$)	Mean Deviation (mm/min)	Experiment Error (%)
Elliptical D - SiO_2	AC Voltage	1.300	0.2370	0.0020	9.15

6.4 Summary

The high potential difference which was applied to the micro-channels induces electrolysis which causes the redox reaction near the electrodes. This is followed by bubbles generation and consequent damage to the thin film electrodes. In this chapter, asymmetrical AC voltage is used to reduce the generation of bubbles. The experiments show that at positive pulsed voltage higher than 10.4 V and a negative pulsed voltage lower than -1.4 V, a duty cycle of less than 30 percent and a frequency of 10 Hz helped reducing the bubble

formation near the electrodes. The heat spreader with AC voltage source produces EO velocity of 1.3 mm/min and the flow rate of 0.237 $\mu l/min$.

Chapter 7

Temperature Measurements

7.1 Introduction

While operating, the temperature of microprocessor will rise until the system reaches equilibrium with the surroundings. For reliable operation, the equilibrium temperature must be sufficiently low.

In this chapter, experiments were carried out to prove that with the aid of electro-osmotic heat spreader, the microprocessor is able reach an equilibrium temperature faster than without it. Besides, electro-osmotic heat spreader is able to reduce the temperature of the microprocessor.

7.2 Equilibrium Temperature Measurement

The equilibrium temperature measurement setup which is shown in Figure 7.1(a) is used to observe the heat transfer rate from heat source to the ambient with and without the aid of electro-osmotic pump. A heat spreader is placed on the top of a resistor plate of 25 Ω which is used as a heat source which is analogous to a microprocessor. Both heat source and heat spreader are connected to a power supply. A thermal camera is used to record a sequence of thermal images as Figure 7.1(b) of heat source and heat spreader in the experiments. These thermal images are used to subtract a reference image pixel by pixel with the image subtraction function in the thermal camera. This method is ideal

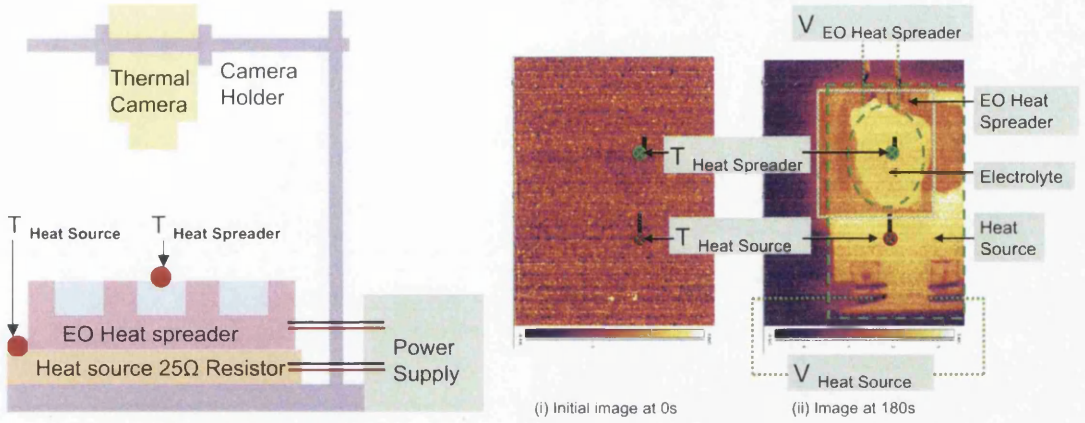

(a) (b)

Figure 7.1: (a) Equilibrium temperature measurement setup. (b) Thermal images from thermal camera.

for monitoring very small temperature changes in a recorded sequence. The temperature difference is obtained from image subtraction function which is expressed as:

$$T_1 = T_{Heat\ Source} - T_{reference} \tag{7.1}$$

$$T_2 = T_{Heat\ Spreader} - T_{reference} \tag{7.2}$$

where T_1 and T_2 are the temperature difference of heat source and heat spreader respectively. The reference image here is referred to the initial image. The temperature reference, $T_{reference}$ of both heat source and heat spreader in the initial image is equivalent to room temperature of 25 ^oC. Thus, the T_1 and T_2 give values of 0 ^oC at initial image (Figure 7.1(b)(i)). As the heat source is powered, the temperature of both heat source ($T_{Heat\ Source}$) and heat spreader ($T_{Heat\ Spreader}$) are increased. T_1 and T_2 are obtained from Equation 7.1 and plotted in a graph which is shown in Figure 7.2.

In the first experiment, a resistor plate is connected to a voltage of 3.3 V to generate a power of 0.43 W. The electro-osmotic pump is turned off, therefore, no circulation of electrolyte is allowed. The T_1 and T_2 are plotted on a real time graph and are shown in Figure 7.2(a). As seen in that figure, without the water circulation, the heat source and electrolyte struggle to reach any sensible equilibrium within the observed time period.

In the second experiment, the electro-osmotic pump in sample Elliptical C in Chapter 5 is turned on to allow the electrolyte to circulate. With the aid of electro-osmotic pump, heat source and electrolyte in the pump reach the equilibrium temperature at the time of 2 minutes (refer to Figure 7.2)(b). The Figure 7.2(b) clearly demonstrates that the heat spreader is effective.

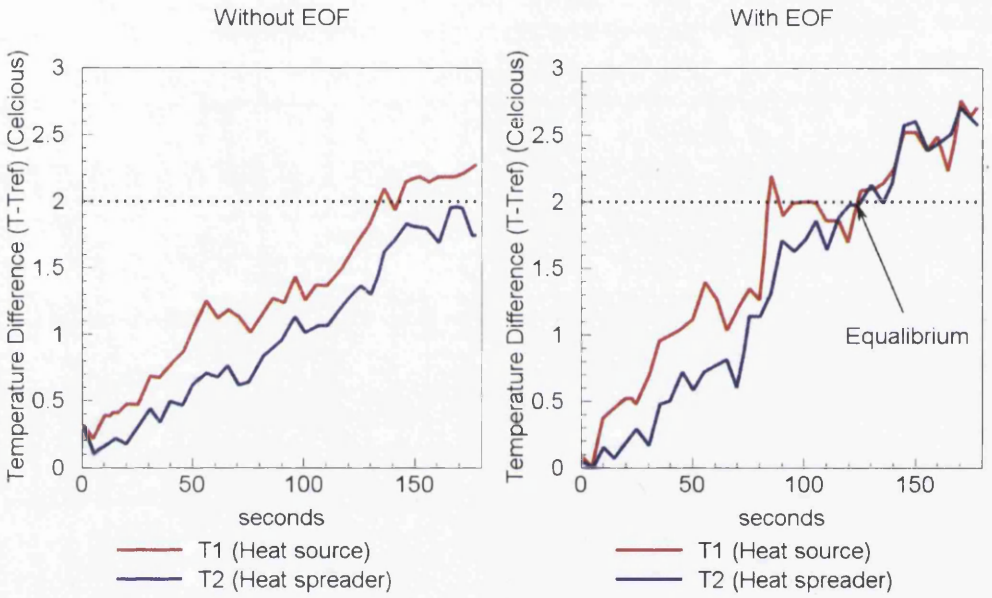

Figure 7.2: The heat source (a)without the electrolyte circulation. (b)with the electrolyte circulation.

7.3 Temperature Measurement Setup

Experiments are carried out to compare the heat source temperature at different conditions as: with and without electro-osmotic flow in the heat spreader.

In the first case, heat source with power of 0.9 W, 1.8 W, 3.7 W, 5.3 W are used. The temperatures of the heat source are measured with thermocouple at steady state. The average temperatures of the heat source are monitored and recorded in Figure 7.4 which are 40 ^oC, 46 ^oC, 62 ^oC and 74 ^oC respectively for the mentioned power. The temperature of heat source is increased as the power that is applied to the heat source is increased.

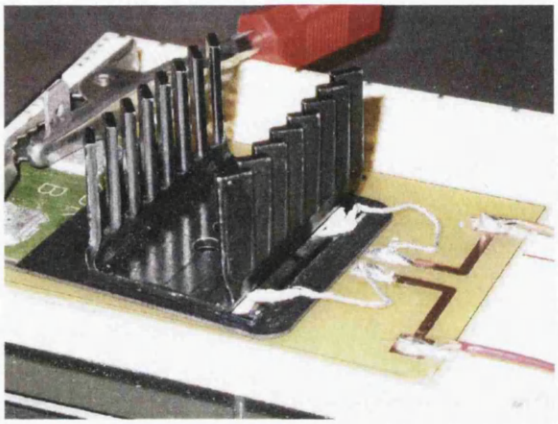

Figure 7.3: Temperature setup.

In the second case, a heat sink and an electro-osmotic heat spreader are attached to a heat source as shown in Figure 7.3. The electro-osmotic pump is switched off and no circulation of electrolyte is allowed. The objective of this experiment is to study the value of temperature that will be reduced by the aid of heat sink as a cooling system. The temperatures of heat source are reduced to 35 ^oC, 42 ^oC, 52 ^oC and 60 ^oC respectively. The attachment with the heat sink is able to increase heat convection from the heat source to the ambient.

In the third case, the electro-osmotic pump in the heat spreader is now turned on to allow electrolyte circulation. The temperature of heat source is reduced further to 34 ^oC, 39 ^oC, 49 ^oC and 56 ^oC. These show that with the embedded electro-osmotic flow in the heat spreader under the heat sink, the temperature of heat source is reduced by about 4 ^oC at 5.3 W. By combining the electro-osmotic flow in the heat spreader and a heat sink, the temperature of heat source can be reduced by as much as 18 ^oC.

7.4 Summary

Comparisons between the cooling system with and without EOF in the heat spreader are made. The experiments show that the electrolyte circulation which is induced by EO forces can accelerate equilibrium.

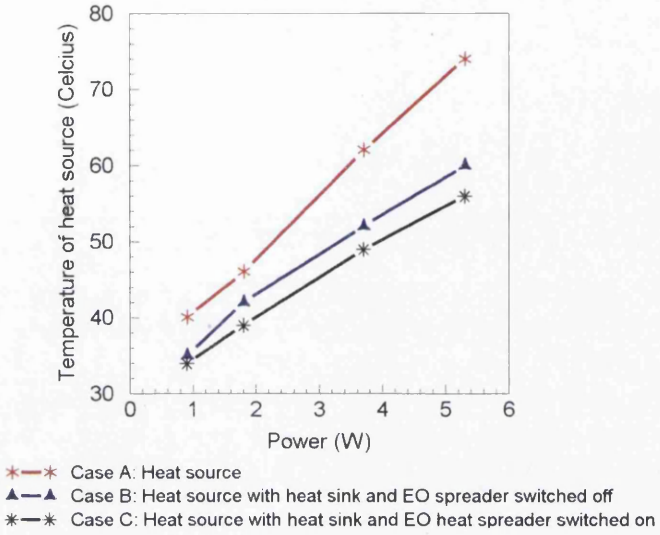

Power(W) Temperature of heat source(^oC)

	Case A	Case B	Case C
0.9	40	35	34
1.8	46	42	39
3.7	62	52	49
5.3	74	60	56

Figure 7.4: Temperature of the heat source with different setup configurations.

In addition, in Section 7.3, forcing the electrolyte circulation in the heat spreader and heat sink (Case C), the temperature of the heat source can be reduced by about 4 ^oC at 5.3 W compared to the configuration without electrolyte circulation. It is also shown that this configuration can reduce the temperature of heat source by as much as 18 ^oC.

Chapter 8

Non-Dimensional Governing Equations

8.1 Introduction

Non dimensional parameters identified in the past are not independent of each other [94]. Some studies use different scales for EOF potentials [36] and make the interpretation of results difficult. Thus a consistent non dimensional scale introduced by Nithiarasu et al [66] is used here. This scaling is better and easier way to analyse electro-osmotic flows and heat transfer model. The initial and boundary conditions of the electro-osmotic flow model and conjugate heat transfer model will be discussed in the latter part of this chapter.

8.2 Non Dimensional Form of Electric Field Equations

In the previous studies, Reynold number is identified as one of the non dimensional numbers. This form of scaling is suitable for the conventional pumping systems where actual flow velocities are known. However, this is not applicable to electro-osmotic flow system. In the electro-osmotic phenomena, the flow only occurs after employing an external electric force. Therefore, calculating a Reynolds number a priori is not possible. Thus the scales should be selected in such a way as to avoid introducing Reynolds number into the non-dimensional form. Consistent scale for both the external potential and elec-

trostatic potential should be used. The following scales are selected to non-dimensionalise the governing equations

$$\phi^* = \frac{ze\phi}{k_B T_\infty}; \psi^* = \frac{ze\psi}{k_B T_\infty}; x^* = \frac{x}{L_\infty}; t^* = \frac{t\alpha_\infty}{L_\infty^2};$$
$$L_\infty = W; \epsilon^* = \frac{\epsilon}{\epsilon_\infty}; \sigma^* = \frac{\sigma}{\sigma_\infty}; T^* = \frac{T - T_\infty}{T_\infty} \tag{8.1}$$

where L_∞ is width of the channel. Using the above scales, the non dimensional form of Equations 2.4 and 2.12 take the following forms:

$$\sigma^* \left(\frac{\partial^2 \phi^*}{\partial x_i^{*2}} \right) = 0 \tag{8.2}$$

and

$$\epsilon^* \left(\frac{\partial^2 \psi^*}{\partial x_i^{*2}} \right) = (\kappa a)^2 \sinh \left(\frac{\psi^*}{T^* + 1} \right) \tag{8.3}$$

$T^* = 0$ if no temperature is involved in the electro-osmotic flow. Here, σ^* and ϵ^* is assumed constant and $\kappa a = W \times \kappa$ where W is the width of the channel and κ is Debye-Huckel Parameter, given as

$$\kappa = \sqrt{\frac{2 n_0 z^2 e^2}{\epsilon_\infty \epsilon_0 k_B T_\infty}} \tag{8.4}$$

$1/\kappa$ is the electric double layer (EDL) thickness or Debye length. EDL thickness is the distance at which the potential ψ is reduced to the value at the solid surface. At high ionic concentration, n_0, the EDL thickness is small and usually about a few nanometers. At small EDL thickness, effects of electric double layer on the flow in micro-channels is negligible. Note that small EDL thickness gives high κa value.

On other hand, low ionic concentration has higher EDL thickness and resulting EDL overlap can produce high friction coefficient over the channel [95]. EDL overlapping often occurs in nano-channels. The high friction coefficient will result in lower flow rates. At thick EDL, κa value is small.

With the small zeta potential, ζ, the Debye Huckel approximation is assumed. Linear Poisson-Boltzmann equation in non dimensional form may be written as:

$$\epsilon^* \frac{\partial^2 \psi^*}{\partial x_i^{*2}} = (\kappa a)^2 \left(\frac{\psi^*}{T^* + 1} \right) \tag{8.5}$$

In our study, Equation 8.3 is used. This is because, solving Poisson Boltzmann equation without adding any approximation leads to more accurate simulations.

8.3 Non-dimensional form of the Navier Stokes Equations

Using the non dimensional scales listed below, the governing Equations of 2.18, 2.21 and 2.22 can be transformed into non-dimensional form.

$$u^* = \frac{uL_\infty}{\alpha_\infty}; \rho^* = \frac{\rho}{\rho_\infty}; x^* = \frac{x}{L_\infty}; t^* = \frac{t\alpha_\infty}{L_\infty^2}; P^* = \frac{PL_\infty^2}{\rho_\infty \alpha_\infty^2}; \phi^* = \frac{ze\phi}{k_B T_\infty};$$
$$\psi^* = \frac{ze\psi}{k_B T_\infty}; \beta^* = \frac{\beta L_\infty}{\alpha_\infty}; T^* = \frac{T - T_\infty}{T_\infty}; \alpha_\infty = \frac{k_\infty}{(\rho c_p)_\infty} \tag{8.6}$$

Continuity equation:

$$\frac{1}{\beta^{*2}} \frac{\partial P^*}{\partial t^*} + \rho^* \frac{\partial u_i^*}{\partial x_i^*} = 0 \tag{8.7}$$

The speed of sound, c is replaced by an artificial compressibility (AC) parameter, β which will be discussed further in Section 9.4.

Modified momentum equation:

$$\rho^* \left(\frac{\partial u_i^*}{\partial t^*} + u_j^* \frac{\partial u_i^*}{\partial x_i^*} \right) = -\frac{\partial P^*}{\partial x_i^*} + Pr \frac{\partial \tau_{ij}^*}{\partial x_i^*} + J \sinh \left(\frac{\psi^*}{T^* + 1} \right) \frac{\partial \phi^*}{\partial x_i^*} \tag{8.8}$$

where ρ^*=1 for incompressible flows and

$$Pr = \frac{\mu}{\rho_\infty \alpha_\infty}; J = \frac{2n_0 k_B T_\infty L_\infty^2}{\alpha_\infty^2 \rho_\infty}; \tau_{ij}^* = \left(\frac{\partial u_i^*}{\partial x_j^*} + \frac{\partial u_j^*}{\partial x_i^*} \right) \tag{8.9}$$

Prandtl number, Pr is the dimensionless number approximating the ratio of the momentum diffusivity to the thermal diffusivity. It contains no length scale unlike Reynolds number. It is only dependent on the electrolyte used. This can be calculated prior to the

experiment and simulation. In the present calculations, Prandtl number of electrolyte in room temperature is used.

Parameter J is defined by properties of electrolyte such as bulk ionic concentration, density and thermal diffusivity. The increase of ionic concentration of electrolyte will increase the parameter J and subsequently increase the velocity of the electrolyte.

Energy equation:

$$\left(\frac{\partial T^*}{\partial t^*} + u_j^* \frac{\partial T^*}{\partial x_j^*}\right) = \alpha^* \frac{\partial^2 T^*}{\partial x_j^{*2}} \tag{8.10}$$

where

$$\alpha^* = \frac{\alpha}{\alpha_\infty} \tag{8.11}$$

$\alpha_\infty = \alpha_{fluid}$, is used. In this thesis, Joule heating is ignored because the voltage that was used in the experiment and simulation is small.

Convective and conductive terms are available in the Equation 8.10. This equation valid for channels filled with electrolyte. However, for solid part of the heat spreader this can be reduced to

$$\frac{\partial T^*}{\partial t^*} = \alpha^* \frac{\partial^2 T^*}{\partial x_j^{*2}} \tag{8.12}$$

In summary, the Prandtl number, Pr and parameters, ka and J are defined using properties of electrolytes and geometry that are known a priori for electrolyte and geometry used. Furthermore, these parameters are independent of each other. This form of non dimensional scale is easier and consistent compared to other scales employed.

8.4 Initial and Boundary Conditions

8.4.1 Electro-osmotic Flow Model

A layout of micro-channel as shown in Figure 8.1 is used to describe the boundary location of the electro-osmotic flow phenomena. It is applied to a three dimensional micro-

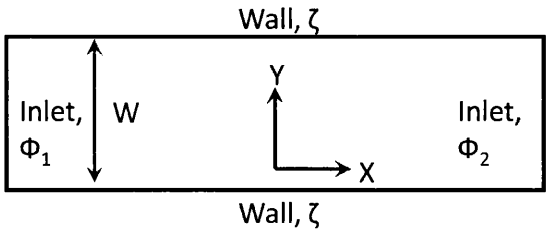

Figure 8.1: Boundary condition of EOF channel.

channel which will be demonstrated in the latter chapter. The boundary conditions for the micro-channel are imposed as :

On the channel walls or any solid boundary:

$$\psi = \zeta; \frac{\partial \phi}{\partial y} = 0; u_1 = 0 \tag{8.13}$$

where ζ is zeta potential. Non-dimensionalised zeta potential is applied near the wall and the external potential gradient in y direction is equal to zero. The velocity is initialized with zero value.

At the inlet, where x = 0

$$\frac{\partial \psi}{\partial x} = 0; \phi = \phi_1; \frac{\partial u_i}{\partial x} = 0 \tag{8.14}$$

At the exit, where x = L

$$\frac{\partial \psi}{\partial x} = 0; \phi = \phi_2; \frac{\partial u_i}{\partial x} = 0 \tag{8.15}$$

The gradient of the velocity in x direction is equal to zero due to electro-osmotic phenomena. ϕ_1 and ϕ_2 are applied external potentials.

8.4.2 Conjugate Heat Transfer Model

A layout of electro-osmotic heat spreader as shown in Figure 8.2 is used to describe the boundary location of the conjugate heat transfer model.

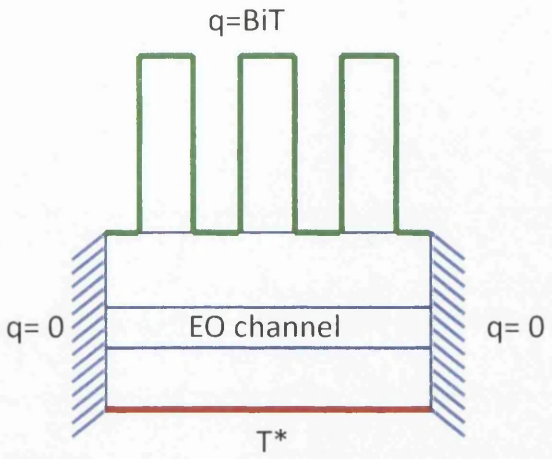

Figure 8.2: Boundary condition of conjugate heat transfer model.

A prescribed temperature is given to the heat source surface. It can be calculated with Equation 8.16.

$$T^* = \frac{T - T_\infty}{T_\infty} \tag{8.16}$$

where T_∞ is reference temperature. Room temperature of 298 K is used as reference temperature. In uniform heat source case, the prescribed temperature is constant. However, in non uniform heat source, the prescribed temperature is spatially varied.

Heat flux is expressed in terms of temperature gradient along the estimated normal of the fins surface.

$$q = k\frac{\partial T}{\partial n} = h(T - T_\infty) \tag{8.17}$$

where h is convective heat transfer coefficient, k is thermal conductivity and n is the normal direction. If the condition is no heat transfer or thermally insulated, the heat flux, q is equal to 0.

Convective heat transfer between the fins and the ambient at a constant heat flux is assumed. The non dimensional form of the Equation 8.17 is written for convective conditions as

$$\frac{\partial T}{\partial n} = BiT \tag{8.18}$$

where Bi is the Biot number and is given by:

$$Bi = \frac{hL_\infty}{k_\infty} \tag{8.19}$$

where L is the characteristic length which is equal to the width of channel.

Biot number is a dimensionless number which is used to describe the heat transfer resistance inside and at the surface of a body. If Biot number is low, heat conduction inside the solid is much faster than the heat convection away from its surface.

The rest of the surfaces are assumed adiabatic. No heat flux is involved in those surfaces.

8.5 Summary

In this chapter, a new non dimensional scale was used in non dimensionalisation of the electro-osmotic governing equations. The selected scale avoids introducing Reynold number into the non-dimensional form. This is because calculation of Reynold number a priori is not possible in electro-osmotic flow. Non dimensional parameters κa, Prandlt number, J and α will be further discussed in the next chapter. Both electro-osmotic and conjugate heat transfer boundary conditions are employed into the equations to investigate the influence of external potential, internal potential, velocity and temperature distribution.

Chapter 9

Temporal and Spatial Discretisation and Benchmarking

9.1 Introduction

The methods employed to discretise the governing electro-osmotic flow equations are presented here. The chapter begins by describing the method of solution for Laplace and Poisson-Boltzmann equations. Discretization of the Navier Stokes equations along with the added source term is discussed in Section 9.3. The method employed to discretise the governing equations is called the CBS algorithm. This incorporates both the temporal discretisation and split to introduce pressure stability. This chapter also discusses the local time stepping procedure and element size calculation used in the algorithm.

The validation of two dimensional algorithm will be discussed in Section 9.7 to ensure the accuracy of the numerical model. The velocity and internal potential distribution results were compared with the experimental data and analytical analysis from other works [29, 34, 4, 96, 97]. The effects of κa, zeta potential, external electric field, Prandlt number and parameter J on the fluid flow were investigated in the latter part of the chapter. Finally, three dimensional algorithm is presented and compared with two dimensional algorithm.

9.2 Discretization of Electric Field

The electric fields of electro-osmotic effect are solved separately from the Navier Stokes equations. The converged solution is then added as the source term to the momentum equation. This method is also used by Hu et al [29], Bianchi et al [35] and Patankar and Hu [34].

Global time stepping procedure is used in solving electric field equation where the time stepping is fixed and does not depend on element size. However, Navier Stokes equations use the local time stepping which will be discussed later in this chapter.

A pseudo time term is added to the electric field equations and solved explicitly. As steady state solution is reached, the pseudo time term is negligible. This similar method was used by Klaij et al [98]. The electric field equations with pseudo time term are written below.

Laplace equation:

$$\frac{\partial \phi}{\partial t} + \frac{\partial^2 \phi}{\partial x_i^2} = 0 \tag{9.1}$$

Poisson Boltzmann equation:

$$\frac{\partial \psi}{\partial t} + \frac{\partial^2 \psi}{\partial x_i^2} = (\kappa a)^2 \sinh \psi \tag{9.2}$$

The above equations are temporally discretised using a finite difference approach. Thus, their semi-discrete forms are shown below

Laplace equation:

$$\frac{\phi^{n+1} - \phi^n}{\Delta t} = \left(-\frac{\partial^2 \phi}{\partial x_i^2} \right)^n \tag{9.3}$$

Poisson Boltzmann equation:

$$\frac{\psi^{n+1} - \psi^n}{\Delta t} = \left(-\frac{\partial^2 \psi}{\partial x_i^2} + (\kappa a)^2 \sinh \psi \right)^n \tag{9.4}$$

The Galerkin finite element method is used for spatial discretisation. It is a good choice for complex domains. The solution to the Poisson-Boltzmann equation and gradient

of solution to the Laplace equation are then added as source terms in the momentum equation.

9.3 Characteristic based Split (CBS) Method

The characteristic based split (CBS) algorithm has been developed by Zienkiewicz and Codina [38] which splits the Navier Stokes equations to remove the pressure term. Then, the equations are solved by the Characteristic Galerkin procedure.

The momentum equation without the pressure term is similar to the convection diffusion equation and can easily be discretised in time by the Characteristic Galerkin procedure which will be discussed in the next section.

The main steps of CBS algorithm are:

1. Solve the momentum equation for intermediate velocity field
2. Calculate the pressure
3. Correct the momentum
4. If temperature is involved, solve for temperature

The CBS algorithm is also applicable to temporal discretisation of the energy equation. The CBS algorithm removes the instability which is caused by the convection term appearing in the energy equation. The Navier-Stokes equations are spatially discretised using the Galerkin finite element procedure. They are weighted by the shape functions and then integrated over the domain [39, 40, 99, 100].

9.3.1 Temporal Discretization

To avoid instability created by the pressure term, the momentum Equation 2.19 is split into two parts. Introducing,

$$\frac{u_i^{n+1} - u_i^n}{\Delta t} = \left[\frac{u_i^{\dagger} - u_i^n}{\Delta t}\right] + \left[\frac{u_i^{n+1} - u_i^{\dagger}}{\Delta t}\right] \tag{9.5}$$

$$\frac{\Delta U^{\dagger}}{\Delta t} = \frac{u_i^{\dagger} - u_i^n}{\Delta t} = -u_j \frac{\partial u_i}{\partial x_i} + Pr \frac{\partial \tau_{ij}}{\partial x_i} + J \sinh\psi \frac{\partial \phi}{\partial x_i} \tag{9.6}$$

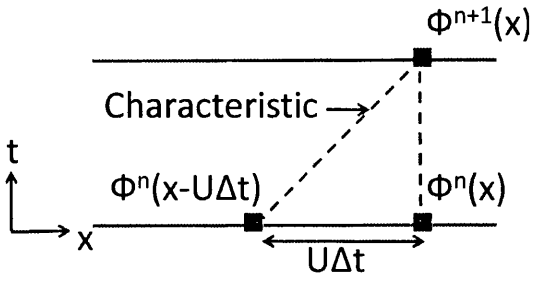

Figure 9.1: Characteristic galerkin procedure

and

$$\frac{\Delta U^{\dagger\dagger}}{\Delta t} = \frac{u_i^{n+1} - u_i^{\dagger}}{\Delta t} = -\frac{\partial P}{\partial x_i} \tag{9.7}$$

In step 1, an intermediate velocity without the pressure term is calculated. It is similar to convective diffusion problem (Equation 9.8). The convection diffusion problems also may give rise to physical oscillations of the numerical solution. Several ways have been developed to avoid oscillation from the which is commonly referred as stabilization technique, including Petrov Galerkin method and Galerkin Least Squares method. One drawback of these techniques is their efficiency relies on the selection value of algorithmic parameter which have to be tuned on test case [38]. The Characteristic Galerkin method is a good alternative stabilization technique because it is parameter free. The stabilizing terms are introduced through Taylor expansion of solution along the Characteristic curves. A convection diffusion equation in one dimension may be written as:

$$\frac{\partial \phi}{\partial t} + u\frac{\partial \phi}{\partial x} - \frac{\partial}{\partial x}\left(k\frac{\partial \phi}{\partial x}\right) + Q = 0 \tag{9.8}$$

assuming ϕ is travelling along the characteristic as shown in Figure 9.1, $\delta = \overline{U}\Delta t$ which is shown in Figure 9.1 is the distance travelled by the wave in x direction. Once the mesh position is updated, the convective term disappears and the remaining problem is just the simple diffusion which is written as:

$$\frac{\partial \phi}{\partial t}(x'(t), t) = \frac{\partial}{\partial x'}\left(k\frac{\partial \phi}{\partial x'}\right) - Q(x') \tag{9.9}$$

The temporal discretization of the above equation along the characteristic as shown in Figure 9.1 gives

$$\begin{aligned}\frac{\phi^{n+1}-\phi^{n}|_{(x-\delta)}}{\Delta t} &= \theta\left[\frac{\partial}{\partial x}\left(k\frac{\partial\phi}{\partial x}\right)-Q\right]^{n+1} \\ &+(1-\theta)\left[\frac{\partial}{\partial x}\left(k\frac{\partial\phi}{\partial x}\right)-Q\right]^{n}|_{(x-\delta)}\end{aligned} \tag{9.10}$$

where $\theta = 0.5$ for semi-implicit scheme.

$$\frac{\phi^{n+1}-\phi^{n}|_{(x-\delta)}}{\Delta t} = \frac{1}{2}\left[\frac{\partial}{\partial x}\left(k\frac{\partial\phi}{\partial x}\right)-Q\right]^{n+1}+\frac{1}{2}\left[\frac{\partial}{\partial x}\left(k\frac{\partial\phi}{\partial x}\right)-Q\right]^{n}|_{(x-\delta)} \tag{9.11}$$

Using Taylor expansion (refer to Appendix D.2)

$$\begin{aligned}\phi^{n}|_{(x-\delta)} &= \phi^{n}-\delta\tfrac{\partial\phi^{n}}{\partial x}+\tfrac{\delta^{2}}{2}\tfrac{\partial^{2}\phi^{n}}{\partial x^{2}}+O(\Delta t^{3}) \\ \tfrac{1}{2}\tfrac{\partial}{\partial x}\left(k\tfrac{\partial\phi}{\partial x}\right)|_{(x-\delta)} &= \tfrac{1}{2}\tfrac{\partial}{\partial x}\left(k\tfrac{\partial\phi}{\partial x}\right)^{n}-\tfrac{\delta}{2}\tfrac{\partial}{\partial x}\left[\tfrac{\partial}{\partial x}\left(k\tfrac{\partial\phi}{\partial x}\right)^{n}\right]+O(\Delta t^{2}) \\ \tfrac{1}{2}Q|_{(x-\delta)} &= \tfrac{1}{2}Q^{n}-\tfrac{\delta}{2}\tfrac{\partial Q^{n}}{\partial x}+\tfrac{\delta^{2}}{4}\tfrac{\partial^{2}Q^{n}}{\partial x^{2}}+O(\Delta t^{3})\end{aligned} \tag{9.12}$$

The convective term is now recovered with the Taylor expansion of Equation 9.12 and replacing δ with $U\Delta t$. Higher order terms are neglected.

$$\begin{aligned}\phi^{n+1}-\phi^{n} &= \Delta t\left[-U^{n}\frac{\partial\phi}{\partial x}^{n}+\frac{1}{2}\frac{\partial}{\partial x}\left(k\frac{\partial\phi}{\partial x}\right)^{n+1}-\frac{1}{2}Q^{n+1}+\frac{1}{2}\frac{\partial}{\partial x}\left(k\frac{\partial\phi}{\partial x}\right)^{n}-\frac{1}{2}Q^{n}\right] \\ &+\frac{\Delta t^{2}}{2}U^{n}\frac{\partial}{\partial x}\left[U^{n}\frac{\partial\phi}{\partial x}-\frac{\partial}{\partial x}\left(k\frac{\partial\phi}{\partial x}\right)+Q\right]^{n}\end{aligned} \tag{9.13}$$

The Equation 9.13 is reduced as:

$$\begin{aligned}\phi^{n+1}-\phi^{n} &= -\Delta t\left[U^{n}\frac{\partial\phi}{\partial x}^{n}-\frac{\partial}{\partial x}\left(k\frac{\partial\phi}{\partial x}\right)^{n+\frac{1}{2}}+Q^{n+\frac{1}{2}}\right] \\ &-\frac{\Delta t^{2}}{2}U^{n}\frac{\partial}{\partial x}\left[-U^{n}\frac{\partial\phi}{\partial x}+\frac{\partial}{\partial x}\left(k\frac{\partial\phi}{\partial x}\right)-Q\right]^{n}\end{aligned} \tag{9.14}$$

where

$$\begin{aligned}\frac{\partial}{\partial x}\left(k\frac{\partial\phi}{\partial x}\right)^{n+\frac{1}{2}} &= \frac{1}{2}\frac{\partial}{\partial x}\left(k\frac{\partial\phi}{\partial x}\right)^{n+1}+\frac{1}{2}\frac{\partial}{\partial x}\left(k\frac{\partial\phi}{\partial x}\right)^{n}\\ Q^{n+\frac{1}{2}} &= \frac{1}{2}Q^{n+1}+\frac{1}{2}Q^{n}\end{aligned}$$

If replace $n+\frac{1}{2}$ term with n term, the Equation 9.14 become explicit in time and written as:

$$\begin{aligned}\phi^{n+1}-\phi^{n} &= -\Delta t\left[U^{n}\frac{\partial\phi}{\partial x}-\frac{\partial}{\partial x}\left(k\frac{\partial\phi}{\partial x}\right)+Q\right]^{n}\\ &\quad -\frac{\Delta t^{2}}{2}U^{n}\frac{\partial}{\partial x}\left[-U^{n}\frac{\partial\phi}{\partial x}+\frac{\partial}{\partial x}\left(k\frac{\partial\phi}{\partial x}\right)-Q\right]^{n}\end{aligned}\tag{9.15}$$

Equation 9.15 is the final form of explicit Characteristic Galerkin method. Following the explicit Characteristic Galerkin method, the semi-discrete form of step 1 (Equation 9.6) with intermediate momentum, $u_i^{\dagger}$ can be written as

$$\begin{aligned}\Delta U^{\dagger} &= -\Delta t\left[u_j\frac{\partial u_i}{\partial x_i}-Pr\frac{\partial\tau_{ij}}{\partial x_i}-J\sinh\psi\frac{\partial\phi}{\partial x_i}\right]^{n}\\ &\quad -\frac{\Delta t^{2}}{2}u_k\frac{\partial}{\partial x_k}\left[-u_j\frac{\partial u_i}{\partial x_i}+Pr\frac{\partial\tau_{ij}}{\partial x_i}+J\sinh\psi\frac{\partial\phi}{\partial x_i}\right]^{n}\end{aligned}\tag{9.16}$$

where

$$\begin{aligned}\tau_{ij} &= \frac{\partial u_i}{\partial x_j}+\frac{\partial u_j}{\partial x_i};\\ \Delta t &= t^{n+1}-t^{n}\end{aligned}$$

The pressure is solved at step 2, using the relation outlined in Equation 8.7.

$$\left(\frac{1}{\beta^{2}}\right)^{n}P^{n+1}-P^{n}=-\Delta t\frac{\partial u_i^{n+\theta_1}}{\partial x_i}\tag{9.17}$$

The momentum can now be corrected once the pressure has been determined, using the Equation 9.7 as

$$\Delta U^{\dagger\dagger} = -\Delta t \frac{\partial P^{n+\theta_2}}{\partial x_i} + \frac{\Delta t^2}{2} u_k \frac{\partial^2 P^{n+\theta_2}}{\partial x_i^2} \tag{9.18}$$

The resulting of momentum equation is written as below

$$\Delta u_i = \Delta U^{\dagger} + \Delta U^{\dagger\dagger} \tag{9.19}$$

Using the general relation

$$\begin{aligned} u_i^{n+\theta_1} &= \theta_1 u_i^{n+1} + (1-\theta_1) u_i^n \\ &= u_i^n + \theta_1 (\Delta u_i) \end{aligned} \tag{9.20}$$

into Equation 9.17 and substituting Equation 9.19 also into Equation 9.17,

$$\begin{aligned} \left(\frac{1}{\beta^2}\right)^n \Delta P &= -\Delta t \frac{\partial}{\partial x_i} \left[u_i^n + \theta_1 (\Delta u_i)\right] \\ &= -\Delta t \frac{\partial}{\partial x_i} \left[u_i^n + \theta_1 \left(\Delta U^{\dagger} - \Delta t \frac{\partial P^{n+\theta_2}}{\partial x_i}\right)\right] \end{aligned} \tag{9.21}$$

where the higher order terms are ignored. The final temporally discretised form of the pressure equation is given as

$$\left(\frac{1}{\beta^2}\right)^n \Delta P = -\Delta t \frac{\partial}{\partial x_i} \left[u_i^n + \theta_1 \Delta U^{\dagger} - \Delta t \theta_1 \frac{\partial P^n}{\partial x_i} - \Delta t \theta_1 \theta_2 \frac{\partial \Delta P}{\partial x_i}\right] \tag{9.22}$$

where

$$P^{n+\theta_2} = P^n + \theta_2 (\Delta P) \tag{9.23}$$

Here, $\theta_1 = 1$ and $\theta_2 = 0$ for fully explicit scheme.

The energy equation is temporally discretised by using the Characteristic Galerkin procedure next. The convective term that may cause oscillation will disappear after moving along the Characteristic. The discretised form of energy equation is written as:

$$\begin{aligned}\Delta T &= -\Delta t\left[u_j\frac{\partial T}{\partial x_j}-\frac{\alpha}{\alpha_\infty}\left(\frac{\partial^2 T}{\partial x_j^2}\right)\right]^n \\ &\quad +\frac{\Delta t^2}{2}u_k\frac{\partial}{\partial x_k}\left[u_j\frac{\partial T}{\partial x_j}-\frac{\alpha}{\alpha_\infty}\left(\frac{\partial^2 T}{\partial x_j^2}\right)\right]^n\end{aligned} \tag{9.24}$$

9.3.2 Spatial Discretisation

The resulting equations are then spatially discretised using the Galerkin finite element procedure. The following form of approximation is employed for the variable:

$$u_i^\dagger=\sum_{a=1}^{m}N^a\overline{u}_i^{\dagger a};u_i=\sum_{a=1}^{m}N^a\overline{u}_i^a;P=\sum_{a=1}^{m}N^a\overline{P}^a;T=\sum_{a=1}^{m}N^a\overline{T}^a$$

The overline indicates a nodal quantity, m is number of nodes in the element and a represents a particular node. In the Galerkin approximation procedures, the equations are weighted by the shape function, N and then integrated over the domain by doing integration by parts and Green's Lemma (refer to Appendix D.1). Finally, use the boundary condition in the weak form.

The following weak forms of the three steps are obtained through applying Galerkin approximation:

Step 1: The weak form of Equation 9.16

$$\begin{aligned}\int_\Omega N^a\Delta U^\dagger d\Omega &= -\Delta t\left[\int_\Omega u_j\frac{\partial N^a}{\partial x_i}u_i d\Omega+Pr\int_\Omega\frac{\partial N^a}{\partial x_i}\tau_{ij}d\Omega-\int_\Omega J\sinh\psi\frac{\partial N^a}{\partial x_i}\phi d\Omega\right]^n \\ &\quad -\frac{\Delta t^2}{2}\left[-\int_\Omega u_k u_j\frac{\partial N^a}{\partial x_k}\frac{\partial u_i}{\partial x_i}d\Omega+\int_\Omega u_k\frac{\partial N^a}{\partial x_k}J\sinh\psi\frac{\partial\phi}{\partial x_i}d\Omega\right]^n \\ &\quad +\Delta t\left[Pr\int_\Gamma N^a\tau_{ij}\overline{n}d\Gamma\right]^n\end{aligned} \tag{9.25}$$

The viscous and stabilizing terms are integrated by parts and last term is the boundary integral arising from integration by parts.

Step 2: The weak form of Equation 9.22

$$\left(\frac{1}{\beta^2}\right)^n \int_\Omega N^a \Delta P d\Omega = \Delta t \int_\Omega \frac{\partial N^a}{\partial x_i}\left[u_i^n + \theta_1 \Delta U^\dagger - \Delta t \theta_1 \frac{\partial P^n}{\partial x_i} - \Delta t \theta_1 \theta_2 \frac{\partial \Delta P}{\partial x_i}\right] d\Omega$$
$$-\Delta t \int_\Gamma N^a \left[u_i^n + \theta_1 \Delta U^\dagger - \Delta t \theta_1 \frac{\partial P^n}{\partial x_i} - \Delta t \theta_1 \theta_2 \frac{\partial \Delta P}{\partial x_i}\right] \overline{n} d\Gamma \tag{9.26}$$

Step 3: The weak form of Equation 9.18

$$\begin{aligned}\int_\Omega N^a \Delta U^{\dagger\dagger} d\Omega &= -\Delta t \int_\Omega N^a \frac{\partial P^{n+\theta_2}}{\partial x_i} d\Omega + \frac{\Delta t^2}{2} \int_\Omega N^a u_k \frac{\partial^2 P^{n+\theta_2}}{\partial x_i^2} d\Omega \\ &= -\Delta t \int_\Omega N^a \left[\frac{\partial P^n}{\partial x_i} + \theta_2 \frac{\partial \Delta P}{\partial x_i}\right] d\Omega \\ &\quad -\frac{\Delta t^2}{2} \int_\Omega u_k \frac{\partial N^a}{\partial x_i} \frac{\partial P^n}{\partial x_i} d\Omega \end{aligned} \tag{9.27}$$

Step 4: The weak form of Equation 9.28

$$\begin{aligned}\int_\Omega N^a \Delta T d\Omega &= -\Delta t \left[\int_\Omega u_j \frac{\partial N^a}{\partial x_j} T d\Omega + \frac{\alpha}{\alpha_\infty} \int_\Omega \frac{\partial N^a}{\partial x_j} \frac{\partial T}{\partial x_j} d\Omega\right]^n \\ &\quad + \frac{\Delta t^2}{2} \left[\int_\Omega u_k u_j \frac{\partial N^a}{\partial x_k} \frac{\partial T}{\partial x_j} d\Omega\right]^n \\ &\quad + \Delta t \left[\frac{\alpha}{\alpha_\infty} \int_\Gamma N^a \frac{\partial T}{\partial x_j} \overline{n} d\Gamma\right]^n \end{aligned} \tag{9.28}$$

9.3.3 Matrix Form

It is convenient to use the matrix notation when the finite element formulation is carried out. The discrete matrix forms are given as:

Step 1: (Refer to Equation 9.25):

$$M \Delta U^\dagger = -\Delta t \left[C u_i + K - F\right] - \frac{\Delta t^2}{2} \left[-K_u u_i + F_u\right] + f_{1e} \tag{9.29}$$

where

$$\begin{aligned} M &= \int_\Omega N^T N d\Omega; C = \int_\Omega u_j N^T \frac{\partial N}{\partial x_i} d\Omega; K = \int_\Omega \frac{\partial N^T}{\partial x_i} \tau_{ij}; \\ F &= \int_\Omega N^T J \sinh\psi \frac{\partial N}{\partial x_i} \phi d\Omega; K_u = \int_\Omega u_k u_j \frac{\partial N^T}{\partial x_k} \frac{\partial N}{\partial x_i} d\Omega; \\ F_u &= \int_\Omega u_k \frac{\partial N^T}{\partial x_k} J \sinh\psi \frac{\partial N}{\partial x_i} \phi d\Omega; f_{1e} = \Delta t \int_\Gamma N^T \tau_{ij} \overline{n} d\Gamma; \end{aligned} \tag{9.30}$$

Step 2: (Refer to Equation 9.26):

$$M_p \Delta P = \Delta t[G u_i + \theta_1 G \Delta U^\dagger - \Delta t \theta_1 H P^n - \Delta t \theta_1 \theta_2 H \Delta P - f_p] \tag{9.31}$$

Rearrange the Equation 9.31:

$$(M_p + \Delta t \theta_1 \theta_2 H)\, \Delta P = \Delta t[G u_i + \theta_1 G \Delta U^\dagger - \Delta t \theta_1 H P^n - f_p] \tag{9.32}$$

where

$$\begin{aligned} M_p &= \int_\Omega N^T N d\Omega; G = \int_\Omega N^T \frac{\partial N}{\partial x_i} d\Omega; H = \int_\Omega \frac{\partial N^T}{\partial x_i} \frac{\partial N}{\partial x_i} d\Omega; \\ f_p &= \int_\Gamma N^T N \left[u_i^n + \theta_1 \left(\Delta U^\dagger - \Delta t \frac{\partial P^{n+\theta_2}}{\partial x_i} \right) \right] \overline{n} d\Gamma \end{aligned} \tag{9.33}$$

Step 3: (Refer to Equation 9.27):

$$M \Delta U^{\dagger\dagger} = -\Delta t \left[G\left(P^n + \theta_2 \Delta P\right) + \frac{\Delta t^2}{2} P P^n \right] \tag{9.34}$$

where

$$P = \int_\Omega u_k \frac{\partial N^T}{\partial x_k} \frac{\partial N}{\partial x_i} d\Omega \tag{9.35}$$

Step 4: (Refer to Equation 9.28):

$$\Delta T = -M_T^{-1} \Delta t \left[C_T T + K_T T - f_T - \frac{\Delta t}{2} K_{uT} T \right] \tag{9.36}$$

where

$$
\begin{aligned}
M_T &= \int_\Omega N^T N d\Omega; C_T = \int_\Omega N^T u_j \frac{\partial N}{\partial x_j} d\Omega; K_T = \int_\Omega \frac{\partial N^T}{\partial x_k} \frac{\partial N}{\partial x_j} d\Omega; \\
f_T &= \int_\Gamma N^T \frac{\partial N}{\partial x_j} T \overline{n} d\Gamma; K_{uT} = \int_\Omega u_k u_j \frac{\partial N^T}{\partial x_k} \frac{\partial N}{\partial x_j} d\Omega;
\end{aligned} \tag{9.37}
$$

9.4 Artificial Compressibility (AC)

When fluid is incompressible, the speed of sound approaches infinity. Hence, the time step limitations arise. An artificial compressibility (AC) method can be employed to eliminate the restriction posed by the speed of sound at step 2 of CBS algorithm [38]. AC parameter, β is given either as a constant or based on the convective or diffusive velocity. It is locally computed using the following relation;

$$\beta = max\left(\epsilon, u_{conv}, u_{diff}\right) \tag{9.38}$$

Here, $\epsilon = 0.5$ is to ensure β is not approaching zero. u_{conv} and u_{diff} are convective velocities and diffusion velocities which are given as:

$$u_{conv} = \sqrt{u_i u_i}; \tag{9.39}$$

$$u_{diff} = \frac{2Pr}{h} \tag{9.40}$$

where Pr is the Prandtl number and h is the element size.

9.5 Local Time Stepping

In the CBS scheme, θ_1 will always be taken to satisfy $\frac{1}{2} \leq \theta_1 \leq 1$ to ensure pressure stability. Parameter θ_2 in step 2 is used to create the explicit or semi-implicit schemes. Here, a fully explicit scheme with $\theta_2 = 0$ is used.

The efficiency of an explicit time stepping algorithm can be increased by introducing a local time stepping scheme, which can accelerate the solution to steady state. The local time step is dependent on the height of element and is calculated at every node.

Subsequently, fewer iteration are required compare to global time steping scheme to reach steady state.

In local time stepping, we use minimum time step found at each node. The time step limitation is explained as.

$$\Delta t = \frac{h}{|u| + \beta} \tag{9.41}$$

where h is the element size and β is artificial speed of sound. The time step limitations for convection and diffusion velocities for using artificial compressibility method can be written as

$$\begin{aligned} \Delta t_{conv} &= \frac{h}{u_{conv} + \beta} = \frac{h}{\sqrt{u_i u_i} + \beta} \\ \Delta t_{diff} &= \frac{h^2}{2Pr} = \frac{h}{u_{diff}} \end{aligned}$$

The smallest time stepping is chosen between convection time step and diffusion time step. This value is then multiply with a safety factor, SF which is a constant [101, 102], that is,

$$\Delta t = SF \times min\left(\Delta t_{conv}, \Delta t_{diff}\right) \tag{9.42}$$

In an unstructured mesh, the element size is not unique to each node. Therefore, the time step limit at each node is calculated by assigning the minimum value for such node calculated from all element connected to that node.

9.6 Element Height

The element height of three dimensional elements is defined as:

$$h_{ie} = min\left(\frac{3V}{OppositeFaceArea}\right)_{ie} \tag{9.43}$$

where V is volume of the three dimensional tetrahedron.

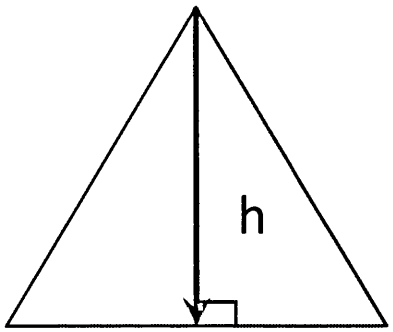

Figure 9.2: Element height

9.7 2D Algorithm Verification

To ensure the accuracy of the CBS algorithm, zeta potential distribution and velocity profile in two dimensional space are compared here with the experimental and analytical results which were presented by Kim et al [4], Dutta et al [97], Yang et al [96, 103], Patankar et al [34] and Hu et al [29].

9.7.1 Comparison with experimental velocity profile

Kim et al [4, 97] experimentally studied electro-osmotic flow driven across the grooved channel by subjecting the flow with an external electric field of 10 V/mm. The grooved channel has a width of 300 μm and depth of 7 μm. To obtained a thin electric double layer, high concentration ($1 \times 10^{-5} M$) of electrolyte was used. Kim et al [4, 97] obtained velocity profile from two dimensional image which was captured by a μ-PIV system. The electro-osmotic force produces a plug like velocity profile with a speed of 389 $\mu m/s$. The zeta potential was estimated from Equation 5.9 which is about 50 mV.

The non dimensional parameters that are used in numerical simulation are

J=211; E_x=386; ζ=-2; κa=98; Pr=6.2

The bulk ionic concentration of the electrolyte in this experiment was about $6.022 \times 10^18/m^3$ (Refer to Appendix C.2). 2D channel with width and length of 1 and 3.33 respectively was used in the numerical simulation as shown in Figure 9.3(a). Figure 9.3(a) shows the mesh of the channel. The external electric field is distributed linearly over

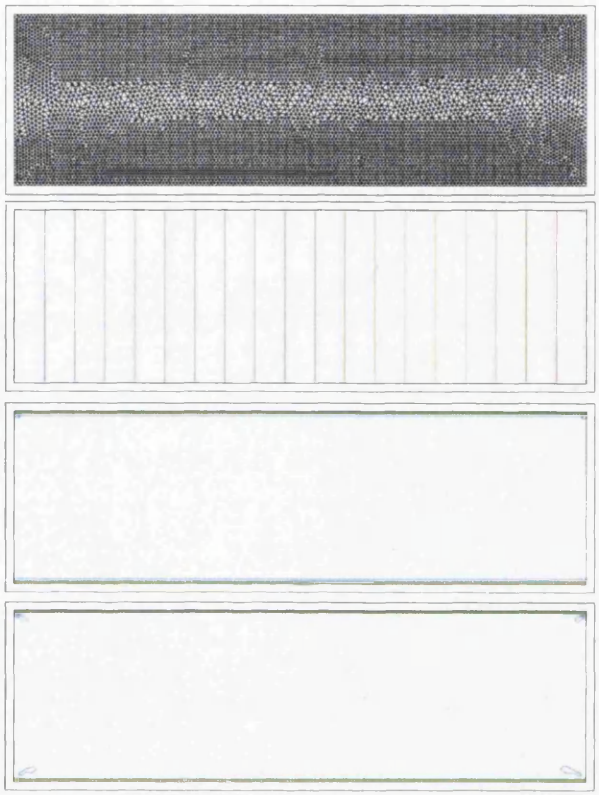

(a)

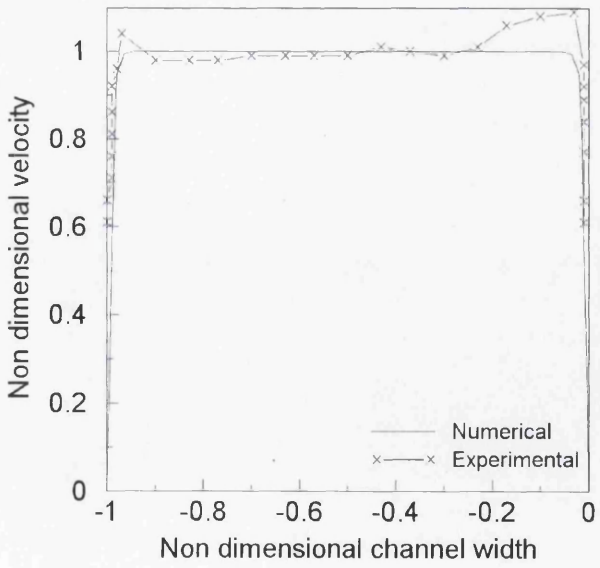

(b)

Figure 9.3: (a)From top 2D channel mesh, external potential, internal potential and velocity distribution (b)Comparison with experimental data from Kim et al [4].

the channel length. The channel has a very thin EDL with respect to the channel width and it produces steep gradient in the internal potential distribution and velocity profile as shown in Figure 9.3(b). As seen, the numerical results agree well with the experimental data.

9.7.2 Comparison with analytical solution

The numerical result were also compared to an analytical solution. Both the internal potential distribution profile and velocity profile were compared.

For small zeta potential, the hyperbolic function of the internal potential is reduced and gives Equation 2.13. The internal potential near the wall is equal to zeta potential. The analytical solution for internal potential is given by [96, 34]

$$\psi = -\frac{cosh[\kappa(Y - \frac{1}{2})]}{cosh[\frac{\kappa}{2}]} \tag{9.44}$$

The internal potential distribution for the diffuse layer near the wall, ψ, used by Hu et al [29] is given by

$$\psi = 2ln\frac{1 + exp(-\kappa Y)tanh\frac{1}{4}\zeta}{1 - exp(-\kappa Y)tanh\frac{1}{4}\zeta} \tag{9.45}$$

where Y is the distance from the wall. Equation 9.45 was used in present work to obtain accurate internal potential distribution. The velocity, u was obtained through simulation of EOF in 2D channel. The analytical expression for velocity profile is [104]:

$$u = 1 - \zeta\left(2ln\frac{1 + exp(-\kappa Y)tanh\frac{1}{4}\zeta}{1 - exp(-\kappa Y)tanh\frac{1}{4}\zeta}\right) \tag{9.46}$$

where ζ is referred to the zeta potential. The parameters used in the numerical simulation are:

J=8.73 to 139.69; E_x=386; ζ=-1; κa=20 to 80; Pr=6.2

The internal potential and velocity were plotted over the half of the channel width as shown in Figure 9.4. Here, different κa value were used. At wide EDL layer such as $\kappa a = 20$, the internal potential is less steep compared to $\kappa a = 80$. The EDL thickness also affect the velocity because it is part of the added source term in momentum equation.

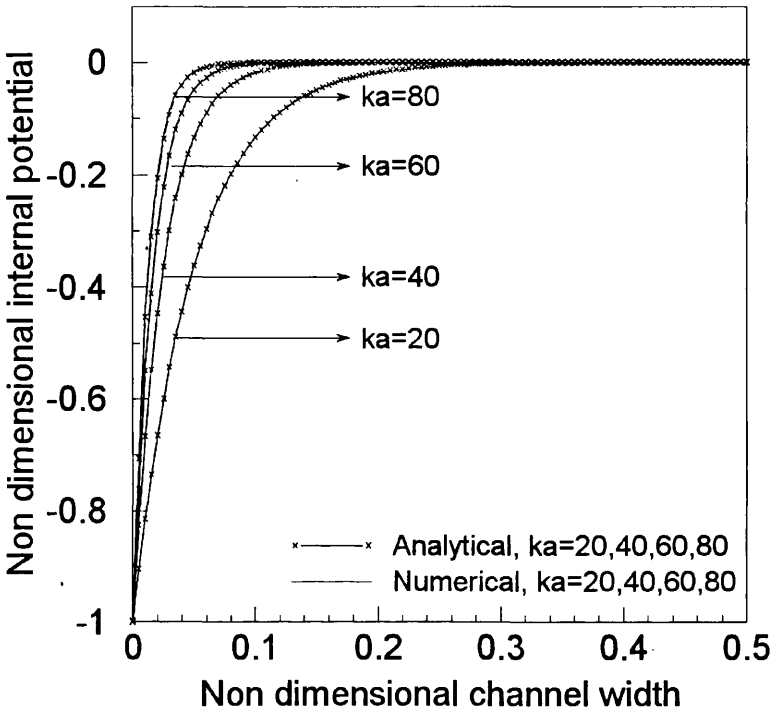

(a)

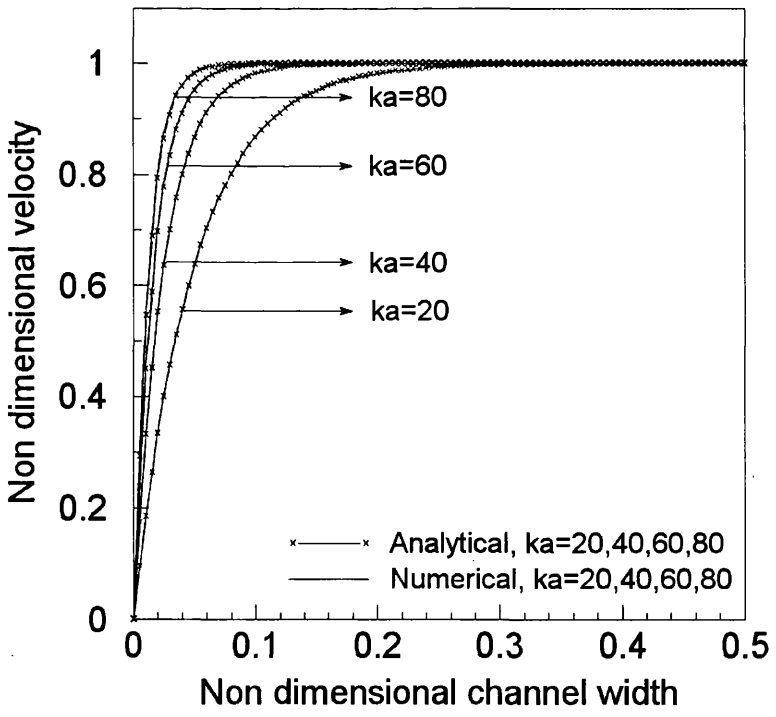

(b)

Figure 9.4: Comparison of (a)Internal potential (b)Velocity profile with analytical solution with 43962 elements and 22386 nodes.

Table 9.1: Relationship between ϵ and κa.

ϵ	κa
191.0	20
47.7	40
21.2	60
11.9	80

As seen in Figure 9.4, the comparisons of both analytical solution and numerical solution are almost identical. The velocity of the numerical solution has been normalised with

$$\overline{u} = \frac{\overline{u}_{num}}{\overline{u}_{max}} \tag{9.47}$$

where $\overline{u}_{num}$ and $\overline{u}_{max}$ are the velocity and maximum velocity that are obtained from numerical simulation [60].

The result presented in Figures 9.3 and 9.4 prove that the 2D model developed produces results that are accurate representation of electro-osmotic flow.

9.8 Parametric Study

The effects of κa, zeta potential, external electric field, Prandlt number and parameter J on the electro-osmotic flow field are analysed in the following sections. Two dimensional channel with non dimensional width and length of 0.33 and 3.5 was used in the present study. Fully developed electro-osmotic flow is considered.

9.8.1 Influence of κa on Flow Field

Different cases of κa are considered in the present study. At small dielectric constant of electrolyte will generate high κa value as shown in Table 9.1. The non dimensional parameters used in the present simulation are:

J=20; E_x=4.06; ζ=-1; κa=20, 40, 60 and 80; Pr=6.2

As seen in Figure 9.5(a), small dielectric constant ($\kappa a = 80$), the internal potential variation is steep close to the walls. As the κa value is reduced, the internal potential

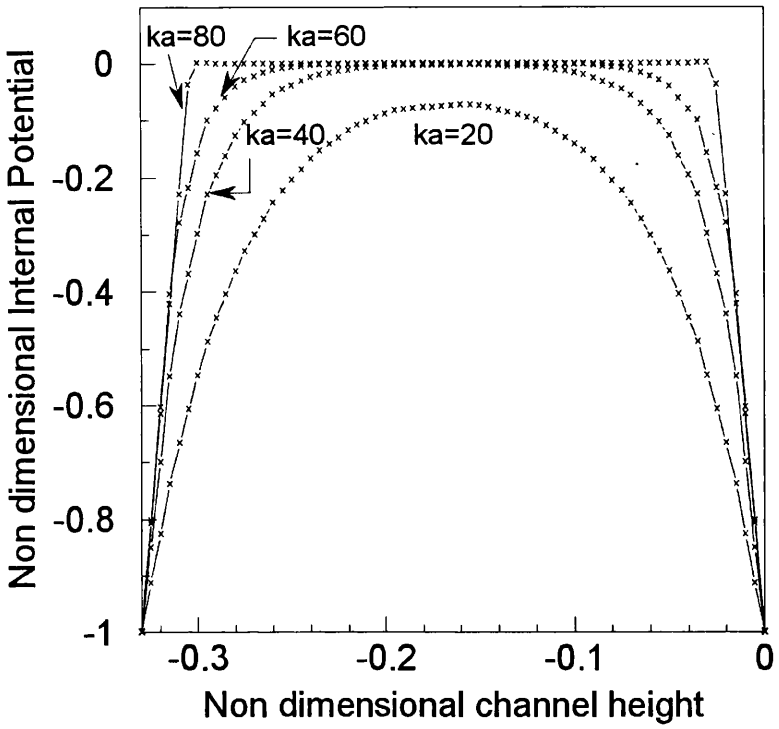

(a)

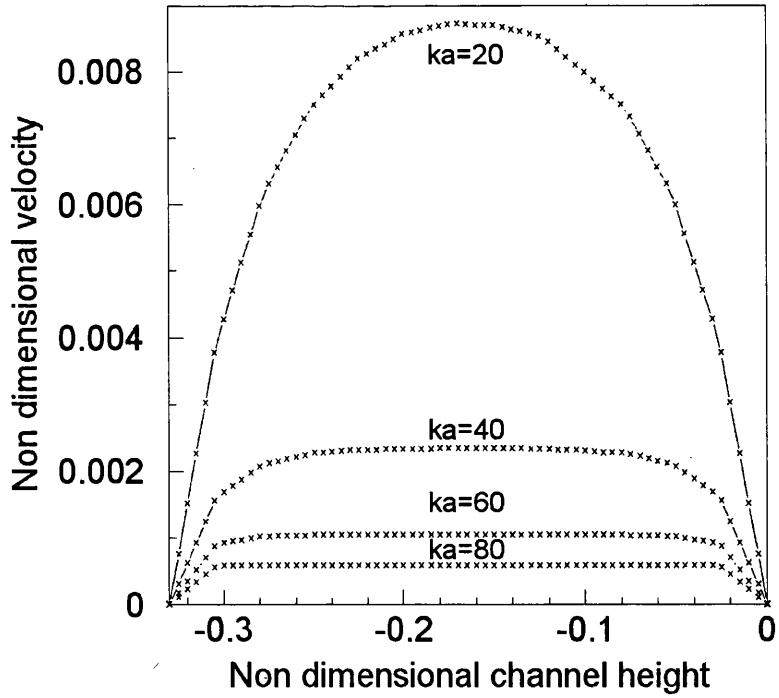

(b)

Figure 9.5: Variation of internal potential and velocity profile with κa at a bulk ionic concentration of 6.022×10^{19}.

Table 9.2: Relationship between n_0, κa and parameter J.

bulk ionic concentration, n_0 (m^{-3})	EDL thickness $1/\kappa$ (μm)	κa	J
2.475×10^{19}	1.4990	20	8.6
9.890×10^{19}	0.7499	40	34.5
2.225×10^{20}	0.5000	60	77.5
3.955×10^{20}	0.3750	80	137.8

gradient becomes less steeper.

The internal potential distribution contributes to the source term in the momentum equation. The characteristic plug like velocity profile arises from the plug like internal potential profile as shown in Figure 9.5(b). The reduction of κa value produces large velocity (reduction in cross sectional area).

9.8.2 Influence of Parameter J on Flow Field

Table 9.2 shows the influence of κa, EDL and bulk ionic concentration on J value. These values are used in the calculations. The parameters used in the present study are:

J=8.6, 34.5, 77.5 and 137.8; E_x=4.06; ζ=-1;
κa=20,40,60 and 80; Pr=6.2

A similar internal potential distribution as previous simulation has been obtained at $\kappa a = 20$ to 80. At thin EDL ($\kappa a = 80$), the internal potential distribution is steeper near the channel walls compared to the lower κa value.

As described in the previous section, the velocity value increases when κa value is decreased. However, here, the non dimensional maximum velocity values are identical between $\kappa a = 40$ and 80 and plug like velocity profiles obtained are shown in Figure 9.6(b). This is due to the fact that J values are increased along with κa values. Numerically, high value of parameters κa and J by increasing bulk ionic concentration of electrolyte are desired to increase the electro-osmotic velocity. However, large value of bulk ionic concentration will result in bubbles generation which is caused by Faradaic process which was explained in Chapter 6. Thus, in the simulation, reasonable parameters κa and J have to be selected to avoid bubbles generation in practical.

Continuous reduction of κa value will increase the thickness of EDL and result in overlapping EDL. This phenomena can be seen at $\kappa a = 20$. The internal potential

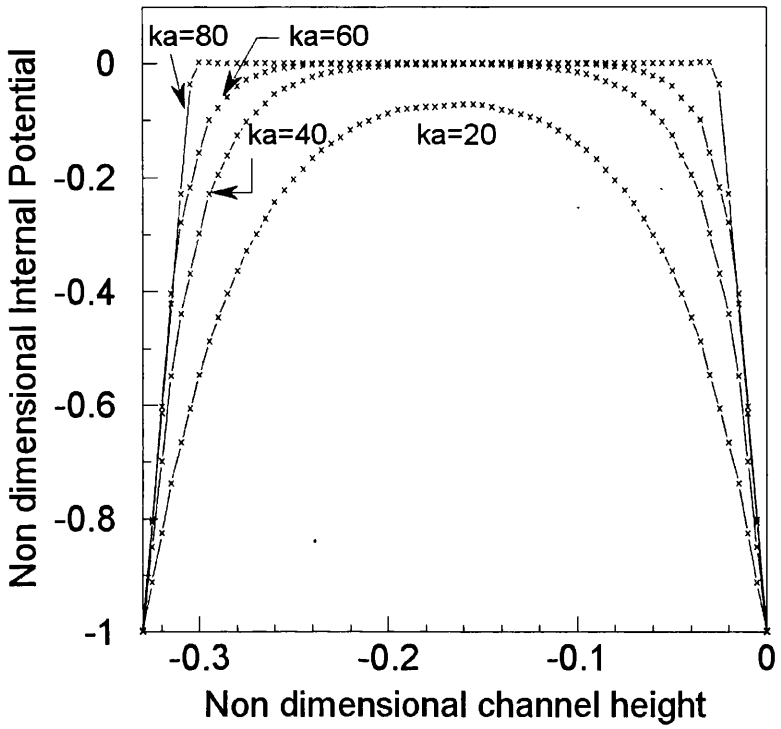

(a)

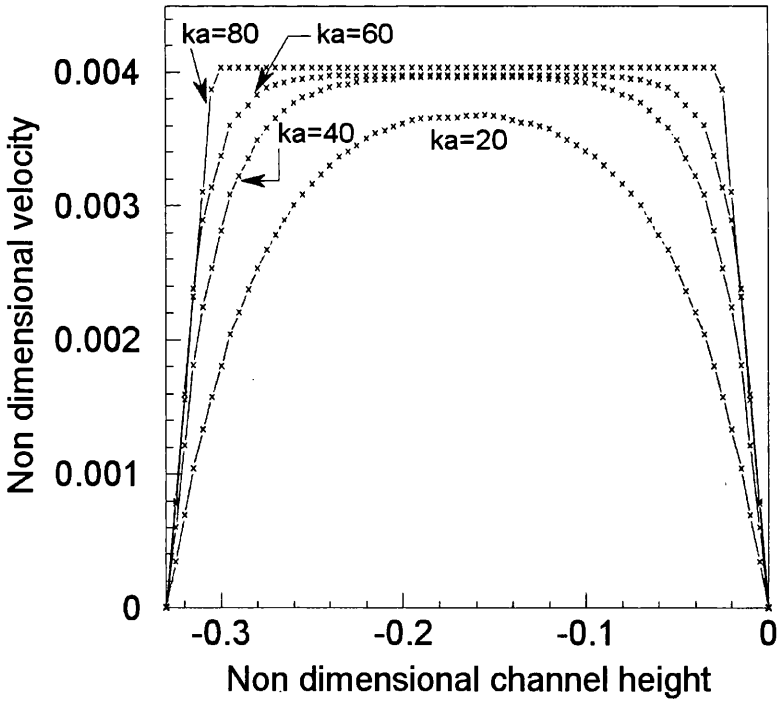

(b)

Figure 9.6: Variation of internal potential and velocity profile with κa between 20 to 80.

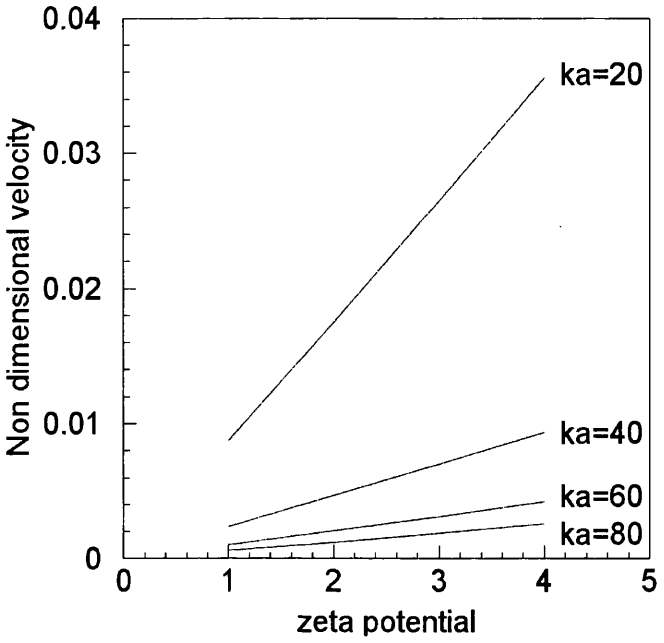

Figure 9.7: Velocity profile for ζ=-1 to -4 and κa=40 to 80.

distribution becomes parabolic at this κa value. The non zero internal potential values at $\kappa a = 20$ clearly shows that the EDL form both sides are overlapping.

9.8.3 Influence of Zeta Potential on Flow Field

The zeta potential describes the surface energy of the channel wall. Here, Debye Huckel approximation should not be applied if accurate velocity approximation is required. In this section, the effect of zeta potential to the flow field is studied. The parameters used are:

J=20; E_x=4.06; ζ=-1 to -4; κa=40 to 80; Pr=6.2

As seen in Figure 9.7, the velocity is increasing linearly with increasing zeta potential. The zeta potential depends on the ionic strength of electrolyte on a surface. At large zeta potential, the ionic strength of electrolyte is large and more ions are attracted towards the surface and forms a thick layer of EDL. When an external electric field is applied, large amount of ions will move to one of the electrodes and will drag along more electrolyte

molecules. Thus, at higher zeta potential values, larger velocity value are obtained.

Figure 9.7 also shows that a decrease in κa value, leads to higher velocity values as demonstrated in previous section. However, zeta potential has stronger influence on velocity at smaller κa values.

9.8.4 Influence of External Electric Potential on Flow Field

The external potential of 10 to 50 V/cm are used in present study. The external potential and κa both are varied and the parameters used are:

J=20; E_x=4.06, 8.11, 12.17, 16.22 and 20.28; ζ= -1; κa=30; Pr=6.2

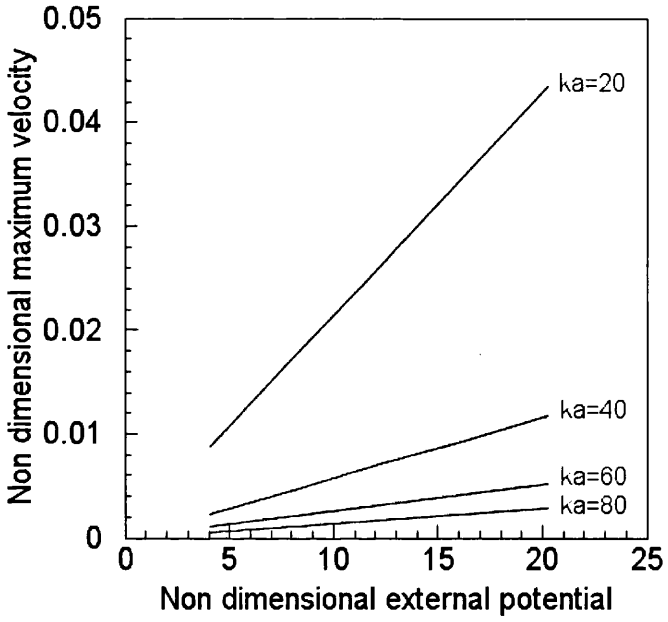

Figure 9.8: Velocity profile of straight channel for E_x = 4.06 to 20.28.

The external potential has no influence on internal potential distribution. However, the increment of the external potential difference would increase the maximum velocity as shown in Figure 9.8. As seen in the figure, as κa value increases, a reduction of maximum velocity is observed.

The external electric field contributes to the source term in momentum equation. It controls the velocity through by acting upon the ions inside the EDL. As the field strength

increases, the ions are attracted towards an electrode due to higher gradient of electric field. As the ions move, the bulk of fluid is also dragged along with through the viscous force. Hence, the increasing of electric field produces a larger driving force and increase the velocity of ions in the fluid. However, the drawback of using large external electric field is it could produce Joule heating which will arise the temperature of the system and ultimately affect the electro-osmotic flow [105]. Therefore, the external electric potential optimisation is essential to avoid Joule heating in the system.

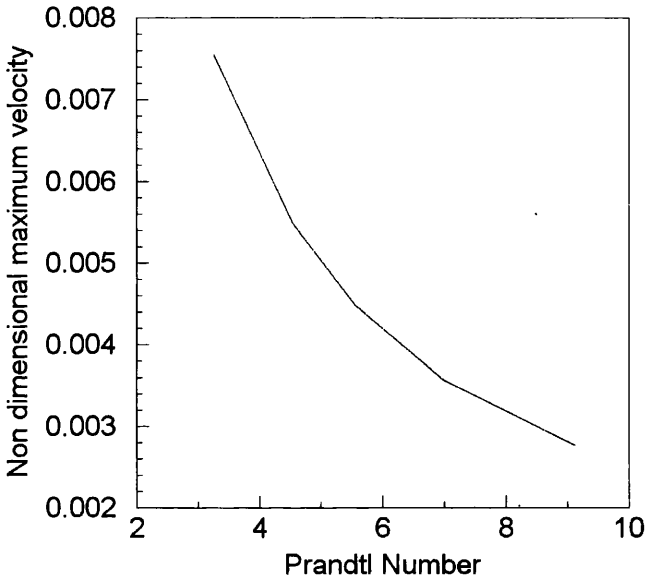

Figure 9.9: Velocity distribution against Pr variation.

9.8.5 Influence of Prandlt number on Flow Field

Prandtl number contributes to the viscosity term in momentum equations. It describes the ratio of viscosity and thermal diffusivity. An increasing in temperature reduces the viscosity of electrolyte and thus reduces the Prandtl number. The variation of temperature, viscosity and Prandtl number are shown in Table 9.3.

In this section effect Pr on flow field are studied with the following parameters.
J=33.93 to 39.14; E_x=4.27 to 3.63; ζ=-1 to -0.87 ;
κa=41.35 to 37.80; Pr= 9.14 to 3.26

Table 9.3: Parameters calculation with variation temperature between 283 K to 333 K

T (K)	ζ	ϕ	κa	μ (Ns/m^2)	$\rho(kg/m^3)$	$\alpha(m^2/s)$	Pr	J
283	1.03	4.27	41.05	1.31E-03	999	1.43E-07	9.14	33.93529
293	0.99	4.13	40.35	1.00E-03	997	1.44E-07	6.90	34.89702
303	0.96	3.99	39.67	7.98E-04	995	1.44E-07	5.56	35.94681
313	0.93	3.86	39.03	6.53E-04	992	1.45E-07	4.55	37.02121
333	0.87	3.63	37.8	44.67E-04	983	1.46E-07	3.26	39.14160

The results are shown in Figure 9.9. The figure shows that an increase in Prandtl number indicates the decrease in electro-osmotic velocity. This is due to the electrolyte larger viscosity which gives the friction to the flow.

However, using the electrolyte with small Prandlt number of 3.26, the electrolyte has smaller viscosity and leads to large electro-osmotic velocity. To reduce the viscosity, higher temperature of electrolyte is needed. However, high temperature in the electrolyte results in bubbles generation and disruption of the continuum of flow. Thus, it leads to the break down of electrical connection of both electrodes in the electro-osmotic pump ultimately stop the electro-osmotic operation [105].

9.9 2D and 3D Channel Comparison

Three dimensional algorithm was also developed to simulate the EOF problems. In order to validate this 3D algorithm, a comparison was made between the results that were collected through the 2D algorithm and 3D solutions produced here.

Both 2D and 3D models as shown in Figure 9.10. The channel has non dimensional width of 1, height of 0.33 and length of 3.33. Mesh near the channel wall is refined to capture the steepness of the internal potential and velocity. Mesh refinement will be discussed in detail in the next chapter. The parameters used in this present study are:

J=20; E_x=4.06; ζ=-0.75; κa=31; Pr=6.2

The external potential field and internal potential distribution and velocity profile are shown in Figure 9.10. The internal potential distribution and velocity profile of both 2D and 3D channel are plotted across channel height as shown in Figure 9.11. The comparison between them shows good agreement. The velocity profile for the 3D problem was obtained

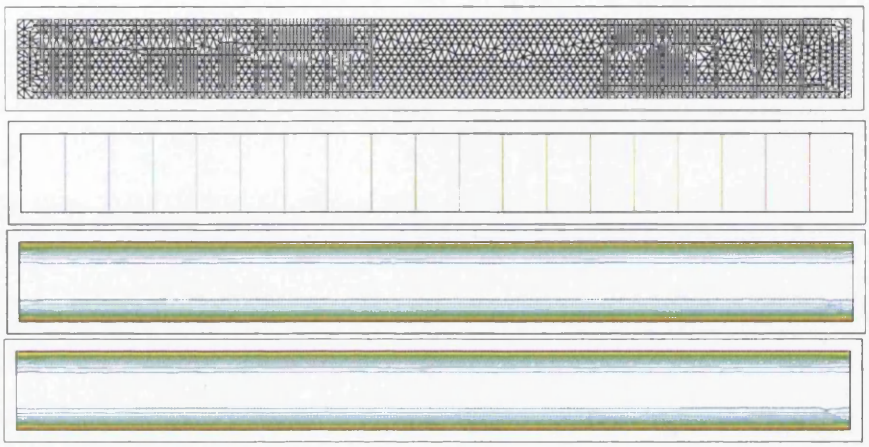

(a) From top: 2D channel mesh, external potential, internal potential, velocity distribution

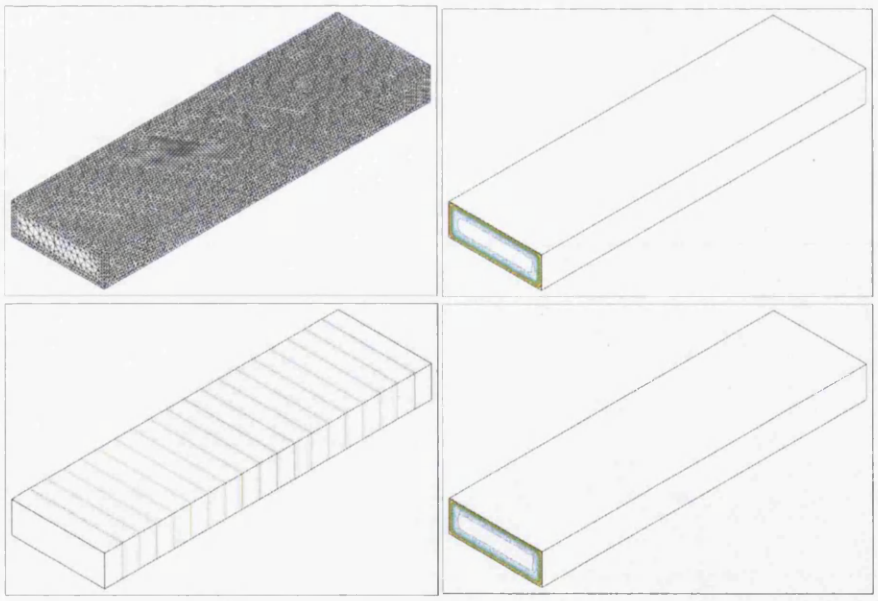

(b) 3D channel mesh, external potential(bottom left), internal potential (top right), velocity distribution (bottom right)

Figure 9.10: Two and three dimensional channel models.

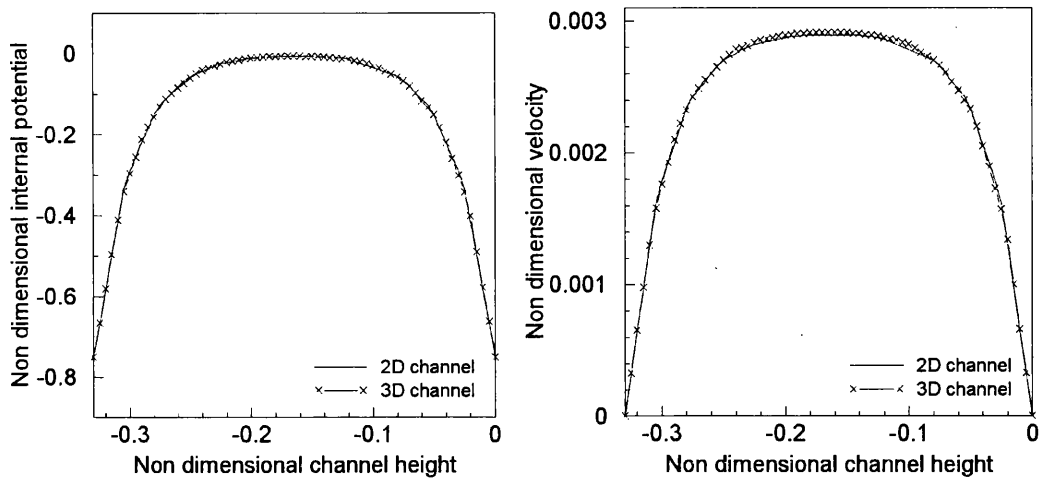

(a) (b)

Figure 9.11: (a)Internal potential (b)Velocity profile in 2D and 3D channels.

at the height of the channel.

9.10 Summary

In this chapter, the pseudo time term was added to the electric field equations to explicitly discretise these equations. As steady state solution is reached, the pseudo time term becomes negligible small. The AC-CBS algorithm was used to discretise the Navier Stokes equations. This method splits the momentum equation by an introducing intermediate momentum field. The advantages of using AC-CBS algorithm include reduction in oscillations. The Navier Stokes equations were spatially discretised by the finite element method

The velocity and internal potential distributions of two dimensional algorithm were agree excellently with the experimental data and analytical solution. The effects of κa, zeta potential, external electric field, Prandlt number and parameter J on the fluid flow were also investigated in this chapter.

At large κa values (small dielectric constant or thin EDL), the internal potential becomes steep near the channel walls and plug like velocity profile developed. However,

larger κa value is general reduces the maximum flow velocity.

At the last section of this chapter, comparisons between two dimensional and three dimensional algorithms were shown. Since the accuracy of both 2D and 3D models have been reasonably verified, the 3D algorithm can now be employed to solve the flow and heat transfer in the proposed heat spreader.

Chapter 10

Electro-osmotic Flow and Heat Transfer In The Heat Spreader

10.1 Introduction

In this chapter, electro-osmotic flow and heat transfer through a three dimensional electro-osmotic heat spreader is studied. Several meshes are generated to study the characteristics of the electro-osmotic heat spreader. A suitable mesh is selected via a mesh sensitivity study for the analysis. The three dimensional algorithm which has been verified in the previous chapter is used here. The numerical results obtained are compared with experimental data which are presented in Chapter 5. The solution consists of two parts. In the first part steady state velocity field is obtained by time stepping the momentum equations to steady state. Once the steady state velocity field is obtained, then every equation is solved to obtain a steady state temperature field.

10.2 Mesh Convergence Study

The 3D heat spreader with fins and a straight micro-channel is shown in Figure 10.1(a). This model is designed to study the electro-osmotic flow and heat spreader shown in Figure 3.1. Note that only the pumping section of the heat spreader is included in the calculation. A non dimensional micro-channel with length, width and depth of 333, 1 and

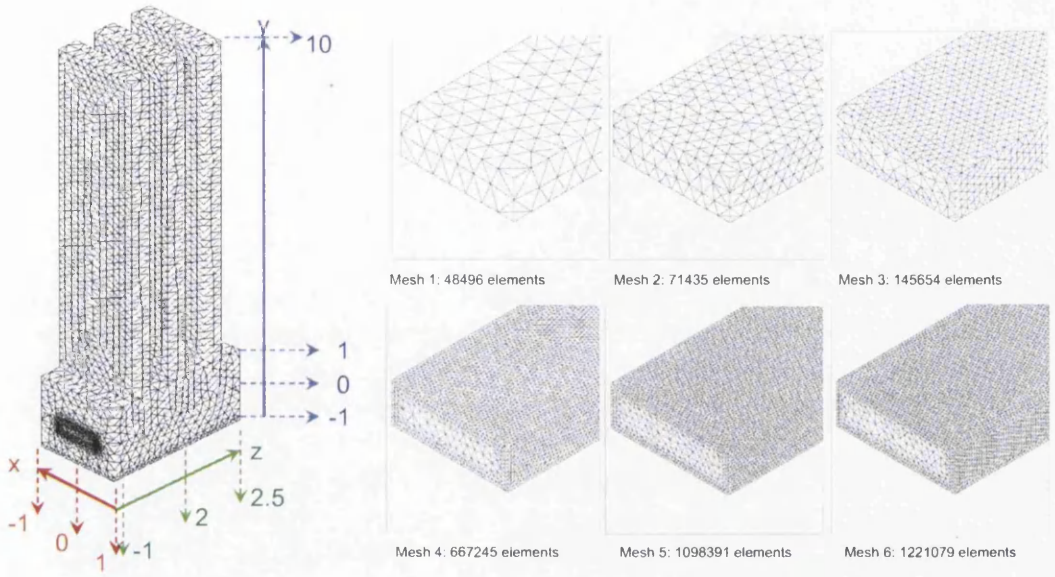

(a) (b)

Figure 10.1: (a)Geometry of heat spreader model (b)Meshes used for the mesh refinement study for EOF in a straight micro-channel.

0.33 respectively is embedded into a solid material. To reduce computational time, the channel length has been shortened to 3.5 without losing accuracy.

The correct internal potential distribution is important in producing a flat velocity profile. Therefore, to capture the steep gradient of internal potential near the wall, mesh refinement is required near the channel walls. However, excessive refinement requires large amount of computational time. Thus a mesh convergence study is carried out to identify a suitable mesh that is sufficiently fine to carry out the calculation.

Different meshes as shown in Figure 10.1(b) are generated for simulation. Each mesh is refined near the channel surface. All the velocity and zeta potential profiles were taken at $y = 0$ to -0.33 and $z = 2$, in the middle of the channel. The parameters used in the mesh sensitivity study are:

J=20; E_x=3.89; ζ=-1; κa=30; Pr=6.2

The results for both velocity and internal potential are shown in Figure 10.2. The velocity deviation, D_u in percentage is:

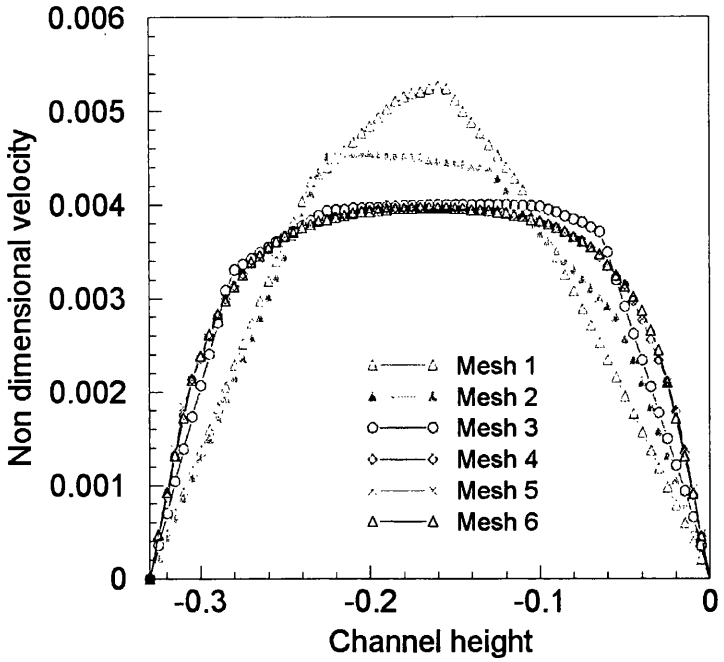

(a) Velocity profile on different meshes

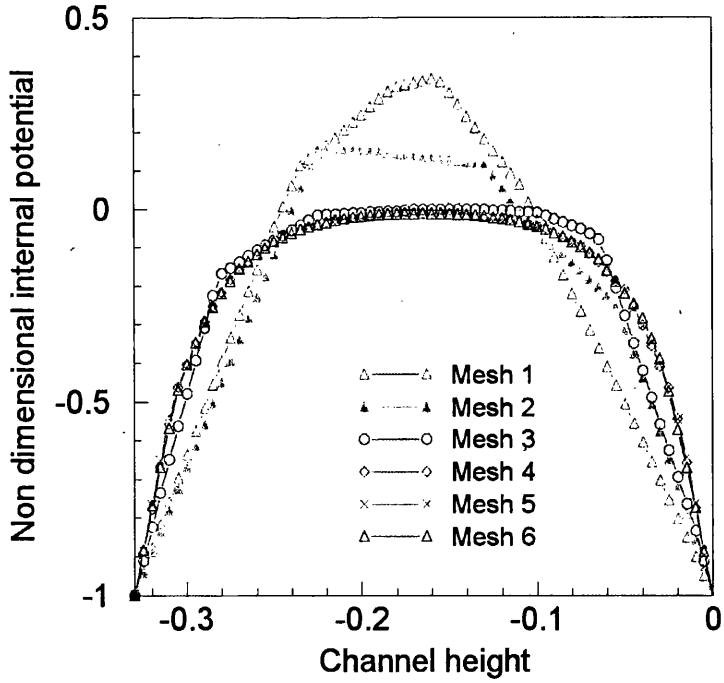

(b) Internal potential profile on different meshes

Figure 10.2: Internal potential and velocity profiles.

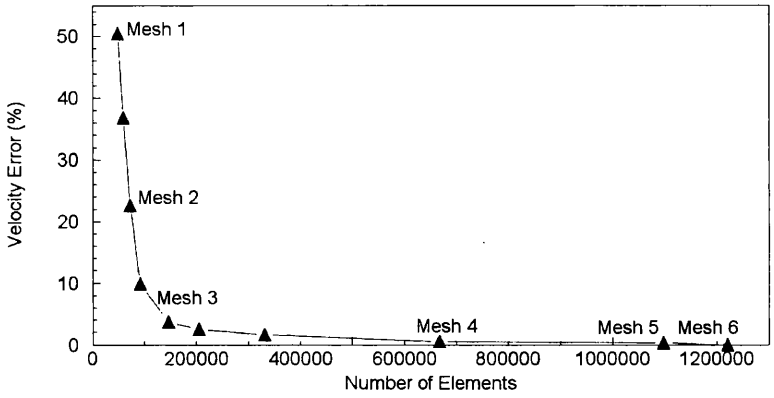

Figure 10.3: Percentage of velocity error for different meshes.

$$D_u = \frac{|max(u_{Mesh\ i}) - max(u_{Mesh\ 6})|}{max(u_{Mesh\ 6})} \times 100 \tag{10.1}$$

where i = 1 to 6 and $max(u_{Mesh\ 6})$ is the maximum velocity of Mesh 6. Figure 10.3 shows the velocity deviation of Mesh 1 to 6 with respect to number of elements. Meshes 1, 2 and 3 show a very approximate profile, with almost 50, 23 and 4 percent deviation respectively from the converged velocity of Mesh 6. In addition, these meshes are too coarse to capture the velocity values and result in asymmetrical profiles.

Meshes 4 and 5 are sufficiently fine to provide accurate results in terms of both internal potential and velocity of electro-osmotic flow. Therefore, Mesh 4 is assumed to be sufficiently fine to carry out all studies. It is sufficiently refined to correctly capture the steep gradient and does not require as much computational time as Mesh 5 or Mesh 6.

10.3 Electro-osmotic Flow Model through Straight Channel

In Chapter 5, some experimental results are given for straight rectangular channels. In this section, numerical results are presented along with comparisons with experimental data. Straight channels B, C and D given in Chapter 5 have been modelled here. The micro-channel in those samples have a width and depth of 30 μm and 10 μm respectively. Mesh 4 described in the previous section is used in present study. DI water is used as

working electrolyte. The zeta potential for the samples B to D are 19.26, 13.48 and 29.54 mV respectively. Additionally, the external potential for those samples are 10, 20, 40 V/cm.

The parameters used in the numerical simulation are calculated by using the reference quantities and values given in Table 10.1. The non-dimensional parameters used in the calculations are:

J=20; E_x=4.06, 8.11 and 16.22 ; ζ=-0.75, -0.53 and -1.15;
κa=30; Pr=6.2

Table 10.1: Parameter, reference quantities and other values for numerical simulation.

Parameter	Value
L_∞	width of channel
z	1
e	$1.602 \times 10^{-19} C$
k_B	$1.3806 \times 10^{-6} m^2 kg/s^2 K$
T_∞	298 K
ψ	-0.75, -0.53 or -1.15 (19.26, 13.48 and 29.54 mV)
ϕ	4.06, 8.11 or 16.22 (equal to electric field of 10, 20 or 40 V/cm)
ϵ_∞	78.4
ϵ_0	$8.85 \times 10^{-12} C/Vm$
n_0	$6.022 \times 10^{-19} m^{-3}$
ka	30
μ	$8.91 \times 10^{-4} Ns/m^2$
c_p	4181 J/kgK
k_∞	0.6 W/mK
ρ	997 kg/m^3
α_∞	$1.44 \times 10^{-7} m^2/s$

The DI water has low ionic concentration of $6.022 \times 10^{19} m^{-3}$. It produces EDL thickness, $1/\kappa$ about 1 μm [96]. The EDL layer is considered thin with respect to the channel dimensions of 30×10 μm.

Figure 10.4(a) shows the plug like internal potential distribution of sample B at $\kappa a = 30$. This leads to plug like velocity profile as shown in Figure 10.4(b). As expected, the velocity increases as the external potential difference is increased.

The non-dimensional velocity is now converted into dimensional value. The dimensional numerical result is compared against the experimental data in Figure 10.5. Both data are given in Table 10.2. The deviation between numerical and experimental results is less than 10 percent. Excellent agreement between the numerical model and experimental

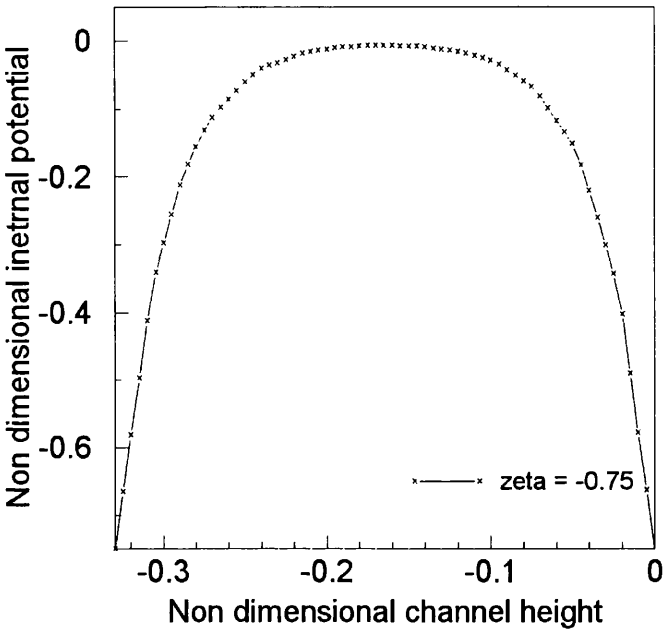

(a)

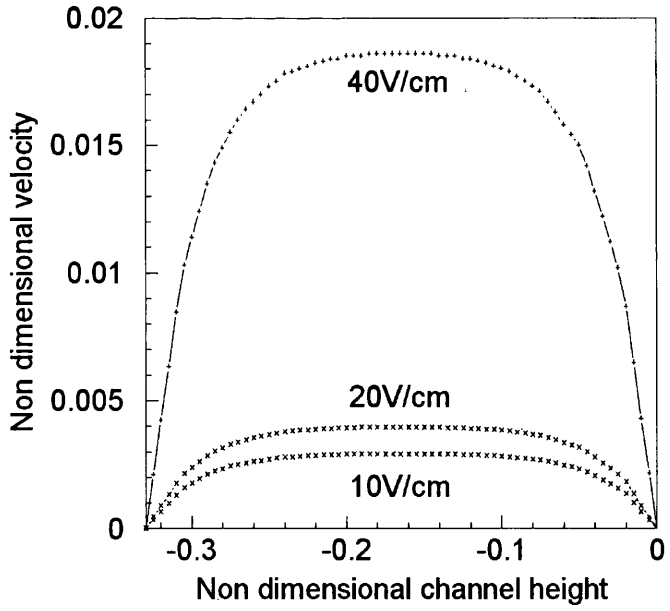

(b)

Figure 10.4: Internal potential and velocity profile of straight channel with external potential of 10, 20 and 40V.

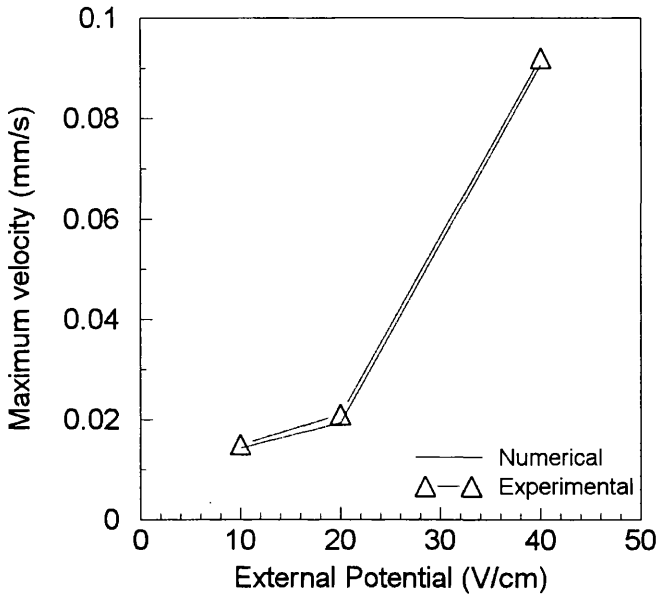

Figure 10.5: Maximum velocity obtained from experimental and numerical results at external potentials of 10, 20 and 40 V/cm.

data is observed.

Table 10.2: Comparisons of the numerical result and experimental data for electro-osmotic flow through a straight rectangular micro-channel.

Voltage (V)	Non-dimensional velocity	Numerical velocity (mm/s)	Experimental velocity (mm/s)	Error (%)
10	0.0028	0.014	0.015	9.2
20	0.0040	0.019	0.021	7.3
40	0.0185	0.090	0.092	2.1

10.4 Conjugate Heat Transfer Model

A conjugate heat transfer problem of an electro-osmotic flow (EOF) based micro-cooling system has been numerically studied here. The AC-CBS algorithm has been employed to temporally discretize the energy equations. The spatial discretization is carried out using the finite element method.

Now, the channel flow solutions obtained in the previous section is embedded in the heat spreader (Figure 10.6). The liquid is forced to flow through the channel and heat

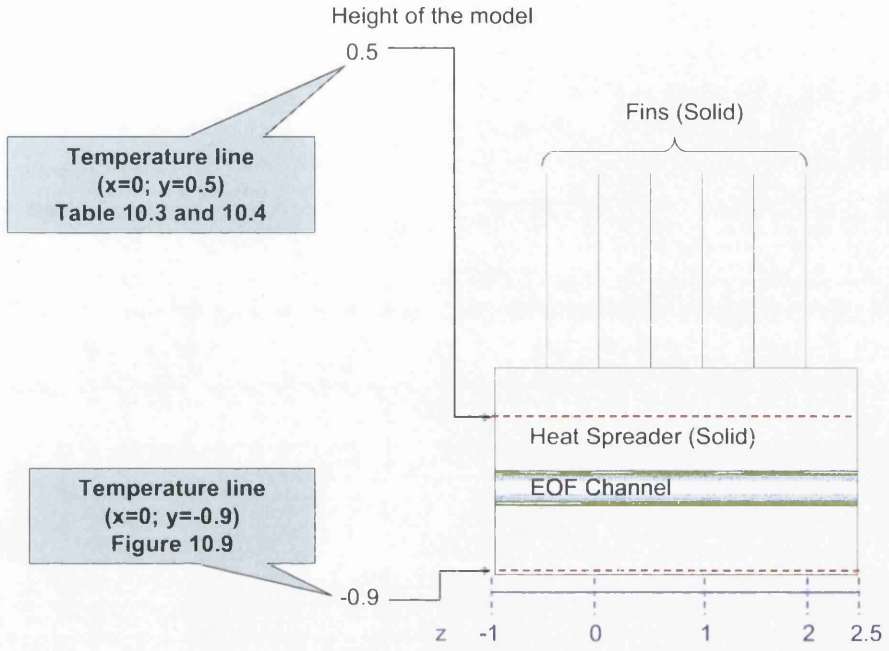

Figure 10.6: EOF channel in the heat spreader model.

is convected from the heat source. Here, two different cases of heat sources are considered. In the first case, a uniform temperature that is higher than atmospheric temperature is considered. In the second case, a non-uniform temperature distribution is assumed on the bottom surface (heat source). In this section, EOF based micro-cooling system is compared with the conventional micro-cooling system which has no electrolyte flow.

Additionally, Biot number used to describe the convective boundary condition on the fin surfaces is also varied. The temperature distribution at Biot numbers of 0.1, 1 and 10 are simulated and the influence of Biot number is studied.

10.4.1 Uniform Heat Source

In this section, a non-dimensional temperature of 0.124 (62^oC) is prescribed at the bottom surface (Refer to Figure 10.7(a)). The temperatures at line ($x = 0$ and $y =$ -0.9) which is near the heat source is plotted in Figure 10.8. As seen in the figure, uniform temperature distribution is shown with non dimensional value of 0.124.

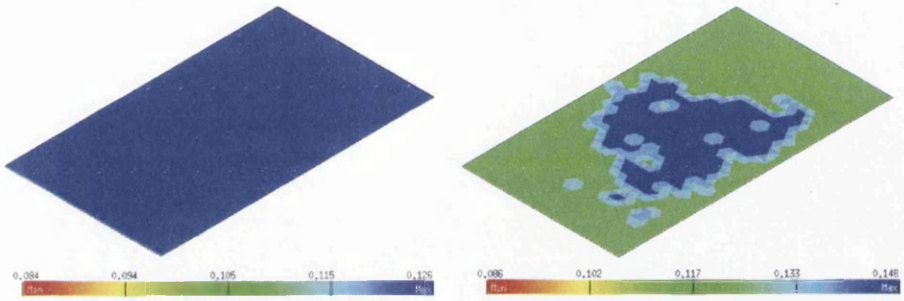

(a) (b)

Figure 10.7: (a)Uniform and (b)Non uniform heat sources.

Heat Spreader Without EOF channel

A geometry of heat spreader with fins as shown in Figure 10.1(a) is used in the present simulation. It contains fins and two substrates. Here, silicon dioxide substrates are used. Its thermal diffusivity is about $9 \times 10^{-7} m^2/s$. Thus, the non-dimensional thermal diffusivity in the solid area is 6.2. Convective heat transfer boundary condition is applied between the fins and the ambient. Biot numbers of 0.1, 1 and 10 are used in the simulation to study the influence of Biot number.

Figure 10.9(a) shows the temperature distribution in the heat spreader with a uniform heat source. The cuts of the heat spreader were taken through the geometry at the $z = 0$. No EOF channel is assumed here. Therefore, only heat conduction equation is solved. As the Biot number increases, increase in heat transfer rate is evident from the change in temperature distribution.

The maximum temperature at line ($x = 0$ and $y = 0.5$) which is located above the channel is recorded in Table 10.3. At a Biot number of 0.1, the maximum temperature at the point (0, 0.5, 0.75) is about 48 ^oC. At higher Biot number, $Bi = 1$ and 10, the temperature is reduced to 45 ^oC and 41 ^oC respectively.

The temperature distribution of Figure 10.9(a) at position $z = 0.75$ is plotted over the geometry height and is shown in Figure 10.10. The system without EOF channel (red line) is decreased linearly from the heat source (y = -1) until the top part of the heat spreader (y = 0). Then, from the point of $y = 0$, the temperature gradient is reduced due

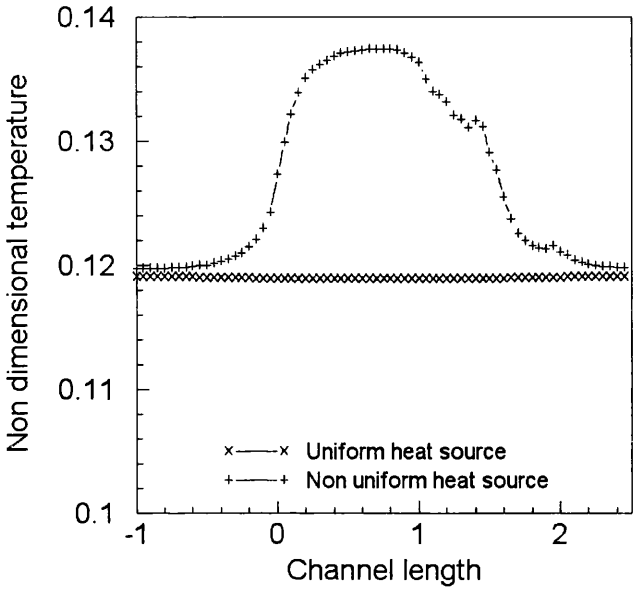

Figure 10.8: Temperature distribution of the heat spreader with a uniform and non-uniform heat source at line $x = 0$ and y = -0.9.

Table 10.3: Temperature at a point for uniform heat source case at Biot numbers = 0.1, 1 and 10 at point x, y, z of (0, 0.5, 0.75).

Biot number	Temperature without EOF	Temperature with EOF	Temperature Difference
0.1	48 ^oC (T^*=0.077)	44 ^oC (T^*=0.065)	4 ^oC
1.0	45 ^oC (T^*=0.067)	40 ^oC (T^*=0.052)	5 ^oC
10	41 ^oC (T^*=0.052)	35 ^oC (T^*=0.033)	6 ^oC

to convective boundary condition is assumed near the fins.

The influences of non dimensional thermal diffusivity, α^* of the solid part to the temperature distribution are studied here. The maximum temperatures of line $x = 0$ and $y = 0.5$ between $\alpha = 1$ to 120 are recorded in Figure 10.11. As seen, the maximum temperatures are increased rapidly from $\alpha^* = 1$ to 12. The maximum temperature becomes constant after $\alpha^* = 12$.

At high thermal diffusivity, the solid becomes more easy to change the temperature. It tends to reach higher temperature. However, in low thermal diffusivity, the solid has more heat capacity to absorb heat energy from changing the temperature.

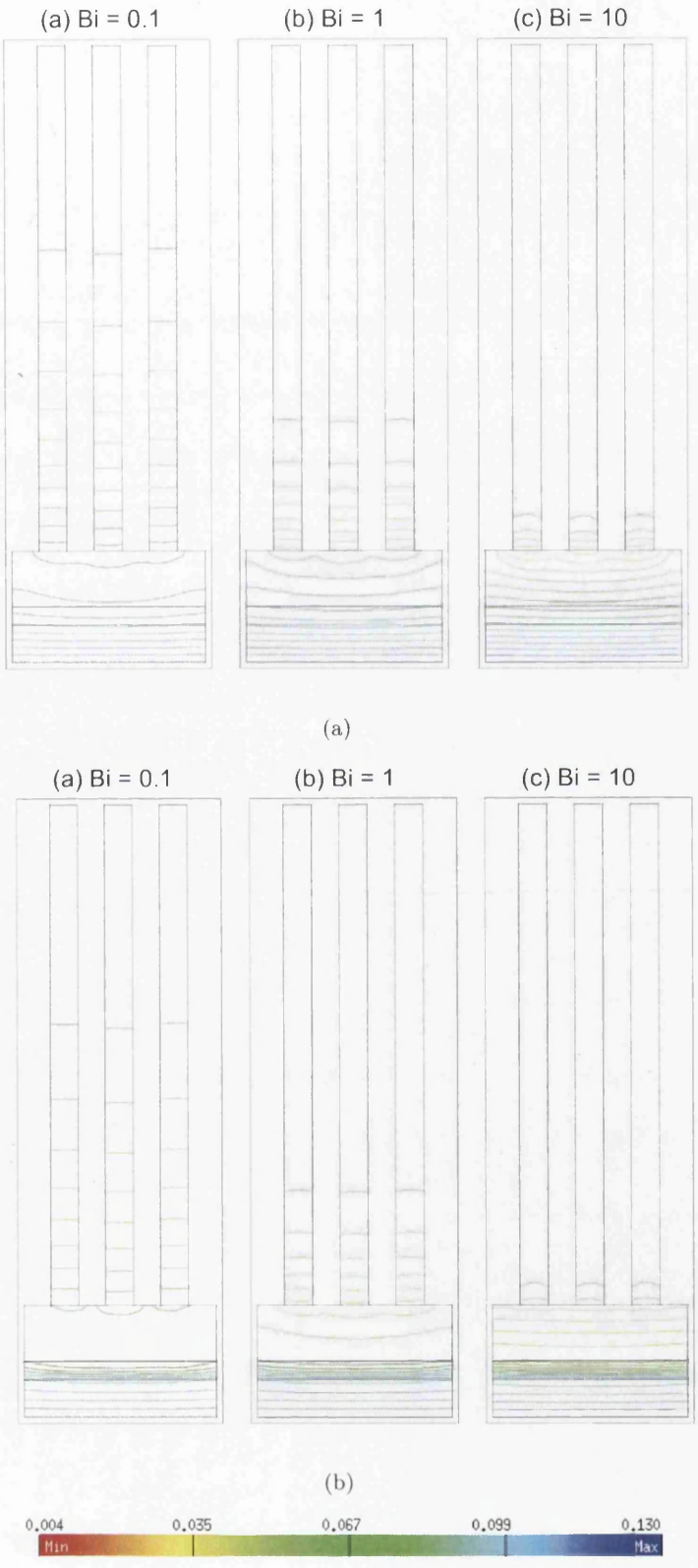

Figure 10.9: Temperature distribution on uniform heat source case (a)without EOF (b)with EOF at Biot numbers of 0.1, 1 and 10.

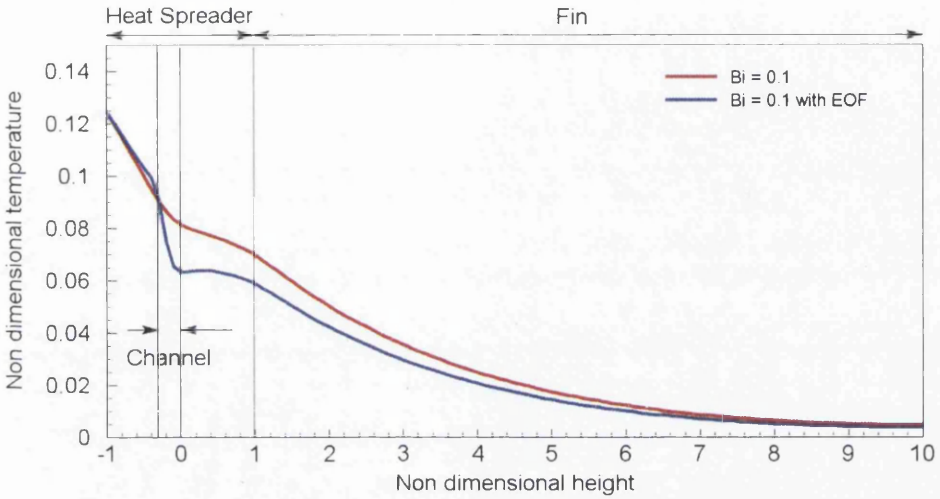

Figure 10.10: Temperature distribution on uniform heat source at Biot numbers of 0.1 at x, y, z of (0, -1 to 10, 0.75)

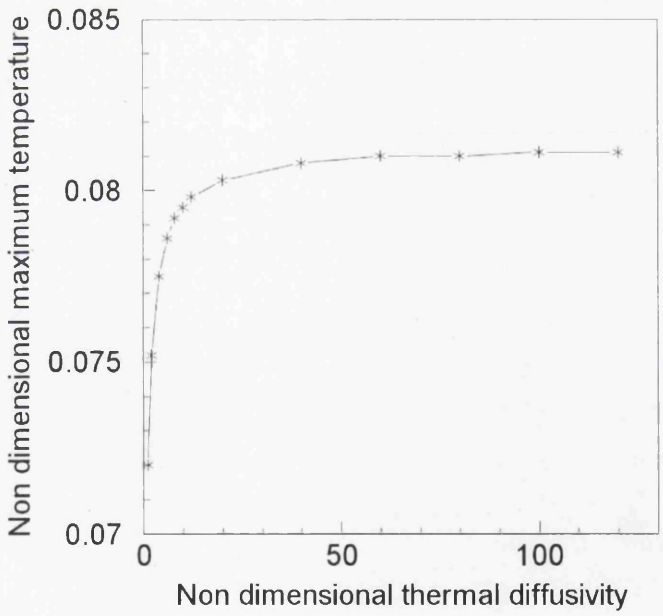

Figure 10.11: Maximum temperature on different thermal diffusivity at line $x = 0$ and $y = 0.5$.

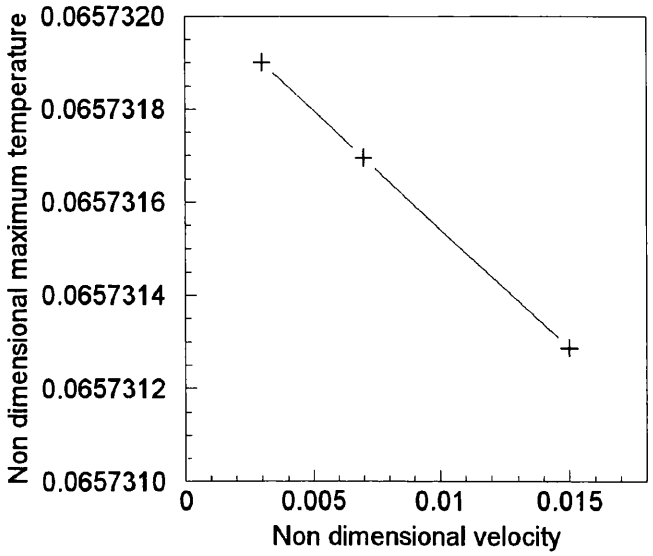

Figure 10.12: Maximum temperature on different velocity at line $x = 0$ and $y = 0.5$.

Heat Spreader With EOF channel

Here, converged EOF flow is employed into the heat spreader to calculate the temperature distribution. As in the previous section, uniform heat source is assumed at the bottom plane of the heat spreader. In the EOF active region, thermal diffusivity is equal to 1 while in the solid region, thermal diffusivity is set to 6.2.

The temperature distribution of the heat spreader system is shown in Figure 10.9(b). At $Bi = 0.1$, the temperature at a section above the channel is lower than the model without the EOF channel which is shown in Figure 10.9(a). This clearly shows that the electrolyte flow transports energy with it to reduce temperature. Thus, the heat transportation in this case is larger than in previous case.

As shown in Table 10.3, the temperature at the point of (0, 0.5, 0.75) is reduced by 4 ^oC to 44 ^oC with the activation of EOF compared to the previous results. This is also applicable to $Bi = 1$ and $Bi = 10$ cases. This clearly demonstrates that the EOF based heat spreader is effective in transporting heat.

As seen in the Figure 10.10, with the aid of the EOF channel (blue line), the temperature is significantly reduced in the EOF channel. This is because the electrolyte in

Table 10.4: Temperature at a point for non-uniform heat source case at Biot numbers = 0.1, 1 and 10 at point x, y, z of (0, 0.5, 0.75).

Biot number	Temperature without EOF	Temperature with EOF	Temperature Difference
0.1	49 ^oC (T^*=0.080)	46 ^oC (T^*=0.069)	3 ^oC
1.0	46 ^oC (T^*=0.071)	43 ^oC (T^*=0.059)	3 ^oC
10	41 ^oC ^oC (T^*=0.055)	38 ^oC (T^*=0.044)	3 ^oC

the EOF channel has higher heat capacity and absorb more heat from the solid part of the geometry. Then, the overall temperature of the geometry is reduced.

The influence of velocity in the EOF channel on the temperature distribution is studied here. Non dimensional velocities of 0.003, 0.007 and 0.015 are used in the present study. As seen in Figure 10.12, an increase of the velocity of EOF, reduces the maximum temperature at line $x = 0$ and $y = 0.5$. However, the maximum temperatures between these velocities are not changing much.

10.4.2 Non-uniform Heat Source

A non-uniform temperature heat source is studied in this section. Non-uniformity in temperature is with a peak temperature at the mid surface of the source as shown in Figure 10.8. The highest temperature is 68 ^oC. The non-dimensional hot spot peak temperature is 0.144. The non-uniform heat source pattern is shown in Figure 10.7(b).

Heat Spreader Without EOF channel

Figure 10.13(a) shows the temperature distribution of heat spreader with a non-uniform heat source. As discussed in previous section, an increase in Biot number decreases the temperature at any section above the heat source.

As seen in Figure 10.14, the temperature is decreased from the heat source at position $y = -1$. Then, the temperature is further dropping after convective boundary condition is assumed near the fins.

According to the Table 10.4, at Biot number of 0.1, the temperature at the point of (0, 0.5, 0.75) is about 49 ^oC. At higher Biot number, $Bi = 1$ and 10, the temperature is reduced to 46 ^oC and 41 ^oC respectively.

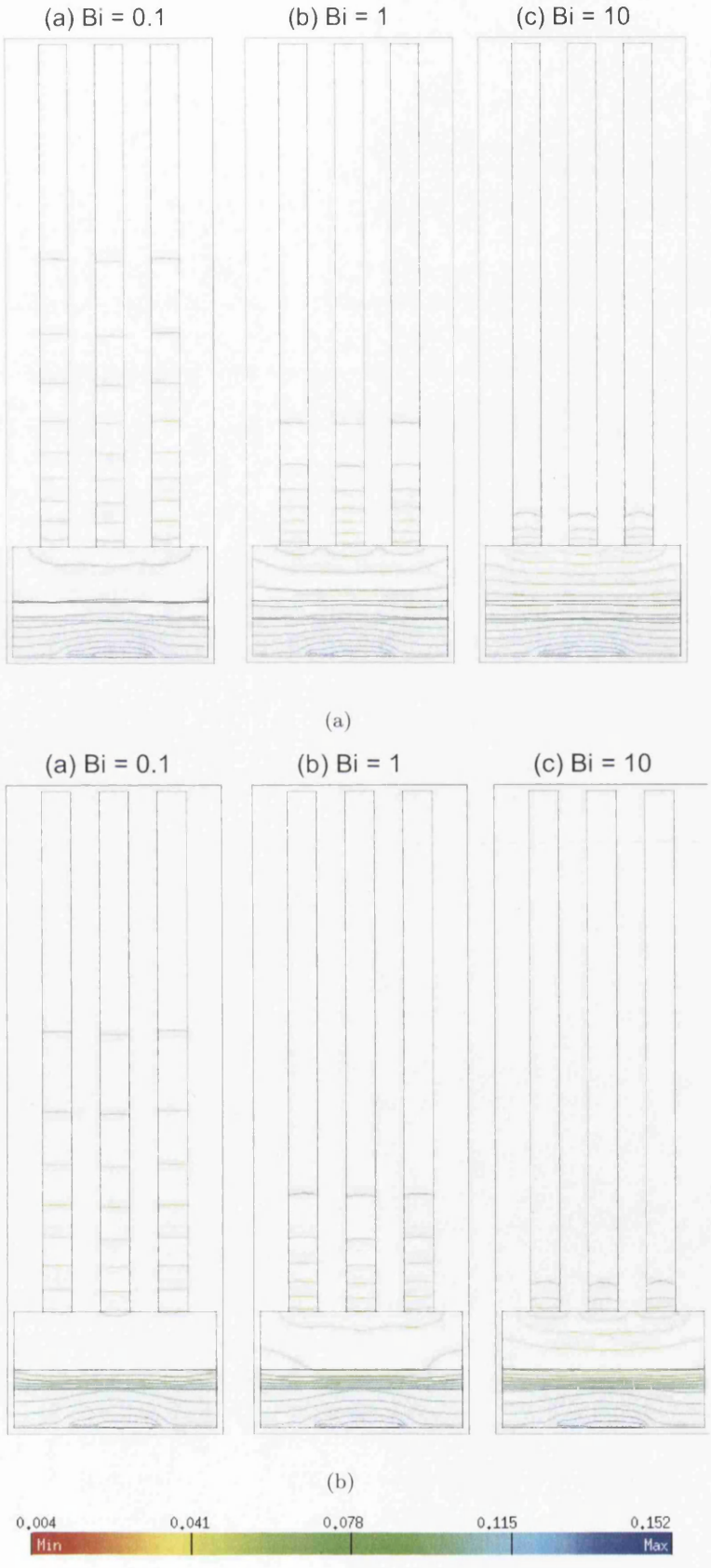

Figure 10.13: Temperature distribution for a non-uniform heat source (a)without EOF (b)with EOF at Biot numbers of 0.1, 1 and 10.

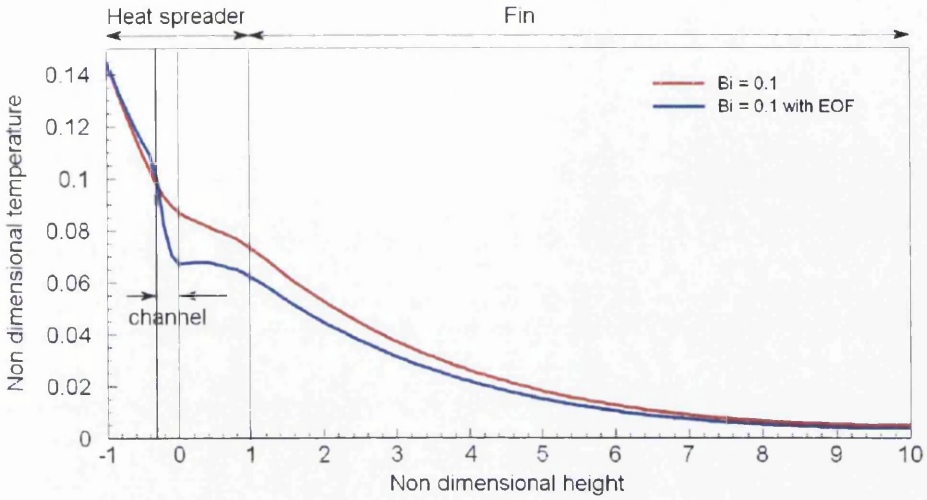

Figure 10.14: Temperature distribution on a non-uniform heat source at Biot numbers of 0.1 at x, y, z of (0, -1 to 10, 0.75).

Heat Spreader With EOF channel

Temperature distribution of heat spreader in the presence of EOF channel is shown in Figure 10.13(b). As seen the temperature at a section above the channel is reduced due to EOF. The temperature is also reduced as the Biot number is increased.

Beside, with the aid of the EOF channel, the temperature near the EOF channel region is significantly reduced as seen in Figure 10.14. Again, the EOF can reduce overall temperature of the geometry.

As seen in Table 10.4, the temperature at the point (0, 0.5, 0.75) is reduced by 3 ^oC to 46 ^oC at $Bi = 0.1$ when EOF is induced. Similar results are obtained at Biot numbers of 1 and 10.

Figure 10.15 shows the temperature distribution at line $x = 0$ and $y = 0.5$. This figure clearly shows that the temperature goes down as the Biot number is increased. It also shows that the temperature is lower when EOF is activated.

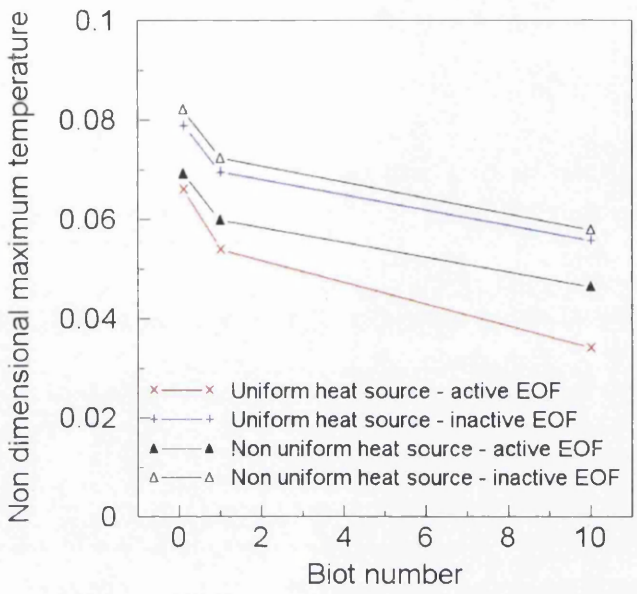

Figure 10.15: Non-dimensional maximum temperature distribution for uniform and non-uniform heat source at Biot numbers = 0.1, 1 and 10 at point x, y, z of (0, 0.5, 0.75).

10.5 Summary

The major objective of this chapter was to develop a conjugate heat transfer model for the proposed EO heat spreader with fins. A converged EOF solution was embedded into the heat spreader. With the embedded EOF model, the temperature distribution of the cooling system with a uniform or non uniform heat source was investigated. The simulation results demonstrated that the increase in Biot number can enhance the heat transfer. Temperature difference between both systems with and without the presence of EOF channel is notably different. It is also obvious from the results that the temperature at a point above the micro-channel is reduced by between 3 to 6 ^oC when EOF is induced in uniform and non-uniform heat source cases. The numerical model shows that electro-osmotic based heat spreader can be an alternative for conventional solid heat spreaders.

Chapter 11

Conclusions

11.1 Conclusion

This thesis proposes the concept of using electro-osmosis (EO) to drive fluid flow through a micro-cooling system. The concept was demonstrated to be viable by using both experimental and numerical methods of analyses. Following paragraphs summarize some of the achievements and important conclusions of the study.

11.1.1 Achievements

- Fabrication of shallow and deep micro-channel etching developed were able to produce micro-channels depth between 1.25 to 83 μm. These recipes were created specifically for the electro-osmotic flow applications. A novel deposition technique was developed to install a pair of gold thin film electrodes to apply external potential difference on the electrolyte.

- A new and robust way of insulating the current from penetrating wafer was introduced. This was achieved by depositing a layer of silicon dioxide on the inside channel surfaces.

- A method of calculating velocity and flow rate was developed and included in the experimental flow measurements.

- A novel procedure based on cyclic AC voltage was developed to reduce bubble gener-

ation in the flow field.

- A mesh sensitivity study was carried out to obtain high quality mesh for the study.
- The heat spreader problem was reduced in size to obtain a model for numerical calculations.
- The AC-CBS procedure was employed to carry out a conjugate heat transfer analysis with electroosmosis.
- Experimental and numerical results were compared.

11.1.2 Conclusions

The results of etching clearly show that the developed etching recipes are reliable to create micro-channel depths of between 1.25 and 83 μm. In this thesis, 30 μm channel depth was used in the electro-osmotic heat spreader. The electro-osmotic pump in the heat spreader has size of 0.6 mm^3 which is smaller compared to Yao el at [23] and Laser at el [24, 25, 26]. With this size, the electro-osmotic heat spreader is possible to be fabricated in an embedded electronic system and provide cooling for the system.

The deposition technique clearly shows that the method is reliable in producing very thin electrodes. The resistance offered by the electrodes to the flow is very small as the thickness of the electrodes about 1 μm. Gold thin film deposition is suitable for micro-scale fabrication compared to the design which the platinum wire was used [1]. However gold electrodes were proved to be prone to electrolysis.

The choice of SiO_2 to electrically insulate the inner channel surfaces has given excellent results. The current penetration into substrate has been reduced from 54.8 mA to 6 μA at 1 V. The advantages of deposition the SiO_2 layer in between the silicon substrate and electro-osmotic pump is beneficial for close proximity cooling of electronic device.

The flow rate obtained without SiO_2 insulation was 0.0013 $\mu l/min$ with 80 kV/m. This flow rate was increased to 0.2028 $\mu l/min$ when SiO_2 insulation was used at only 2 kV/m. The obtained velocities in experiments were comparable with the velocities which

were obtained in numerical simulation in Chapter 10. The flow rates were calculated to understand the amount of electrolyte can be transported in the electro-osmotic heat spreader.

The pulsed voltage method introduced reduced the bubble formation significantly. The optimum cycle was found to be with a maximum voltage of 10.4 V and a minimum voltage of -1.4 V with a duty cycle of 30 percent and a frequency of 10 Hz. With this cycle a flow rate of 0.237 $\mu l/min$ was generated. This is comparable with the flow rates with fixed external voltage difference which were shown in Chapter 5.

The experimental results on the heat spreader clearly show that including EOF reduces the temperature by more than 4 ^oC.

The numerical solutions obtained for the conjugate heat transfer problem are in good agreement with the experimental data. Parametric studies clearly show that the temperature can be reduced by 3 to 6 ^oC when EOF is induced. This also demonstrated that the electro-osmotic micro-pump in the heat spreader is an alternative for micro-cooling system.

11.2 Future Work

One of the major stumbling blocks of taking the proposed spreader idea to field application is developing appropriate technology for bonding. Since the bonding surfaces are not smooth and area available for bonding is limited, obtaining a perfect bonding is an issue. Although this thesis attempted the available bonding techniques, further research is essential to produce a perfect bonding technology.

Many other minor aspects such as Joule heating, flow measurements and reliability of electrodes need better understanding. However bonding is probably the most important issue.

Bibliography

[1] L. Jiang, J. Mikkelsen, J.M. Koo, D. Huber, S. Yao, L. Zhang, P. Zhou, J.G. Maveety, R. Prasher, J.G. Santiago, T.W. Kenny, and K.E. Goodson. Closed-loop electroosmotic microchannel cooling system for VLSI circuits. *IEEE Transactions on Components and Packaging Technologies*, 25:347–355, 2002.

[2] E.Y. Wu, R.P. Vollertsen, R. Jammy, A. Strong, and C. Radens. Leakage current and reliability evaluation of ultra thin reoxidized nitride and comparison with silicon dioxide. *40th Annual International Reliability Physics Symposium Proceeding*, pages 255–267, 2002.

[3] Matec Applied Sciences. Zeta potential - the importance of zeta potential, the electroacoustic method and case studies involving titanium dioxide and silicon dioxide. *Azonanotechnology Article*, March, 2005.

[4] M.J. Kim, A. Beskok, and K.D. Kihm. Electroosmotic driven microchannel flows: A comparative study of microscopic particle image velocimetry measurements and numerical simulations. *Experiments in Fluids*, 33:170–180, 2002.

[5] International Technology Roadmap for Semiconductors - ITRS 2007 Edition. *http://www.itrs.net/reports.html*, 2007.

[6] M. Sahraoui, T. Cader, and G.R. Ahmed. Cooling technologies for high heat flux applications. *Thermal and Thermomechanical Phenomena in Electronic Systems*, 2:692–693, 2004.

[7] G. Upadhya, M. Munch, Z. Peng, J. Horn, D. Werner, and M. McMaster. Micro-scale

liquid cooling system for high heat flux processor cooling applications. *Semiconductor Thermal Measurement and Management Symposium*, pages 116–119, 2006.

[8] I. Mudawar. Assesment of high heat flux thermal management schemes. *ITCPT*, 24:122–141, 2001.

[9] H.Y. Zhang, D. Pinjala, O.K. Navas, M.K. Iyer, P.K. Chan, X.P. Liu, H. Hayashi, and J.B. Han. Development of thermal solutions for high performance laptop computers. *Inter Society Conference on Thermal Phenomena*, pages 433–440, 2002.

[10] T. Nguyen, M. Mochizuki, K. Mashiko, Y. Saito, L. Sauciuc, and R. Boggs. Advanced cooling system using miniature heat pipes in mobile pc. *Thermal and Thermomechanical Phenomena in Electronic Systems*, pages 507–511, 1998.

[11] Z.J. Zuo, M.T. North, and K.L. Wert. High heat flux heat pipe mechanism for cooling of electronics. *ITCPT*, 24:220–225, 2001.

[12] J.R. Guarino and V.P. Manno. Characterization of laminar jet impingement cooling in portable computer applications. *ITCPT*, 25:337–346, 2002.

[13] S.Y. Kim, M.H. Lee, and K.S. Lee. Heat removal by aluminum-foam heat sinks in a multi-air jet impingement. *ITCPT*, 28:142–148, 2005.

[14] E.N. Wang, L. Zhang, L. Jiang, J.G. Maveety J.M. Koo, E.A. Sanchez, K.E. Goodson, and T.W. Kenny. Micromachined jets for liquid impingement cooling of vlsi chips. *Journal of Microelectromechanical Systems*, 13:833–842, 2004.

[15] A.M. Kiper. Impingement water jet cooling of vlsi circuits. *International Communications in Heat and Mass Transfer*, 11:517–526, 1984.

[16] D.B. Tuckerman and R.F.W. Pease. High performance heat sinking for vlsi. *IEEE Electron Device Letters*, 2:126–129, 1981.

[17] H.Y. Zhang, D. Pinjala, T.N. Wong, and Y.K. Joshi. Development of liquid cooling techniques for flip chip ball grid array packages with high heat flux dissipations. *ITCPT*, 28:127–135, 2005.

[18] L. Zhang, J.M. Koo, L. Jiang, M. Asheghi, K.E. Goodson, J.G. Santiago, and T.W. Kenny. Measurements and modeling of two phase flow in microchannels with nearly constant heat flux. *Journal of Microelectromechanical Systems*, 11:12–19, 2002.

[19] L. Zhang, K.E. Goodson, and T.W. Kenny. *Silicon Micro-channel Heat Sinks: Theories and Phenomena.* Springer, 2004.

[20] C. Gillot, C. Schaeffer, and A. Bricard. Integrated micro heat sinks for power multichip module. *IEEE Transactions on Inductry Applications*, 36:217–221, 2000.

[21] P.M. Martin. Microchannel heat exchanger for advanced climate control. *Proceeding of SPIE*, 2639:82–88, 1995.

[22] A.V. Vydai, S.B. Soshelev, G.V. Reznikov, V.V. Kharitonov, and S.V. Cheremushkin. Thermophysical design of the parameters of a computer board with a micro-channel cooling system. *Journal of Engineering Physics and Thermophysics*, 64:80–86, 1993.

[23] S.H. Yao, D.E. Hertzog, S.L. Zeng, and J.C. Mikkelsen Jr.and J.G. Santiago. Porous glass elecroosmotic pumps: Design and experiments. *Journal of Colloid and Interface Science*, 268:143–153, 2003.

[24] D.J. Laser and J.G. Santiago. A review of micropumps. *Journal of Micromechanics and Microengineering*, 14:792–795, 2004.

[25] D.J. Laser, A.M. Myers, S.H. Yao, K.F. Bell, K.E. Goodson, J.G. Santiago, and T.W. Kenny. Electroosmitc micropumps for integrated circuit thermal management. *Proc. Transducers, Boston, MA*, 2003.

[26] D.J. Laser. Design, fabrication, and applications of silicon electroosmotic micropumps. *Ph.D. dissertation, Stanford University*, 2005.

[27] D. Burgeen and F.R. Nakache. Electrokinetic flow in ultrafine capillary slits. *The Journal of Physical Chemistry*, 68:1084–1091, 1964.

[28] C.L. Rice and R. Whitehead. Electrokinetic flow in a narrow cylindrical capillary. *The Journal of Physical Chemistry*, 69:4017–4024, 1965.

[29] L. Hu, J.D. Harrison, and J.H. Masliyah. Numerical model of electrokinetic flow for capillary electrophoresis. *Journal of Colloid and Interface Science*, 215:300–312, 1999.

[30] J.Y. Min, E.F. Hasselbrink, and S.J. Kim. On the efficiency of electrokinetic pumping of liquids through nanoscales channels. *Sensors and Actuators B*, 98:367–377, 2004.

[31] G.Y. Tang, C. Yang, K. Chai C, and H.Q. Gong. Numerical analysis of the thermal effect on electroosmotic flow and electroskinetic mass transport in microchannels. *Analytica Chimica Acta*, 507:27–37, 2004.

[32] G.Y. Tang, C. Yang, J. Chai C, and H.Q. Gong. Modeling of electroosmotic flow and capillary electrophoresis with the joule heating effect: The nernst-planck equation versus the boltzmann distribution. *Langmuir*, 19:10975–10984, 2003.

[33] G.Y. Tang, D.G. Yan, C. Yang, H.Q. Gong, C.J. Chai, and Y.C. Lam. Joule heating and its effects on electroosmotic flow in microfluidic channels. *Journal of Physics Conference Series*, 34:925–930, 2006.

[34] N.A. Patankar and H.H. Hu. Numerical simulation of electroosmotic flow. *Analytical Chemistry*, 70:1870–1881, 1998.

[35] F. Bianchi, R.Ferrigno, and H.H. Girault. Finite element simulation of an electroosmotic driven flow division and a t-junction of microscale dimensions. *Analytic Chemistry*, 72:1987–1993, 2000.

[36] D. Erickson and D. Li. Three dimensional structure of electroosmotic flow over hetergenous surfaces. *Journal of Physical Chemistry B*, 107:12212–12220, 2003.

[37] M.F. Borges, L.L. Verardi, and J.M. Machado. Electroosmotic pumping in rectangular microchannel: A numerical treatment by the finite element method. *Applied Mathematics E-Notes*, 2:10–15, 2002.

[38] O.C. Zienkiewicz, R.L. Taylor, and P.Nithiarasu. *The Finite Element Method for Fluid Dynamics*. Elsevier, Amsterdam, 2005.

[39] P. Nithiarasu. An efficient artificial compressibility (ac) scheme based on the characteristic based split (cbs) method for incompressible flows. *International Journal for Numerical Methods in Engineering*, 56:1815–1845, 2003.

[40] P. Nithiarasu, J.S. Marthur, N.P. Weatherill, and K. Morgan. Three dimensional incompressible flow calculations using the characteristic based split (cbs) scheme. *International Journal for Numerical Methods in Fluids*, 44:1207–1229, 2004.

[41] O.C. Zienkiewicz and R. Codina. A general algorithm for compressible and incompressible flow - part 1: The split, characteristic based scheme. *International Journal for Numerical Methods in Fluids*, 20:869–885, 1995.

[42] O.C. Zienkiewicz, B.V.K. Satya Sai, K. Morgan, R. Codina, and M. Vaquez. A general algorithm for compressible and incompressible flow - part ii: Tests on the explicit form. *International Journal for Numerical Methods in Fluids*, 20:887–913, 1995.

[43] O.C. Zienkiewicz, P. Nithiarasu, R. Codina, M. Vazquez, and P. Ortiz. An efficient and accurate for fluid mechanics problem. the characteristic based split (cbs) algorithm. *International Journal for Numerical Methods in Fluids*, 31:359–392, 1999.

[44] R.F. Probstein. *Physicochemical Hydrodynamics.* Butterworths, 1989.

[45] R.W. Lewis and C. Humpheson. Numerical analysis of electroosmotic flow in soils. *Journal of the Soil Mechanics and Foundations Division*, 99:603–616, 1973.

[46] L. Fotsing, M. Fillet, I. Bechet, Ph. Hubert, and J. Crommen. Determination of six water soluble vitamins in a pharmaceutical formulation by capillary electrophoresis. *Journal of Pharmaceutical and Biomedical Analysis*, 15:1113–1123, 1997.

[47] M. Pumera. Analysis of nerve agents using capillary electrophoresis and laboratory on a chip technology. *Journal of Chromatohraphy A*, 1113:5–13, 2006.

[48] S.N. Murthy, Y.L. Zhao, S.W. Hui, and A. Sen. Synergistic effect of anionic lipid enhancer and electroosmosis for transcutaneous delivery of insulin. *International Journal of Pharmaceutics*, 326:1–6, 2006.

[49] C.W. Wei, T.H. Young, and J.Y. Cheng. Lab on a chip for drug development. *Electroosmotic mixing induced by non-uniform zeta potential and application for DNA microarray in microfluidic channel*, 55:49–377, 2003.

[50] S. Das, T. Das, and S. Chakraborty. Analytical solutions for the rate of dna hybridization in a microchannel in the presence of pressure driven and electroosmotic flows. *Sensors and Actuators B*, 114:957–963, 2006.

[51] M. Washizu, Y. Nikaido, O. Kurosawa, and H. Kabata. Stretching yeast chromosomes using electroosmotic flow. *Journal of Electrostatic*, 57:395–405, 2003.

[52] A. Manz, C.S. Effenhauser, N. Burggraf, D.J. Harrison, K. Seiler, and K. Fluri. Electroosmoctic pumping and electrophoretic seperations for miniaturized chemical analysis. *Journal fo Micromechanical Microengineering*, 4:257–285, 1994.

[53] D.J. Harrison, A. Manz, and P.G. Glavina. Electroosmotic pumping with a chemical sensor system integrated on silicon. *Solid State Sensor and Actuators*, pages 792–795, 1991.

[54] P. Woias. Micropumps-past,progress and future. *Journal of Sensors and Actuators B*, 2004.

[55] S.L. Zeng, C.H. Chan, J.C. Mikkelsen, and J.G. Santiago. Fabrication and characteristic of electroosmotic micropumps. *Journal of Sensors and Actuator B*, 79:107–114, 2001.

[56] C.H. Chen and J.G. antiago. A planar electroosmotic micropump. *Journal of Microelectromechanical Systems*, 11:672–683, 2002.

[57] J.O.M. Bockris and A.K.N. Reddy. *Modern Electrochemistry 1.* Plenum Rosseta, 1970.

[58] J.O.M. Bockris and A.K.N. Reddy. *Modern Electrochemistry 2.* Plenum Rosseta, 1970.

[59] S. Levine, J.R. Marriot, and K. RobinSon. Theory of electrokinetic flow in a narrow paralle plate channel. *Journal of Chemical Society Faraday Transactions 2: Molecular and Chemical Physics*, 71:1–11, 1975.

[60] D. Maynes and B.W. Webb. Fully developed electro-osmotic heat transfer in microchannels. *International Journal of Heat and Mass Transfer*, 46:1359–1369, 2003.

[61] A.T. Conlisk. The debye-hckel approximation: Its use in describing electroosmotic flow in micro- and nano-channels. *Electrophoresis*, 26:1896–1912, 2005.

[62] K.D. Huang and R.J. Jeng. Electrokinetic behaviour of overlapped electric double layers in nanofluidic channel. *Nanotechnology*, 18:115701.1–115701.6, 2007.

[63] T.S. Zhao and Q. Liao. Thermal effects on electro-osmotic pumping of liquids in microchannels. *Journal of Micromechanics Microengineering*, 12:962–970, 2002.

[64] W. Qu and D.Q. Li. A model for overlapped edl fields. *Journal of Colloid Science*, 224:397–407, 2000.

[65] D.G. Yan, C. Yang, H.Q. Gong, C.J. Chai, and Y.C. Lam. Assessment of joule heating and its effects on electroosmotic flow and electrophoretic transport of solutes in microfludic channels. *Electrophoresis*, 27:628–639, 2006.

[66] P. Nithiarasu and R.W. Lewis. A short note on joule heating in electro-osmotic flows: A consistent non-dimensional scaling. *International Journal of Numerical Methods for Heat and Fluid Flow*, 18:919–931, 2008.

[67] S. Multu. *Microfluidic Biochemical Analysis System with Electro-osmotic Pump and Thermally Responsive Polymer Valve.* ProQuest, 2005.

[68] R. Mahajan, C. Chiu, and G. Chrysler. Cooling a microprocessor chip. *Proceedings of the IEEE*, 94:1476–1486, 2006.

[69] P. Wang and A. Bar Cohen. On-chip hot spot cooling using silicon thermoelectric microcoolers. *Journal of Applied Physics*, 102:034503, 2007.

[70] T. Glawdel and C.L. Ren. Electroosmotic flow control for living cell analysis in microfluidic pdms chips. *Mechanics Research Communications*, In press, 2008.

[71] A. Brask, J.P. Kutter, and H. Bruus. Long term stable electroosmotic pump with ion exchange membrance. *Lab Chip*, 5:730–738, 2005.

[72] Y. Takamura, H. Onoda, H. Inokuchi, S. Adachi, A. Oki, and Y. Horiike. Low voltage electroosmotic pump for stand alone microfluidics devices. *Electrophoresis*, 24:185–192, 2003.

[73] M.D. Alvarez A. Merlos, J. Santander and F. Campabadal. Optimized technology for the fabrication of piezoresistive pressure sensors. *Journal of Micromechanical Microengineering*, 10:204–208, 2000.

[74] A. Hierlemann, O. Brand, C. Hagkeitner, and H. Baltes. Microfabrication techniques for chemical/biosensors. *Proceedings of the IEEE*, 91:839–863, 2003.

[75] S.M. Sze. *VLSI Technology.* McGraw-Hill, 1983.

[76] W.K.Chen. *The VLSI Handbook.* CRC Press, 1999.

[77] P. Rai Choudhury. *Handbook of Microlithography, Micromachining and Microfabrication. Volume 1: Microlithography.* SPIE Optical Engineering Press, 1997.

[78] C. Fu, C. Hung, and H. Huang. A novel and simple fabrication method of embedded su8 micro-channels by direct uv lithography. *Journal of Physics: Conference Series*, 34:330–335, 2006.

[79] C.H. Lin, G.B. Lee, B.W. Chang, and G.L. Chang. A new fabrication process for ultra-thick microfluidic microstructures utilizing su8 photoresist. *Journal of Micromechanics and Microengineering*, 12:590–597, 2002.

[80] S.S. Lyer and A.J. Auberton Herve. *Silicon Wafer Bonding Technology for VLSI and MEMS Application.* IET, 2002.

[81] J. wei, H. Xie, M.L. Nai, C.K. Wong, and L.C. Lee. Low temperature wafer anodic bonding. *Journal of Micromechanics and Microengineering*, 13:217–222, 2003.

[82] Z. Chen and R.K. Singh. Mechanism of particle deposition on silicon surface during dilute hf cleans. *Journal of the Electrochemical Society*, 150:667–672, 2003.

[83] N.T. Nguyen and S.T. Wereley. *Fundamentals and Applications of MIcrofluidics.* Artech House, 2006.

[84] A.J. Sprenkels, W. Olthuis, and P. Bergveld. The application of silicon dioxide as an electret materials. *IEEE*, pages 165–169, 1998.

[85] J. Wu, G. Soni, D. Wang, and C.D. Meinhart. Ac electrokinetic pumps for micro/nano fluidics. *ASME International Mechanical Engineering Congress and Exposition*, page 61836, 2004.

[86] H. Amjadi. Charges storage in double layers of thermally grown silicon dioxide and apcvd silicon nitride. *IEEE Transactions on Dielectrics and Electrical Insulation*, 6:852–857, 1999.

[87] X.G. Zhang. *Electrochemistry of Silicon and Its Oxide.* Kluwer Academic Plenum Publishers, 2001.

[88] S.M. Sze. *Physics of Semiconductor Devices.* John Wiley and Sons, 1981.

[89] J.G. Santiago, S.T. Wereley, C.D. Meinhart, D.J. Beebe, and R.J. Adrian. A particle image velocimetry system for microfluidics. *Experiments in Fluids*, 25:316–319, 2004.

[90] H. Chujo, K. Matsumoto, and I. Shimoyama. A high flow rate electro-osmotic pump with small channels in parallel. *Micro Electro Mechanical Systems MEMS IEEE The Annual International COnference*, 16:351–354, 2003.

[91] J. Koryta, J. Dvorak, and L. Kavan. *Principles of Electrochemistry.* Wiley, 1993.

[92] S. Multu, C.Yu, P. Selvaganapathy, F. Svec, C.H. Mastrangelo, and J.M.J. Frechet. Micromachined porous polymer for bubbles-free electroosmotic pumping. *Proc. IEEE MEMS*, pages 19–14, 2002.

[93] P. Selvaganapathy, Y.L. Ki, P. Renaud, and C.H. Mastrangelo. Bubbles-free electrokinetic pumping. *Journal of MEMS*, 11, 2002.

[94] A.K. Arnold, P.F. Eng, S.P. Singh, and P. Nithiarasu. Experimental and numerical comparison of electroosmotic flow through micro-channels. *Micro and Nanoscale Flows: Advancing the Engineering Science and Design,7-8 December,University of Strathclyde, Glasgow, UK.*, 2006.

[95] C. Yang, D.Q. Li, and J.H. Masliyah. Modelling forced liquid convection in rectangular microchannels with electrokinetic effects. *International Journal of Heat Mass Transfer*, 41:4229–4249, 1998.

[96] R.J. Yang, L.M. Fu, and Y.C. Lin. Electroosmotic flow in microchannel. *Journal of Colloid and Interface Science*, 239:98–105, 2001.

[97] P. Dutta, A. Beskok, and T.C. Warburton. Electroosmotic flow control in complex microgeometries. *Journal of Microelectromechanical Systems*, 11:36–44, 2002.

[98] C.M. Klaij, J.J.W. Van Der Vegt, and H. Van Der Ven. Pseudo-time stepping methods for space time discontinous galerkin discretisation of the compressible navier stokes equation. *Journal of Computational Physics*, 219:622–643, 2005.

[99] P. Nithiarasu, R. Codina, and O.C. zienkiewicz. The characteristic based split (cbs) scheme - a unified approach to fluid dynamics. *International Journal of Numerical Methods In Engineering*, 66:1514–1546, 2008.

[100] N.Massarotti, P.Nithiarasu, and O.C. Zienkiewicz. Characteristic based split (cbs) algorithm for incompressible flow problems with heat transfer. *International Journal for Heat and Fluid Flow*, 8:969–990, 1998.

[101] N.Massarotti, F. Arpino, R.W. Lewis, and P.Nithiarasu. Explicit and semi implicit cbs procedures for incompressible viscous flows. *International Journal for Numerical Methods in Engineering*, 66:1618–1640, 2006.

[102] R.W. Lewis, P. Nithiarasu, and K.N. Seetharamu. *Fundamentals of the Finite Element Method for Heat and Fluid Flow.* Wiley, New York, 2004.

[103] R.J. Yang, L.M. Fu, and C.C. Hwang. Electroosmotic entry flow in a microchannel. *Journal of Colloid and Interface Science*, 244:173–179, 2001.

[104] A.K. Arnold, P. Nithiarasu, and P.G. Tucker. Finite element modelling of electroosmotic flows using unstructured meshes. *International Journal of Numerical Methods for Heat and Fluid Flow*, 18:67–82, 2008.

[105] G. Chen, U. Tallarek, A. Seidel-Morgenstern, and Y. Zhang. Influence of moderate joule heating on electroosmotic flow velocity, retention and efficiency in capillary electrochromatograhpy. *Journal of Chromatography A*, 1044:287–294, 2004.

Appendix A

Fabrication Recipes

A.1 Photolithography Recipes

Table A.1: Photolithography recipes for shallow and deep channels

Photolithograhy process	**Shallow channels**	**Deep channels**
Photo-resist	S1828 (Positive Photo-resist)	SU8 (Negative photo-resist)
Range	436nm (G line)	355nm (I line)
Spinning speed 1	2000 rpm	500 rpm
Spinning time 1	30s	10s
Spinning speed 2	Nil	2000 rpm
Spinning time 2	Nil	30s
Soft baking time 1	2 min	16 min
Baking temperature 1	90°C	65°C
Soft baking time 2	Nil	16 min
Baking temperature 2	Nil	90°C
Exposure time	30s	40s
Exposure dose	$750mJ/cm^2$	$400mJ/cm^2$
UV light intensity	$25mW/cm^2$	$10mW/cm^2$
Hard baking time 1	Nil	1 min
Baking temperature 1	Nil	65°C
Hard baking time 2	Nil	12 min
Baking temperature 2	Nil	90°C
Develop solvent	MF 319	Solvent

Appendix B

Temperature Measurement

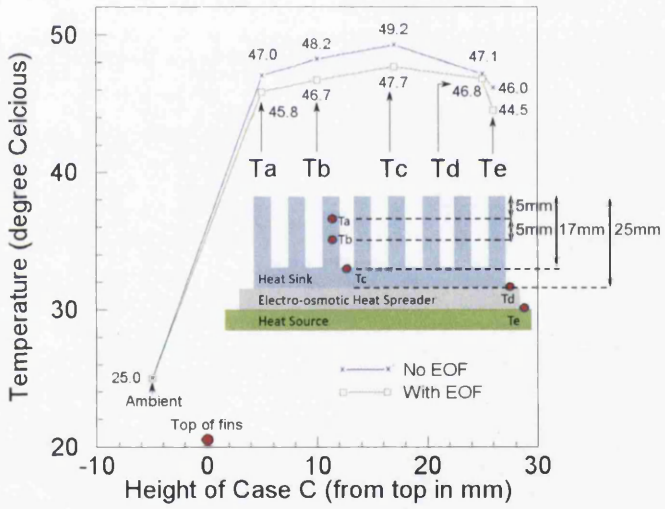

Figure B.1: Temperature of different locations in a cooling system.

The temperature of different positions in a cooling system is monitored and recorded in a graph as shown in the Figure B.1. The height of the heat sink is 25 mm. Without the water circulation, the temperature at a point T_a which is 5 mm below the tip of the heat sink is 47 ^oC. However, with the water circulation, the temperature at this point is reduced by 1.2 ^oC.

However, these temperature profiles are not agree with the numerical result which are shown in Figure 10.10 and 10.14. This is due to limitation in obtaining experimental

data. In the experiment, the thermocouple was used to get the temperature value. Therefore, only surface temperature is measured. The temperature value is affected by the room temperature.

To obtain an accurate temperature value, bulk temperature value is essential and micro temperature sensor is needed. The fabrication of micro temperature sensor in the silicon can be investigated.

Appendix C

Parametric Formula

C.1 Parametric Calculation in Velocimetry System

The straight channel image as shown in Figure C.1 has dimension and properties as in recorded in Table C.1.

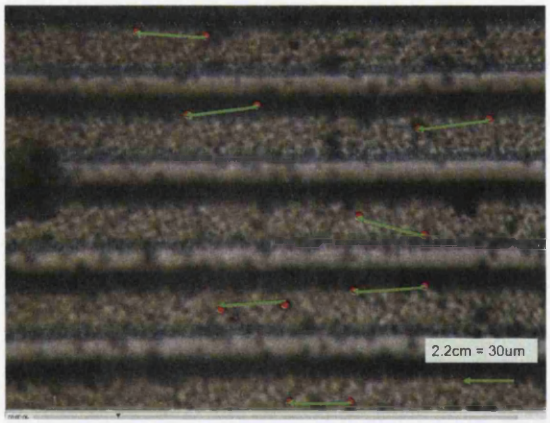

Figure C.1: Image of silicon dioxide straight channels at 20Vdc

The images with marked particle locations were overlapped as shown in Figure C.1. There are 7 pairs of line L_m was drawn its length was calculated by using Equation 5.3 and shown in Table C.2.

In this image, 2.2 cm (M) in the image is equal to 30 μm (W) which is known as

Table C.1: Dimensions and properties of a straight channel

Straight Channel	Silicon dioxide
Pumping Potential Difference (V)	20
Pumping Distance (mm)	10
Channel Width, W (μm)	30
Channel Depth, D (μm)	10
Channel Area, A (mm^2)	0.0003

Table C.2: Velocity calculation.

$RF = W/M$	L_m (m)	Δx (m)	Time Interval, Δt (s)	Velocity, u (mm/min)
1.364×10^{-3}	3.200×10^{-2}	43.640×10^{-6}	2	1.309
1.364×10^{-3}	3.200×10^{-2}	43.640×10^{-6}	2	1.309
1.364×10^{-3}	3.300×10^{-2}	45.000×10^{-6}	2	1.350
1.364×10^{-3}	3.000×10^{-2}	40.910×10^{-6}	2	1.227
1.364×10^{-3}	3.000×10^{-2}	40.910×10^{-6}	2	1.227
1.364×10^{-3}	3.200×10^{-2}	43.640×10^{-6}	2	1.309
1.364×10^{-3}	2.800×10^{-2}	38.180×10^{-6}	2	1.145

channel width of the channel. The representative fraction RF is calculated as:

$$\begin{aligned} RF &= \frac{W}{M} \\ &= \frac{30 \times 10^{-6} m}{2.2 \times 10^{-2}} \\ &= 1.36 \times 10^{-3} m \end{aligned}$$

At L_m of 3.2 cm, the actual displacement of a particle is obtained by the product of both representative fraction and L_m:

$$\begin{aligned} \Delta x &= L_m \times RF \\ &= \left(3.2 \times 10^{-2}\right) m \times \left(1.364 \times 10^{-3}\right) \\ &= 43.640 \times 10^{-6} m \end{aligned}$$

The velocity of every particle are obtained by dividing the particle displacement

with time interval of 2 s as shown in Table C.2. Following of that, the average velocity, $\overline{u}$ is determined and recorded in the Table C.3 with the equation as below:

$$\begin{aligned}\overline{u} &= \frac{1}{n}\sum_{i=1}^{n} u \\ &= \frac{[3(1.309)+1.350+2(1.227)+1.145]}{7} = 1.268 mm/min\end{aligned}$$

Table C.3: Average velocity, flow rate, mean deviation and error calculation

Average Velocity, $\overline{v}$ (mm/min)	1.268
Flow Rate per Channel, FR $(\mu l/min)$	$1.268 \times 0.0003 = 0.00038$
Flow rate of 152 Channels, FR $(\mu l/min)$	$0.000380 \times 152 = 0.0578$
Mean Deviation, $\lvert D\rvert$ (mm/min)	0.0010
Error, %	$0.058/1.268 \times 100\ \% = 4.61$

The obtained average velocity is then used to calculated the volumetric flow rate of micro-channel FR. Finally, the mean deviation, $|D|$ and experiment error, E_r were calculated.

C.2 Bulk ionic concentration

$$n_0 = N_A c \tag{C.1}$$

where N_A is Avogadro constant $(6.022 \times 10^{23} M)$ and c is the concentration of electrolyte in $Molar$.

Appendix D

Integration Formula

D.1 Integration by part and Green Lemma

$$\int_{\Omega} U\frac{\partial V}{\partial x}d\Omega = \int_{\Omega} \frac{\partial}{\partial x}UVd\Omega - \int_{\Omega} V\frac{\partial U}{\partial x}d\Omega \tag{D.1}$$

This can be simplified further by applying Green Lemma method

$$\int_{\Omega} f\frac{\partial^2 g}{\partial x^2}d\Omega = \int_{\Gamma} f\frac{\partial g}{\partial x}\overline{n}d\Gamma - \int_{\Omega} \frac{\partial f}{\partial x}\frac{\partial g}{\partial x}d\Omega \tag{D.2}$$

D.2 Taylor Expansion

$$U^n|_{(x-\delta)} = U^n - \delta\frac{\partial U^n}{\partial x} + \frac{\delta^2}{2}\frac{\partial^2 U^n}{\partial x^2} + O(\Delta t^3) \tag{D.3}$$

D.3 Integration of Shape Functions

Two dimensions:

$$\int_{\Omega} N_i^a N_j^b N_k^c d\Omega = \frac{a!b!c!2A}{(a+b+c+2)!} \tag{D.4}$$

where A is the area of a triangular element

Author's Publications

[1] P. Nithiarasu, P.F. Eng, A.K. Arnold, and S.P. Singh, Conceptual design, analysis and fabrication of a micro-cooling system for thermal management of electronic equipment, *International Conference on Trends in Product Lifecycle Modeling Simulation and Synthesis, PLMSS 2006, Bangalore, 18-20 Dec*, 35-43, 2006.

[2] A.K. Arnold, P.F. Eng, S.P. Singh, and P. Nithiarasu, Experimental and numerical comparison of electroosmotic flow through micro-channels, *Micro and Nanoscale Flows: Advancing the Engineering Science and Design,7-8 December,University of Strathclyde, Glasgow, UK*, 2006.

[3] A.K. Arnold, P. Nithiarasu, P. Tucker, and P.F. Eng, Electro-osmotic flow (EOF) in micro-channel experimental data and numerical invesitgation, *ISHMT-ASME Heat and Mass Transffer Conference, India*, 2006.

[4] P.F. Eng, P. Nithiarasu, A.K. Arnold, P. Igic, and O.J. Guy, Electro-osmotic flow based cooling system for microprocessors, *EUROSIME2007*, 2007.

[5] S.P. Singh, P. Nithiarasu, P.F. Eng, R.W. Lewis, and A.K. Arnold, An implicit-explicit solution method for coupled electro-osmotic flows in three dimensions using unstructured meshes, *International Journal for Numerical Methods in Engineering*, 73, 1137 to 1152, 2008.

[6] A.K. Arnold, P. Nithiarasu, and P.F. Eng, Electro-osmotic flow (EOF) in micro-channels, *Institution of Mechanical Engineers, Part C, Journal of Mechanical Engineering Science*, 2008.

[7] P.F. Eng and P. Nithiarasu, Numerical study of electro-osmotic flow and heat transfer in a microchannel cooling system, *ACME Newcastle*, 2008.

[8] P. Nithiarasu, P.F. Eng, and A.K. Arnold, Flow and heat transfer in micro-channels electro-osmotic flow, *5th European Thermal Sciences Conference Eindhoven*, 2008.

[9] P.F. Eng and P. Nithiarasu, Numerical investigation of an electro-osmotic cooling system, *ThermaComp Conference Naples, Italy*, 1, 2009.

[10] P.F. Eng and P. Nithiaeasu, Numerical Investigation of an Electro-osmotic Flow (EOF) based Micro-Cooling System, *Numerical Heat Transfer, Part B: Fundamentals*, Submitted.